Parameter Estimation Algorithms for Impulse Radio UWB Localization Systems

Fang Shang

Department of Electrical & Computer Engineering
McGill University
Montreal, Canada

November 2013

A thesis submitted to McGill University in partial fulfillment of the requirements for the degree of Doctor of Philosophy.

Abstract

Ultra Wideband (UWB) Impulse Radio (IR) technology has attracted considerable attention in the past few years due to its many desirable properties, such as the ability to penetrate through walls and ground, low power spectral density level, immunity to multipath fading and high temporal resolution. UWB radio is not restricted to radar and communications applications, but is also extensively used for indoor localization and tracking. Indeed, IR-UWB is especially well-suited for these applications since it offers centimeter accuracy, has low power requirements and allows for low cost hardware implementations. There is currently great interest for advanced applications of IR-UWB localization, such as real time inventory monitoring, asset identification and tracking in high security areas, monitoring of people or patients, and search/rescue operations, to name a few. Precise radio localization and tracking require the prior estimation of one or more key physical parameters, including: Angle of Arrival (AOA), Signal Strength (SS), Time of Arrival (TOA) and Time Difference of Arrival (TDOA). In this thesis, we study and design new low-complexity, yet accurate algorithms for parameter estimation in IR-UWB localization systems, including TOA and AOA, under single and multiple users scenarios. The original contributions of the thesis are organized along three main axes as follows.

The first problem we consider is the estimation of the TOA along with the Average Power Delay Profile (APDP), in a single-antenna single-user system operating at a sub-Nyquist rate. Indeed, while *a priori* knowledge of the APDP is assumed in many existing TOA estimators, its estimation has been overlooked in the literature. We assume a multi-cluster parametric model for the APDP and estimate its parameters via log-domain Least-Squares (LS) fitting; the estimated APDP is then used in conjunction with a maximum likelihood criterion to obtain the TOA estimate. Secondly, still in the context of single-user systems, we consider the case where an antenna array is employed at the receiver, and we develop a joint estimator of the TOA and AOA. The proposed method consists of two steps: (1) preliminary estimation of the TOA and APDP using energy-based threshold crossing and log-domain LS fitting, respectively; (2) joint TOA refinement and AOA estimation by local search of a Log-Likelihood Function (LLF) which employs the preliminary estimates from the first step. The derivation of the LLF relies on an original formulation in which the superposition of images from secondary paths is modeled as a Gaussian random process, whose second order statistical properties are characterized by a wideband space-time correlation function. In addition to the APDP, this function incorporates a special gating mechanism to represent the onset of the secondary paths, thereby leading to a novel form

of the LLF. Our third and final contribution deals with the extension of these newly proposed estimators to the multi-user case. More specifically, we consider the joint estimation of the TOA and AOA in the presence of Multi-User Interference (MUI), which is known to seriously degrade the estimation accuracy of these parameters. To solve this problem, we propose a new low-complexity approach which now includes three steps: (1) time alignment and averaging of the antenna signals using Time-Hopping (TH) codes to mitigate the effects of MUI; (2) preliminary TOA estimation based on energy detection followed by quadratic averaging; (3) joint TOA and AOA estimation using the previously developed LLF, but extended to account for MUI.

The performance of all these newly proposed methods and algorithms is thoroughly investigated by means of numerical simulation experiments over realistic UWB radio channels. Comparisons are made with the current state of the art as well as to closed-form expressions for the Cramer-Rao bound, which are also derived in this thesis. In all cases, significant improvements in estimation accuracy are demonstrated, as compared to existing benchmark approaches.

Sommaire

Les technologies d'impulsions radio (IR) à ultra large bande (UWB) ont attiré une attention considérable au cours des dernières années en raison de leurs nombreuses propriétés avantageuses, telles que la capacité de pénétrer les murs des édifices et le sol, le faible niveau de leur densité spectrale de puissance, leur immunité aux évanouissements causés par les trajets multiples, et leur résolution temporelle élevée. La transmission radio UWB n'est pas limitée aux applications radar et de communications et s'avère très utile pour la localisation et le suivi des sources à l'intérieur des édifices. En effet, l'IR-UWB est particulièrement bien adaptée à ce genre d'applications puisqu'elle offre une grande précision (de l'ordre du centimètre), demande une faible consommation de puissance et permet une mise en œuvre électronique à faible coût. Il y a donc présentement un grand intérêt pour les applications avancées de localisation IR-UWB, telles que le contrôle des inventaires en temps réel, l'identification et le suivi des biens dans les zones de haute sécurité, le pistage du personnel et des patients d'un hôpital et les opérations de secours et de sauvetage, pour n'en nommer que quelques unes. La localisation et le suivi de sources en précision au moyen de la technologie IR-UWB requièrent l'estimation au préalable d'un ou plusieurs paramètres physiques clés, incluant : l'angle d'arrivée (AOA), la puissance du signal (SS), le temps d'arrivée (TOA) et la différence de temps d'arrivée (TDOA). Dans cette thèse, nous concevons et portons à l'étude de nouveaux algorithmes à complexité réduite, mais toujours très précis pour l'estimation de paramètres physiques telles que le TOA et l'AOA, dans les systèmes de localisation IR-UWB à la fois pour les scénarios à usager unique et multi-usagers. Nos contributions originales s'orientent selon trois axes principaux.

Le premier problème que nous abordons est celui de l'estimation du TOA conjointement avec le profil de puissance du retard moyenné (APDP), dans un système à usager simple et antenne unique opérant en régime sub-Nyquist. En effet, bien que la connaissance *a priori* du APDP soit supposée connue dans de nombreux estimateurs du TOA de ce type, son estimation a été quelque peu négligée dans la littérature. Nous considérons un modèle paramétrique à agglomérats multiples pour l'APDP et estimons ses paramètres au moyen d'un ajustement par la méthode des moindres carrés (LS) dans le domaine logarithmique. L'APDP ainsi obtenu est alors utilisé dans un critère de maximum de vraisemblance (ML) afin d'obtenir l'estimé du TOA. Deuxièmement, toujours dans un contexte d'usager unique, nous considérons le cas où un réseau d'antennes est utilisé au récepteur et développons un estimateur conjoint du TOA et de l'AOA. La méthode proposée consiste en deux étapes : (1) estimation préliminaire du TOA et

de l'APDP par dépassement de seuil basé sur l'énergie et par ajustement LS dans le domaine logarithmique, respectivement; (2) raffinement du TOA et estimation de l'AOA, conjointement au moyen d'une recherche locale du maximum de la fonction de vraisemblance (LLF), utilisant les estimés préliminaires de l'étape précédente. La détermination de la LLF repose sur une formulation originale du problème dans laquelle la superposition des images provenant de trajets secondaires est modélisée comme un processus aléatoire Gaussien, dont les propriétés statistiques du second ordre sont caractérisées par une fonction de corrélation spatio-temporelle à large bande. En plus de l'APDP, cette fonction incorpore un mécanisme de déclenchement servant à représenter l'arrivée des trajets secondaires, ce qui conduit à une forme nouvelle de la LLF. Notre troisième et dernière contribution porte sur l'extension des nouveaux estimateurs au cas multi-usagers. Plus précisément, nous considérons l'estimation jointe du TOA et de l'AOA en présence d'interférence multi-usagers (MUI), laquelle peut avoir des effets dévastateurs sur la précision de cette estimation si elle n'est pas tenue en compte. En guise de solution à ce problème, nous proposons une nouvelle approche à complexité réduite et reposant maintenant sur trois étapes: (1) alignement temporel des signaux reçus aux antennes au moyen du code de saut temporel (TH) de l'usager désiré, dans le but de réduire les effets de la MUI; (2) estimation préliminaire des TOA basée sur la détection d'énergie suivie d'un moyennage quadratique; (3) estimation jointe du TOA et de l'AOA par maximisation de la LLF développée précédemment, mais étendue afin de tenir compte de la MUI.

La performance de tous les nouveaux estimateurs et algorithmes est étudiée en détail au moyen d'expériences de simulations numériques sur des modèles réalistes du canal radio UWB. Des comparaisons sont faites avec d'autres méthodes de pointe dans ce domaine ainsi qu'avec la borne de Cramer-Rao dont les diverses expressions sont développées dans la thèse. Dans tous les cas soumis à l'étude, des améliorations majeures sont démontrées au niveau de la précision des estimés, en comparaison avec les méthodes existantes.

Acknowledgments

First and foremost, I would like to thank Professor Benoit Champagne and Professor Ioannis Psaromiligkos for their guidance and constant support. I would also like to thank them for their strong scientific rigor, a much appreciated human approach and the great opportunities they gave me such as attending international conferences. I also extend my thanks to the faculty and staff of Electrical and Computer Engineering department and to the members of my Ph.D. committee.

I am also grateful for the financial support provided by a scholarship from McGill Engineering Doctoral Awards (MEDA) program and by Professor Champagne and Professor Psaromiligkos via research grants from the Fonds quebecois de la recherche sur la nature et les technologies (FQRNT) and the Natural Sciences and Engineering Research Council of Canada (NSERC).

Finally, I would like to express my deepest gratitude to my parents for their support and unconditional love in the past few years.

Contents

List of Figures

List of Tables

List of Acronyms

AOA	Angle Of Arrival
AWGN	Additive White Gaussian Noise
APDP	Average Power Delay Profile
BPM	Binary Position Modulation
BPAM	Binary Pulse Amplitude Modulation
BER	Bit Error Rate
CRB	Cramer Rao Bound
CSS	Chirp Spread Spectrum
CMOS	Complementary Metal Oxide Semiconductor
CM	Chanel Model
DS	Direct Sequence
DSSS	Direct-Sequence Spread Spectrum
DW-MESS	Double Weighted Maximum Energy Sum Selection
DSP	Digital Signal Processing
EIRP	Effective Isotropic Radiated Power
ED	Energy Detection
ESPRIT	Estimation of Signal Parameters via Rotational Invariance Techniques
EKF	Extended Kalman Filter
EM	Expectation Maximization
FCC	Federal Communications Commission
FIM	Fisher Information Matrix
GPS	Global Position System
GCC	Generalized Cross-Correlation
ITU-R	International Telecommunications Union Radiocommunication Sector

IR	Impulse Radio
LOS	Line Of Sight
LS	Least Square
LLF	Log-Likelihood Function
MPC	Multi Path Component
MF	Matched Filter
ML	Maximum Likelihood
MES	Maximum Energy Selection
MESS	Maximum Energy Sum Selection
MB-OFDM	Multi-Band Orthogonal Frequency Division Multiplexing
MUI	Multiuser Interference
MIMO	Mingle-Input Multiple-Output
NLOS	Non Line Of Sight
OFDM	Orthogonal Frequency-Division Multiplexing
OPM	Orthogonal Pulse Modularization
OOK	On Off Key
OLOS	Obstructed Line-Of-Sight
PSD	Power Spectrum Density
PR	Pseudo-Random
PPM	Pulse Position Modulation
PAM	Pulse-Amplitude Modulation
PDP	Power Delay Profile
PL	Path Loss
RF	Radio Frequency
RFID	Radio Frequency Identification
RSS	Received Signal Strength
RMSE	Root Mean Square Error
SF	Spreading Factor
SNR	Signal-to-Noise Ratio
STDL	Stochastic Tapped-Delay-Line
SIMO	Single-Input Multiple-Output
TH	Time Hopping
TOA	Time Of Arrival

TDOA	Time Difference Of Arrival
UWB	Ultra Wideband
ULA	Uniform Linear Array
UCA	Uniform Circular Array
WCDMA	Wideband Code Division Multiple Access
WPAN	Wireless Personal Area Network
WSN	Wireless Sensor Network
W-MESS	Weighted Maximum Energy Sum Selection
1D	1-dimensional
2D	2-dimensional

Chapter 1

Introduction

This chapter provides a general introduction to the thesis, which aims at developing and studying new signal processing algorithms for the problem of parameter estimation in impulse-based Ultra WideBand (UWB) localization systems. A high level overview of UWB technology and its applications are given in Section 1.1, while a literature review of various parameter estimation methods for UWB localization systems is presented in Section 1.2. The research objectives and the contributions of the thesis are discussed in Section 1.3, and finally, an outline of the upcoming chapters is presented in Section 1.4.

1.1 Ultra wideband technology for source localization

According to the rules issued by the United States Federal Communications Commission (FCC) [1] and International Telecommunications Union Radiocommunication Sector (ITU-R), a UWB signal is a radio signal with an absolute bandwidth of at least 500MHz, or with a fractional bandwidth larger than 20%. The absolute bandwidth B is defined as the difference between the upper frequency f_h and lower frequency f_l at the -10dB emission points, i.e., $B = f_h - f_l$, while the fractional bandwidth FB is defined as the ratio of the absolute bandwidth to the center frequency of the signal, i.e.,

$$FB = 2\frac{f_h - f_l}{f_h + f_l} \tag{1.1}$$

where $(f_h + f_l)/2$ is the center frequency.

The Power Spectral Density (PSD) level of UWB communications signals is quite low, as compared to narrowband or wideband signals used in more traditional communication systems.

This is because the large bandwidth of UWB signals is made available under tight limits on the emitted power. Indeed, due to the large frequency band covered by UWB systems, the control of the power at transmitter output in order to prevent interference to users of other communications equipment or devices that share the same or nearby frequency bands, becomes one of the most critical issues. In general, FCC in the USA and other groups in other countris have set the Effective Isotropic Radiated Power (EIRP) level of UWB transmitters to be no larger than -41.3dBm/MHz (dBm = decibel referenced to 1 milliwatt) in any direction, although a large continuous bandwidth of 7.5GHz exists from 3.1 to 10.6GHz to allow transmission at the maximum power. For illustrative purpose, the spectral mask of FCC's EIRP for indoor UWB systems is shown in Fig. 1.1. The extremely low values of the allowed power output at certain frequencies are set to avoid interference with existing radio communications services, e.g., Global Position System (GPS), in those bands.

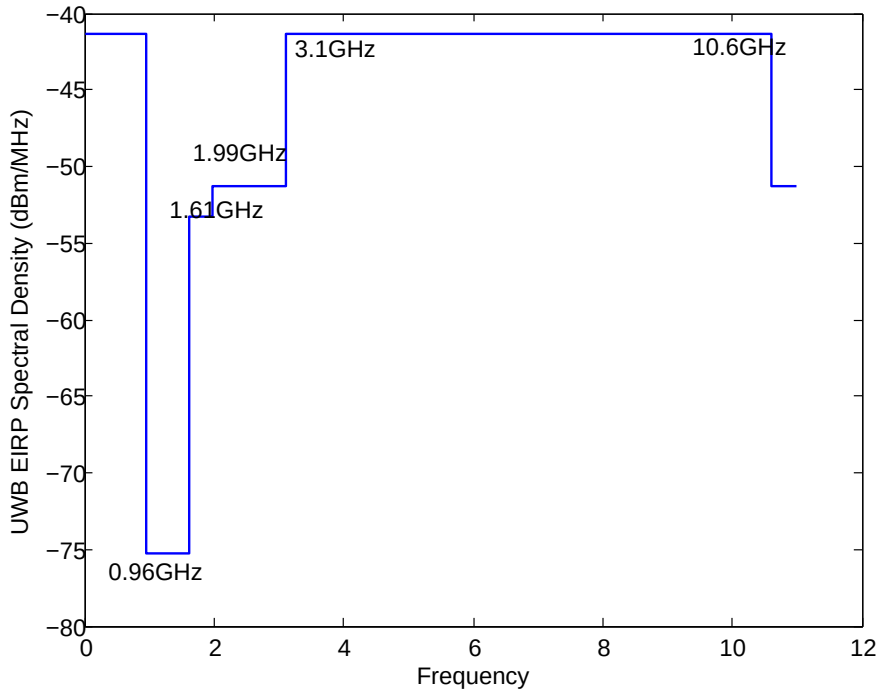

Fig. 1.1 FCC spectral mask for indoor UWB systems as taken from [1]

There were originally two IEEE Task Groups dealing with the development of standards related to UWB signals and systems, Task Groups IEEE 802.15.3a and IEEE 802.15.4a. Task Group IEEE 802.15.3a focused on a high-speed alternative to IEEE 802.15.3 (a standard for

high-rate Wireless Personal Area Network (WPAN)), in the form of a UWB physical layer for short-range WPAN [2], which utilizes all or part of the spectrum between 3.1 to 10.6 GHz and provides data rates up to 480 Mbps. Two main signaling schemes were proposed, namely: Multi-Band Orthogonal Frequency Division Multiplexing (MB-OFDM) [3] by WiMedia Alliance and Direct Sequence-UWB (DS-UWB) [4] by the UWB Forum.

In MB-OFDM UWB, the 7.5GHz spectrum is divided into 14 subbands, each with a bandwidth of 528MHz. The set of subbands is further partitioned into 5 groups, with the first four groups consisting of three subbands each, and the fifth group having 2 subbands. The OFDM symbols are transmitted using one of the available subbands in a particular time slot using a switching mechanism. Although this scheme is denoted as OFDM, it operates over a very wide bandwidth, much larger than that found in conventional OFDM systems, such as the IEEE 802.16e WiMAX. The introduction of carrier-based MB-UWB in IEEE 802.15.3a was intended for high-speed communications over short ranges in wireless home networking. Examples of targeted applications included high data rate (larger than 100Mb/s) download of digital television signals within a WPAN. An MB-UWB system has the potential of high data rates for short range transmissions, but is subject to both deep fades and Inter-Symbol Interference (ISI) when the duration of the cyclic prefix is shorter than the maximum channel delay spread.

The DS-UWB scheme is based on Direct-Sequence Spread Spectrum (DSSS) technology [5]. Here, each data symbol is spread in the frequency domain by means of a specific spreading code that takes the form of a transmit chip sequence at a rate higher than the data symbol rate; the integer ratio of the chip to symbol rate is known as the Spreading Factor (SF). In effect, the DS-UWB transmitter operates by sending a coded sequence of low power time localized pulses, which are coherently decoded at the receiver given the knowledge of the spreading code. Because these systems use very short pulses, with durations between ten to a few hundreds of picoseconds, the transmitted signals spread out over a wide frequency band that meets the defining conditions of UWB signals, as previously stated. DS-UWB signaling also suffers severely from ISI, since the SF is relatively small for high data rates as compared with that of other DSSS systems, such as Wideband Code Division Multiple Access (WCDMA).

Unfortunately, an agreement could not be reached in making a definite choice between these two proposals, i.e., MB-OFDM versus DS-UWB, and the IEEE 802.15.3a project authorization request was withdrawn in 2006. Nevertheless, research on these two different UWB signaling schemes has continued since then.

Task Group IEEE 802.15.4a focuses on a low data rate alternative to IEEE 802.15.4 in the

form of a UWB physical layer for WPAN [6]. Here, the available spectrum for UWB systems includes the 250-750MHz, 3.244-4.742GHz, and 5.944-10.234GHz bands. The IEEE 802.15.4a standard offers two different signaling schemes, namely: Chirp Spread Spectrum (CSS) and Impulse Radio UWB (IR-UWB). CSS is a spread spectrum technique based on fast frequency chirps [7], which achieves a wideband transmission by sweeping the transmitter oscillator's frequency across the available spectrum. Unlike the CSS signals, which are specifically designed for data communications [8], the IR-UWB signals consist of coded sequences of short duration pulses, which endow them with an optional capability for ranging applications. Therefore, they can be used for high precision localization in various environments, such as indoor residential, indoor office, industrial warehouse, as well as certain outdoor settings. In this thesis, we are interested in the ranging aspect of IR-UWB signaling, and so this scheme is discussed in further details below.

In IR-UWB systems, a train of modulated pulses, each with very short duration (typically a few tens to hundreds picoseconds) are transmitted with a low duty cycle, although each pulse instantaneously occupies a very large bandwidth. Generally, the spectrum of each pulse should adhere to the spectral mask requirements for the PSD as previously illustrated in Fig. 1.1. The signaling typically employs a repetition pattern so that multiple pulses are combined to carry the information of one bit. In IR-UWB signaling, the individual pulses are so short that most signal reflections do not overlap with the original pulse, and thus multipath fading as encountered in more traditional systems does not apply here. Due to their low PSD level and pseudo-random character (as a result of applying various types of modulations on the pulse sequence), IR-UWB signals also exhibit a noise-like signal spectrum which makes them resistant to unintended detection (eavesdropping). Moreover, IR-UWB signals can be easily coupled to without the need of a radio frequency (RF) mixing stage for up-conversion. Therefore, at the receiver, it is not necessary to employ a local oscillator nor the associated complex electronics for delay and phase tracking loops. As a result, both the complexity and cost of the IR-UWB transmitter and receiver can be kept relatively low. These favorable characteristics of IR-UWB systems have motivated their use in both ranging and communication applications.

Since the inception of IEEE 802.15.4a in late 2003, the development of UWB technologies for moderate to longer range communications (100-300m) at lower data rate (a few Mb/s) has received significant attention. The initially targeted applications in WPAN have been further extended to wireless home networking, wireless Universal Serial Bus (USB), etc. Meanwhile, UWB technology has also been applied to short range, low data rate communications such as in Wireless Sensor Network (WSN) applications [9].

Besides the above mentioned developments in IR-UWB technologies derived from IEEE 802.15.4a, there have been many earlier applications of UWB pulse signaling in the context of impulse radar, that include: imaging radar, vehicular radar, military radar, etc. [10]. The UWB nature of the short electromagnetic pulses confer them with a rich variety of material penetration properties. For instance, the low-frequency components of UWB pulse signals enable them to propagate effectively through various materials such as bricks and cement. The high temporal resolution of IR-UWB signals, combined with their good material penetration properties, allow them to be used for short range radar imaging systems, including ground penetration radars, through-wall radar imaging, surveillance and medical imaging. Their excellent time resolution and accurate ranging capability can be exploited in vehicular radar systems for collision avoidance, guided parking, etc.

In recent years, one of the most popular applications of UWB technology has been that of precise positioning and tracking of fixed or moving objects equipped with radio transmitters [11]. Due to their use of very short pulses in the time-domain, localization systems based on IR-UWB signaling can potentially offer timing precision of the order of a few tens of picoseconds, equivalent to centimeter resolution in positioning accuracy. The robust features of IR-UWB signals combined with through-wall propagation make them suitable for localization in harsh environments. Furthermore, the low power and cost attributes of the associated transceiver electronics make them attractive for the ultra-low power Radio-Frequency Identification (RFID) of objects equiped with small UWB transmitters also known as tags. In fact, IR-UWB represents a promising technology for locating people and assets, and navigating beyond the coverage zone of the GPS. Furthermore, because of its data handling capability, it can simultaneously be used for the accurate positioning *and* identification of multiple targets in different types of radio environments.

1.2 Literature review

While GPS shows excellent performance in outdoor localization, it fails to provide a good accuracy in indoor scenarios that are typically characterized by severe multipath effects. Hence, there is a growing interest for alternative IR-UWB localization, including ranging or positioning, in various commercial and military applications [12, 13, 14].

Radio localization is based on geometrical triangularization using location information from radio signals traveling between the target node and one or more reference nodes. This information can take different forms, depending on the specific radio measurements available at the reference

nodes, including: Received Signal Strength (RSS), Time of Arrival (TOA), Time Difference of Arrival (TDOA) and Angle of Arrival (AOA), [15]. In RSS-based approaches, the reference nodes are aware of the transmitted power level by the target node and employ a path loss model to estimate its distance based on the measured RSS. Unfortunately, due to the difficulty in predicting the path loss with sufficient accuracy in practice, the use of RSS does not allow a very precise localization of the target. Time-based techniques, such as those employing TOA and TDOA estimation, can make use of the utmost advantage of IR-UWB signaling (i.e., ultra short pulse duration) to achieve precise localization, and are therefore among the most popular approaches for indoor localization. In the case of TOA-based approaches, the positioning is achieved by employing distance measurements between the target and reference nodes, obtained in turn from the TOA measurements. Most TOA ranging schemes are based on the detection of the first arriving multipath component, and require timing synchronization between the target and reference nodes which poses a major challenge in dense multipath environments. Alternatively, the need for synchronization with the target node can be relaxed if two or more time-synchronized reference nodes are available. In this case, measurement of the TDOA between two such reference nodes (i.e., difference between their respective TOAs) provides information about the position of the target in the form of an hyperbola. Subsequently, localization of the target in the plane can be made by intersecting 2 or more such hyperbolas. AOA is another type of measurement that is increasingly used for ranging applications. In this approach, positioning is based on the measurement of angle between the line joining the target node to the receiver and some arbitrary reference direction. AOA estimation can be achieved via the application of advanced antenna array processing techniques.

In the rest of this section, we present selected recent works from the literature specific to the problems of TOA estimation for single antenna receiver, AOA and joint TOA/AOA for antenna array receivers, and spatial parameter estimation for multi-user applications, all under the common UWB framework.

1.2.1 TOA estimation methods

Traditionally, TOA estimation is performed by using a correlation or Matched Filter (MF) receiver, where the received noisy signal is matched to a time-shifted replica of the undistorted transmitted pulse waveform. The TOA estimate is then obtained as the time shift corresponding to the positive peak value at the output of the matching correlator. In the case of a single path ra-

dio channel, and under low noise conditions, this method provides good estimates of the unknown delay, which is equal to the propagation time between the transmitter and the receiver (assuming there is no synchronization error). However, it exhibits much poorer accuracy in multipath environments, because then it is highly unlikely that the peak MF output will correspond to the first (shortest) arrival path [16]. Unfortunately, the ideal single path condition of propagation is rarely met in practical applications of UWB signals to localization, where the typical radio channel instead exhibits a complex multipath structure [17, 18, 19, 20]. Accordingly, recent research efforts on TOA estimation with UWB signals have focused mainly on the multipath problem.

A Maximum Likelihood (ML) estimator of the TOA is derived in [21] with explicit consideration of multipath propagation. Its performance is shown to closely approach the Cramer-Rao Bound (CRB) on the variance of unbiased TOA estimators [22] at high Signal-to-Noise Ratios (SNRs). However, the excessive computational cost associated to the estimation of too many modeling parameters, including all the multipath arrival instants along with their channel gains, combined with the high sampling rate requirement for accurate TOA estimation, render this ML estimator impractical for UWB channels with a large number of multipaths [23]. To reduce complexity, the Generalized Maximum Likelihood (GML) estimator is proposed in [24] by utilizing a Sequential Component Cancellation (SCC). While assuming that the strongest channel path (i.e., the one leading to a positive peak in the ML-based objective function) has been correctly acquired, this estimator obtains the desired TOA as the location of the smallest delay found to be above a predetermined threshold during a backward search starting from this strongest path location. Nevertheless, the estimation error with this method cannot be reduced below a certain limit since the sequential cancellation scheme remains imperfect, even as the SNR increases.

Some recent works on practical ML-based TOA estimators aim at reaching a balance between low implementation complexity and competitive performance in estimation. In [25], an Improved Generalized Maximum Likelihood (IGML) estimator is proposed, based on the *a priori* knowledge of the Average Power Delay Profile (APDP), which characterizes the power of the received UWB signal through the multipath channel as a function of the propagation delay. In [26], sub-Nyquist sampling ML estimators with different levels of *a priori* information are compared, including the Maximum Energy Sum Selection (MESS), the Weighted Maximum Energy Sum Selection (W-MESS) and the Double Weighted Maximum Energy Sum Selection (DW-MESS). In [27], ML timing estimation with sub-sampling is proposed under the assumptions of normally distributed channel impulse response and known APDP. In [28], the authors propose a computationally efficient TOA estimator which is claimed to achieve the same performance as

the ML estimator in [21] when the multipath arrivals are dense.

While most ML-based TOA estimators employ a MF receiver, TOA estimation methods based on the Energy Detection (ED) receiver are also of interest due to their low complexity implementation, especially with sub-Nyquist sampling rates [29, 30, 31]. The performance of the low-sampling rate MF and ED for TOA estimation based on thresholding is analyzed and compared in [32]. In [33], a data-aided dual pulse autocorrelation based TOA estimation is proposed. The TOA of direct path is calculated by using the received signal autocorrelation and threshold-crossing (TC). In [34], a two-step approach is proposed where a coarse TOA estimate is first obtained based on ED, and then refined through a hypothesis testing-based process. Two new Bayesian TOA estimators that rely on the overall energy profile available at the output of the ED receiver are proposed in [35].

In the ED approach, the TOA is normally estimated as the first TC point of a time localized energy measure, where the threshold depends on the statistics of the received signal and the channel [36, 37, 38]. The effect of different values for the threshold is further studied. We note that these methods are sensitive to the threshold level: in order not to miss the attenuated first arrival, the threshold level cannot be set too high; but then, the algorithm can suffer from high false alarm (false detection) rates. False alarms can be either caused by noise at low SNR or interference from the pulse side lobes at high SNR, depending on the specific pulse shape being used at the transmitter. Since the performance of the detector greatly depends on the threshold level, the latter should be chosen carefully in order to reach a balance between the probability of missed detection and false alarms. In practice, one seeks to minimize the probability of missed detection subject to a constraint on the probability of false alarm.

1.2.2 AOA and joint TOA/AOA estimation methods

Some initial attempts in developing AOA estimators for UWB signals have focused on subspace-based methods [39, 40]. To apply the traditional subspace method (as in the narrowband case) to UWB signals, a focusing technique must be employed [41] to account for the dependence of the steering vector on the frequency. In [42], a new focusing technique for AOA estimation of multipath cluster is proposed, which is claimed to achieve better performance than earlier approaches. In [43], a two-dimensional unitary Estimation of Signal Parameters via Rotational Invariance Techniques (ESPRIT) algorithm is employed for AOA estimation in indoor UWB mulitpath environments. In general, however, the resulting algorithms are characterized by very

high computational complexity (as they need to perform focusing, eigenvalue decomposition, etc.) and inadequate estimation performance in dense multipath environments.

Recently, some researchers have proposed to jointly estimate the TOA and AOA at low computational cost using simplified search techniques. These joint estimation schemes normally require the use of a receiver equipped with an antenna array, such as a Uniform Linear Array (ULA) or a Uniform Circular Array (UCA). In [44], a joint TOA/AOA estimator based on time domain smoothing is proposed, where UWB signals from several immediate neighboring elements of the antenna array are averaged over the time domain. In [45], for example, joint estimation is achieved through calculating a two dimensional delay-angle power spectrum within the frequency domain. In [46], a beamforming approach is proposed in which the overlapping effect of secondary images is mitigated by a special form of multipath-aided acquisition that is capable of resolving closely spaced multipath. Meanwhile, TDOA-based AOA estimation methods are adopted in many other works where, in general, TOA estimates are first obtained at each antenna (either via time- or frequency-domain processing), and then used to further extract the desired AOA by processing of the TOAs, e.g., by computing the TDOAs or least-square fitting of the TOAs. In [47, 48, 49], such a frequency domain approach is adopted for the estimation of the TOA and the AOA where in a first step, coarse symbol timing is achieved based on a minimum distance criterion that exploits the knowledge of the TH code, while in the second step, high resolution TOA estimation is performed at each antenna by searching for the maximum of a special power delay profile. In [50], a joint TOA/AOA estimator is proposed for UWB indoor ranging under Line Of Sight (LOS) operating conditions, in which signal samples obtained from an antenna array at the Nyquist rate are processed in a three-step algorithm to produce the desired estimates: the first step estimates the TOAs at the antenna elements, the second step further process these estimates to derive a joint estimate of the main TOA and AOA, while the third step improves the AOA estimate.

Although the AOA estimation performance of these techniques is competitive to early subspace-based schemes [41, 40], especially in dense multipath environments, the imposed processing structure on the AOA estimation limits the achievable accuracy and suggests that other estimators with better performance may exist.

1.2.3 Parameter estimation under multiuser interference

All of the above approaches have been designed specifically under the assumption of a single user system model. However, in practical applications of localization systems, multiple emitters often operate simultaneously in the same radio environment. Consequently, the resulting Multiuser Interference (MUI) can severely degrade the accuracy of the TOA and AOA estimation unless special measures are taken to suppress it or, at least counteract its effects to a sufficient extent. In radio localization systems based on IR-UWB signaling, this can be achieved by exploiting the TH or DS code patterns of the desired user, which are assumed to be known at the receiver.

In [51], the authors develop a TOA estimation method that performs non-linear filtering on the received signal energy to mitigate MUI. In [52], a multiuser AOA estimation technique is proposed using a digital channelization receiver that has the ability to select spectral lines from the desired UWB emitter. In [53], a TOA estimator is proposed that can reduce MUI in weak Non Line-Of-Sight (NLOS) environments based on the Expectation Maximization (EM) and pseudo-quadratic ML algorithms. In [54], TOA estimators based on the ML criterion with interference cancellation are proposed, but they are mainly based on a single-path model.

Currently, and to the best of our knowledge, there are not many works on parameter estimation for IR-UWB localization under MUI, especially on AOA estimation, therefore leaving an open research area to be filled.

1.3 Thesis objectives and contributions

The aim of the proposed research is to develop improved parameter estimation algorithms for wireless localization systems based on IR-UWB signaling. To be more specific, the main goal is to develop high accuracy estimators for location related parameters such as TOA and AOA, but with reasonable complexity and cost of implementation.

For TOA estimation, as we elaborated in the previous section, although there are already many works in the literature, certain important aspects of the problem area, such as making partial use of available channel statistics in the estimation process, are still worthy of further developments. Existing estimators which employ channel information either require full channel parameter estimation, which is not practical due to the large number of channel parameters (especially at higher sampling rate where the computational load becomes prohibitive), or simply assume that the required information about the channel parameters is already known. For instance, the sub-Nyquist

sampling ML estimators in [26] can achieve good estimation accuracy, but to function properly, they generally require *a priori* information about the channel, in the form of the APDP, which should be estimated beforehand. As we have been able to verify, a lack of adequate information about the APDP in these methods can significantly deteriorate the performance of the TOA estimator. We are therefore interested in exploring the use of realistic channel model information as an aid to TOA estimation or IR-UWB signals, without significantly increasing the computational complexity of the resulting processor. That is, we aim at using and estimating relevant channel information, and especially the APDP, to efficiently benefit the final TOA estimation.

Besides its potential application in ML-based TOA estimation, the APDP is an important characteristic of the UWB channel in its own right. Indeed, it can provide useful information about the characteristics of the multipath radio channel, including the presence of dominant scatterers in the vicinity of the UWB transmitter as well as the reflection/absorption properties of the surrounding environment [55]. Despite its importance, the estimation of the APDP from a statistical signal processing perspective has not yet been extensively explored.

With regard to AOA estimation, our main interest lies in approaches where the TOA and AOA are estimated jointly at low to moderate computational cost. These approaches are of practical interest not only because of their low complexity, but also because they can simultaneously obtain the AOA and TOA parameters, which are the ultimate parameters needed for radio localization. As mentioned earlier, estimation of the AOA normally requires the use of a receiver equipped with an antenna array, but this in turn opens a new real of possibility from a statistical signal processing perspective. While recently proposed schemes offer competitive performance, they are ultimately limited by the specific structural choices made in their derivation. Furthermore, as in the case of TOA estimation, these estimators do not take full benefit of the temporal characteristics of the multipath radio channel. Specifically, in the case of AOA estimation and to the best of our knowledge, few works currently attempt to exploit knowledge of the APDP in the estimation. Hence, there is still room to improve the final accuracy of the joint TOA/AOA estimates and we are interested in deriving and studying the properties of such an improved algorithm, which can achieve a better performance as well as requiring a low complexity.

Finally, since parameter estimation under MUI is currently not fully developed, our goal is to provide an effective joint AOA and TOA estimator to fill this gap. Specifically, we are interested in deriving joint estimators that are better equipped to mitigate MUI, specifically by exploiting knowledge of the time hopping codes of the different user signals at the receiver.

A summary of the research contributions presented in this thesis is presented below.

1. *Development of a novel TOA estimator for IR-UWB impulse radio systems that exploits APDP information:* Specifically, we derive a sub-Nyquist ML-based TOA estimator that employs specific knowledge of the UWB channels in the form of the APDP. However, instead of assuming a known APDP, as in previous works, we propose and investigate a joint estimator of the TOA and the APDP. At first, a simple exponential model is used for the APDP and its parameters are estimated; the estimated APDP is then used to form a likelihood function and obtain the ML-based TOA estimate.

2. *Introduction of a more sophisticated multi-cluster model for the APDP:* In practice, the APDP of a dense multipath UWB channel usually consists of several clusters, each with a specific exponential decay rate. A low-dimensional parametric model of this type is therefore investigated as a generalization to the simple exponential model used above. The parameters of this model are estimated via an original Least Square (LS) fitting approach; then, the estimated APDP is used as above in a likelihood function to obtain the ML estimate of the TOA. The newly proposed LS-based APDP estimator can also help boost the performance of previously reported TOA estimators.

3. *Performance evaluation of the newly proposed joint TOA and APDP estimation schemes:* Performance in the presence of Inter Frame Interference (IFI) of the proposed schemes is also discussed. We derive the CRBs on the variance of both TOA and APDP parameters, which are then used to benchmark the performance of the proposed estimators.The performance of the proposed sub-Nyquist ML estimator along with single and multiple APDP estimation (including single and multiple exponential models) is evaluated through exhaustive numerical simulations under realistic conditions of propagation based on well established UWB channel models, and comparisons are made to benchmark approaches from the recent literature. The results clearly demonstrate the advantages of the new TOA estimator as well as the usefulness of the proposed APDP estimation.

4. *Development of a low complexity joint TOA and AOA estimator for antenna array receivers:* We propose an original model for the UWB channel, in which the pulse image from the primary path is modeled as a deterministic component while the superposition of the images from the secondary paths are modeled as a Gaussian random process. A special gating mechanism models the onset of the secondary paths. By exploiting the properties of this model, we derive a new estimation method which consists of two steps: (1) coarse estima-

tion of the TOA and the APDP followed by (2) joint TOA refinement and AOA estimation by maximization of a novel log-likelihood function (LLF) using the coarse estimates from the first step. We derive a general LLF expression for this problem and expose the processing structure of the joint ML estimator of the TOA and AOA.

5. *Consideration of implementation issues and performance analysis of the newly proposed joint TOA/AOA estimator:* We develop specific approaches for the solution of practical issues related to the implementation of the new estimator, especially the coarse estimation of the TOA and APDP in the first step, and the efficient implementation of the two-dimensional search in the second step. We derive the CRB for unbiased TOA and AOA estimators, taking into account the proposed multipath signal model and its associated gating mechanism. We also investigate the performance of the newly proposed joint TOA/AOA estimator and demonstrate that it outperforms a benchmark approach from the recent literature. Our results are based on multipath UWB channel models featuring both diffuse and directional secondary image fields, and include comparison to the CRB as well.

6. *Extension of the above joint TOA/AOA estimator to the multi-user framework:* This is equivalent to the consideration of a Multiple-Input Multiple-Output (MIMO) scenario, which is more challenging than the previous two system models. In this case, both the multipath propagation of the desired signal itself and signals from multiple emitters will interfere with the desired signal, and thus largely degrade the estimation. Traditionally, to alleviate the hardware cost at the receiver, non-coherent approaches have been adopted. In this work, we extend the previous joint estimator of the TOA and AOA estimator in dense multipath UWB environments, so that it may counteract the MUI and succeed in the parameter estimation task. Specifically, we propose a MUI mitigation technique which exploits the knowledge of the desired user's TH code to time-align the received signal at the receiver. We then show how the above joint TOA/AOA estimator can be applied to this time aligned signal by properly compensating for the residual interference power in the log-likelihood based energy filter. The validity of this proposed MUI mitigation scheme is thoroughly demonstrated through simulation experiments considering practical conditions of operation, including multiple users with non-equal power (i.e., near-far effect) as well as dense multipath propagation.

Parts of the research presented in this thesis have been published or submitted for publication

in peer-reviewed journals and refereed conferences, as listed below:

Journal papers:

[J-1] F. Shang, B. Champagne and I. Psaromiligkos, "Time of arrival and power delay profile estimation for IR-UWB systems," *Signal Processing*, vol. 93, no. 5, May. 2013, pp. 1317-1327.

[J-2] F. Shang, B. Champagne and I. Psaromiligkos, "Joint ML based estimation of time and angle of arrival for UWB localization in multipath environments," submitted to *IEEE Trans. Wireless Communications*, April 2013, currently under revision.

[J-3] F. Shang, B. Champagne and I. Psaromiligkos, "Joint ML based estimation of time and angle of arrival for UWB localization in multipath environments," to be submitted to *IEEE Communications Letters,* Nov. 2013.

Conference papers:

[C-1] F. Shang, B. Champagne and I. Psaromiligkos, "Joint estimation of time of arrival and power profile for UWB localization," in *Proc. 2010 IEEE Int. Conf. on Signal Processing*, Beijing, China, Oct. 2010, pp. 1484-1487.

[C-2] F. Shang, B. Champagne and I. Psaromiligkos,"Joint estimation of time of arrival and channel power delay profile for pulse-based UWB systems," in *Proc. 2012 IEEE Int. Conf. Communications*, Ottawa, Canada, Jun. 2012, pp. 4515-4519.

[C-3] F. Shang, B. Champagne and I. Psaromiligkos,"A novel ML-based joint TOA and AOA estimator for IR-UWB systems," in *Proc. 2013 IEEE Int. Conf. on Acoust., Speech, and Signal Processing*, Vancouver, Canada, May 2013.

1.4 Thesis organization

Chapter 2 presents an up-to-date review of IR-UWB signaling technology, with focus on the localization problem and associated parameter estimation. A detailed overview of IR-UWB signaling is first presented, along with the background mathematical framework needed for the characterization of pulse modulation and multi-access schemes. UWB channel models based on IEEE 802.15.4a are then introduced with the consideration of various environments, including

both LOS and NLOS. Current approaches available for the localization of an UWB emitter are explained along with their advantages and disadvantages. Finally, selected parameter estimation techniques from the recent literature are reviewed in detail.

Chapter 3 presents a novel TOA estimator for IR-UWB impulse radio systems that exploits APDP information. We first introduce a detailed system model for estimating TOA in the case of a single user and a receiver equipped with a single antenna. The novel ML-based TOA estimator is obtained by modeling the channel impulse response as a Gaussian random process with second-order characterization in the form of the APDP. The latter is modeled as comprising a single or multiple exponentially decaying components and a LS fitting approach is proposed for the estimation of its parameters. The performance of the proposed joint TOA and APDP estimator is finally examined under different conditions, including channel models, sampling rates, etc.

In Chapter 4, a new joint ML-based TOA and AOA estimator for antenna array receivers is developed and investigated. An original channel model is first assumed, in which the channel impulse response is separated into two parts as explained in the previous section. A new log likelihood function (LLF) is derived based on this model and used to develop a joint estimator in two steps: coarse TOA estimation followed by localized two-dimensional search of the LLF. The computational complexity of this estimator is analyzed, along with the consideration of important implementation issues. The CRB on estimator variance is derived, and finally, the performance of the newly proposed scheme is investigated through Monte Carlo simulations, with comparisons to earlier competitive schemes.

In Chapter 5, we consider the extension of this joint TOA/AOA estimator to the multiuser case, where the proposed design strategy includes three steps. The first step aims to reduce MUI by alignment of the received signal over multiple symbols and frames using the knowledge of TH codes and training sequence at the receiver. The second and third steps then involve coarse TOA estimation followed by two-dimensional search for the maximum of a LLF. These steps are similar to those in Chapter 4, but subtle modifications are made to the noise power to take into account the residual level of interference after alignment. Finally, the behavior of the proposed estimator is examined by simulation experiments.

Finally, Chapter 6 briefly summarizes the thesis, presents some concluding remarks and provides suggestions for future work.

Chapter 2

Background on Parameter Estimation for IR-UWB Localization

In this chapter, a comprehensive technical description of IR-UWB systems is given, with the main focus on localization aspects. In Section 2.1, IR-UWB signaling is reviewed in detail, including the choice of different pulse types, time-based digital modulation and multiple-access schemes. In Section 2.2, reference UWB channel models are presented as per the IEEE 802.15.4a standard. Various localization techniques and related physical parameters suitable for UWB systems are explained in Section 2.3. Finally, some representative works on parameter estimation for IR-UWB localization are briefly reviewed in Section 2.4.

2.1 IR-UWB signaling for localization applications

IR-UWB signals are especially well suited for short-range localization due to their high timing accuracy and low-cost hardware circuitry. Indeed, because of their extremely short pulse duration (i.e., $<$ 1ns duration, equivalent to $>$ 1GHz bandwidth), IR-UWB signals can achieve a localization accuracy or spatial resolution, in the centimeter range. Furthermore, the electronic transceiver circuitry for generating and processing the modulated pulse sequence can often be realized at low-cost using Complementary Metal Oxide Semiconductor (CMOS) technology [56, 57]. However, since the transmitted power spectrum of the UWB signal is limited by the FCC mask [6], UWB ranging and localization is mainly applicable over short distances, such as in indoor and confined areas.

A transmitted IR signal consists of a modulated sequence of individual pulse waveforms, also called monocycles. While many different types of monocycles exist, they share a common distinguishing feature in that each transmitted ultra-short pulse instantaneously occupies the whole UWB bandwidth. With the transmitted PSD strictly limited by FCC rules, the goal of the pulse shape design is to achieve optimal utilization of the spectral mask (as illustrated in Fig. 1.1) while minimizing interference to other wireless systems. The most often used types of monocycles include Gaussian derivatives, Rayleigh, Laplacian, cubic and modified Hermitian [58]. These often refer to parametric families of pulses, with a generic waveform shape derived from a given mathematical expression, but characterized by different parameters that can be varied to control certain shape factors, such as amplitude, duration, frequency content. Generally, monocycles that can be easily generated are adopted widely, while the rule of thumb is to aim for a nearly flat frequency spectrum.

One of the most often used pulse shapes is the Gaussian doublet, which is defined as the the second derivative of a Gaussian pulse, the latter borrowing its shape from the well-known Gaussian probability density function. Specifically, the Gaussian pulse is given by the bell-shape function

$$w_0(t) = \frac{1}{\sqrt{2\pi\sigma^2}} e^{-t^2/2\sigma^2} \tag{2.1}$$

where t denotes the continuous time, σ is the standard deviation or pulse spread and a zero-mean is assumed. The Gaussian doublet, obtained as the second derivative of $g(t)$ with respect to time t, is shown plotted in Fig. 2.1 in the time domain, along with its amplitude spectrum in the frequency domain, where the value of σ =0.45ns. For the Gaussian derivative family of monocycles, it is observed that the center frequency f_c increases whereas the bandwidth decreases as the order of the derivative increases [59]. Generally, higher-order derivatives show better fitting to the FCC spectral mask but for ranging application, a wider spectrum (i.e. low-order derivative) is favored since it can provide higher localization accuracy. However, the trade off between bandwidth and implementation complexity should always be considered.

In practice, a pulse train which consists of a sequence of non-overlapping, digitally modulated monocycles is emitted at the transmitter. In this case, the spectrum of a pulse train would not be as smooth as that of the single pulse shown in Fig. 2.1. Instead, spectral lines are introduced due to the repetitive nature of the continues pulse transmission [60], that is, the overall spectrum envelope is similar to that of a single pulse, but the fine details of the spectral shape becomes very irregular due to the presence strong spectral lines at multiples of the pulse repetition frequency.

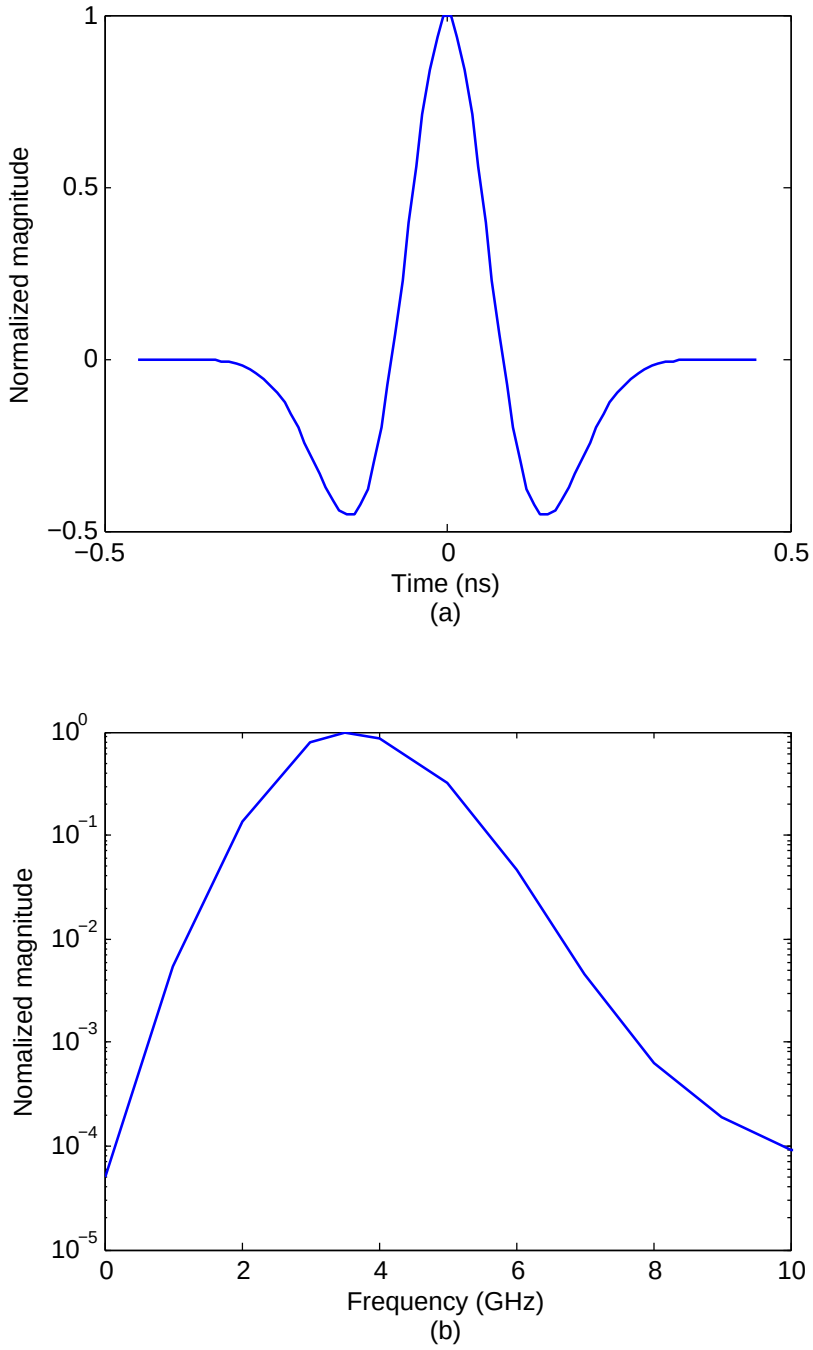

Fig. 2.1 Gaussian doublet: (a) pulse shape for $\sigma = 0.45$ns; (b) corresponding amplitude spectrum

To reduce the amplitude level of these spectral lines, various randomization techniques can be employed. For instance, randomizing the position of each pulse by a small time shift around pulse width, will tend to spread the energy spikes spread over the frequency, thereby smoothing out the amplitude spectrum. The most common way to randomize the UWB pulse train is by using a Pseudo-Random (PR) sequence to determine the time shifts applied to the individual pulses, as further explained below [61].

In addition to reducing spectral peaks, pseudo-random codes can be used as a means to implement a multiple access scheme, whereby IR signals from different users can be separated at the receiver. In this scheme, each user owns a unique random code, which is different from (and ideally orthogonal to) that of other users. The receiver, which observes a superposition of the pulse trains emitted by multiple users, can recover the one emitted by a specific user simply by using its corresponding code sequence and applying a reverse time shifting operation on the received signal; following this operation, the pulse train from the desired user is preserved while those from other users appears as low-level white noise [58].

There are mainly two different multiple access schemes that can be employed with IR-UWB signaling, namely: Time Hopping (TH) and Direct Sequence (DS). In order to explain their operation, we first note that in IR-UWB signaling, the time axis is divided into symbol periods consisting of N_f pulse repetition periods of duration T_f, each of which is called a *frame*. Within each frame a single pulse is transmitted. In TH-UWB systems, each frame is further divided into $N_c > 1$ smaller time slots of duration T_c, each one providing a possible instant for pulse transmission. For a symbol of N_f frames, the TH code length is usually set to N_f and the IR-UWB signal transmitted by the kth user can be written as

$$s_k(t) = \sum_{j=0}^{N_f-1} w(t - jT_f - c_k(j)T_c) \tag{2.2}$$

where $w(t)$ is the pulse waveform, $T_c = T_f/N_c$ is the chip interval and $c_k(j) \in \{0, \ldots, N_c - 1\}$ is the pseudo-random code sequence identifying user k. DS-UWB is much like the conventional DS spread spectrum technique employed in 2nd generation wireless systems. The random code assigned to a particular user serves to spread the data bit into multiple chips, now a chip is now identified with the pulse repetition period. Again, assuming that each symbol or data bit is

represented by N_f pulses, the transmitted signal of one such symbol can now be written as

$$s_k(t) = \sum_{j=0}^{N_f-1} w(t - jT_c)c_k(j) \tag{2.3}$$

where $w(t)$ is the pulse waveform, $T_c = T_f$ and $c_k(j) \in \{-1, +1\}$.

Different data modulation techniques are available for IR-UWB systems, such as Pulse Position Modulation (PPM), Pulse Amplitude Modulation (PAM), Binary Position Modulation (BPM), Orthogonal Pulse Modularization (OPM) and On-Off Keying (OOK) modulation [62]. PPM is a time-based modulation scheme, in which, depending on the information symbol, each pulse is delayed or advanced by a small time shift, denoted here as T_p such that $T_p < T_c$. Simple IR-UWB transceivers can be designed by combining a selected modulation technique with the chosen multiple access scheme. However, certain constraints apply; for instance, while TH-UWB can be used with PAM and PPM, it is not suitable for OOK.

In the TH-PPM combination, which is the most commonly employed in the literature, the transmitted IR-UWB signal takes the form

$$s_k(t) = \sum_{i=0}^{N_b-1} \sum_{j=0}^{N_f-1} w(t - jT_f - c_k(j)T_c - a_k(i)T_p)) \tag{2.4}$$

where N_b is the number of transmitted bits and $a_k(i) \in \{0, 1\}$ is the binary data sequence. An example of such a signal is shown in Fig. 2.2, where $N_b = 2$, $N_c = 3$, $N_j = 5$, $T_f = 3$ns, $T_c = 1$ns and $T_p = T_c/2 = 0.5$ns is the time shift of the PPM modulation. In this particular example, the TH code sequence is $c_k(j) = [1, 2, 2, 2, 1]$, the transmitted bits are $a_k(i) = [1, 0]$ and a Gaussian doublet pulse shape is used for $w(t)$.

In contrast to PPM and BPM, which are time-based techniques, all other forms of modulation are shape-based techniques. Among them, PAM is a popular one in which the binary data sequence is used to control the amplitude of each pulse. The simplest case of PAM is the Binary Pulse Amplitude Modulation (BPAM), in which the pulse amplitude takes either a positive or negative value (say ±1 Volt), depending on the binary data at that instant. In [62], simulation studies show that IR-UWB systems using TH-BPAM have better performance than TH-PPM and TH-OOK over the Additive White Gaussian Noise (AWGN) channel if there is a jamming signal. Based on Bit Error Rate (BER) calculations, this reference even provides an order of performance of the studied combination of multiple access schemes and modulation techniques

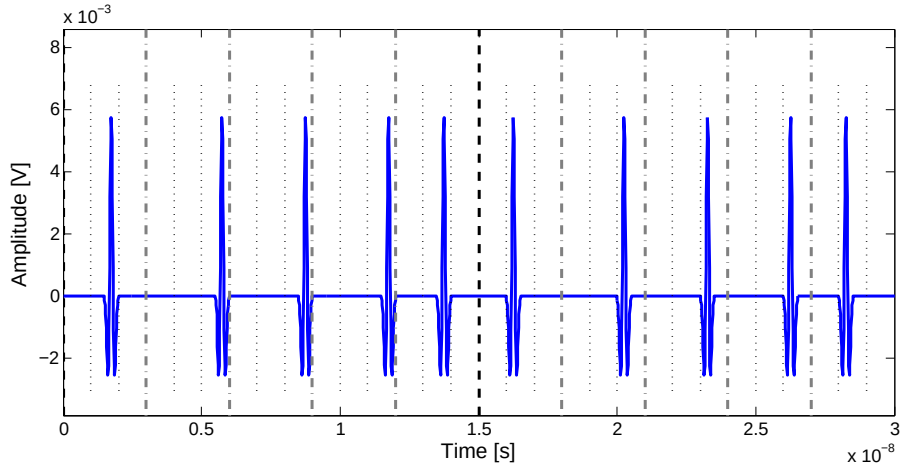

Fig. 2.2 Time window of 2 data bits for PPM modulation with TH spreading

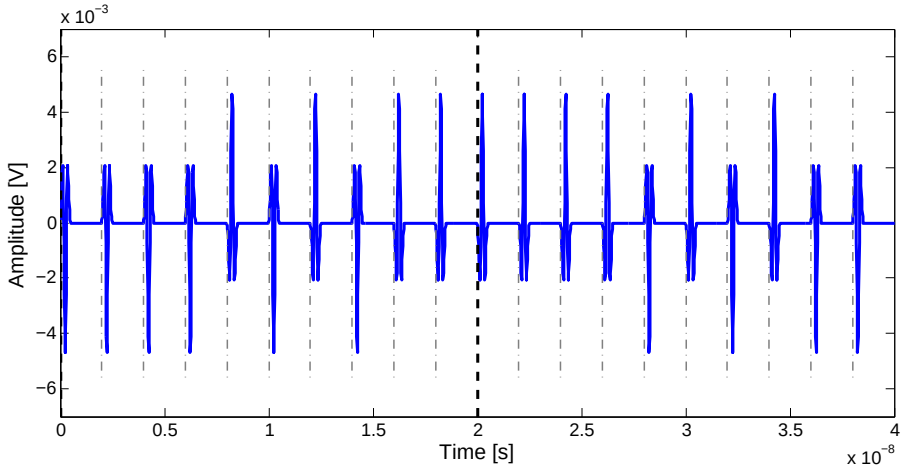

Fig. 2.3 Time window of 2 data bits for BPAM modulation with DS spreading

over the AWGN channel: TH-BPAM followed by DS-BPAM, TH-PPM and then DS-OOK. In the DS-BPAM combination, the transmitted signal is

$$s_k(t) = \sum_{i=0}^{N_b-1} \sum_{j=0}^{N_f-1} w(t - jT_c)c_k(j)a_k(i) \tag{2.5}$$

An example of a 2-bit DS-BPAM signal is illustrated in Fig. 2.3, where $N_b = 2$, $N_c = 1$, $N_j = 10$, $T_f = T_c = 2ns$, $a_k(i) = [-1, +1]$ and $c_k(j) = [+1, +1, +1, +1, -1, +1, -1, +1, -1, -1]$.

Since the main focus of this thesis is on parameter estimation, as opposed to data transmission, we shall limit our discussion of IR-UWB signaling to the above and skip the details about the other modulation schemes; however, the interested reader may consult one of the many good references available on this topic, such as [61, 58, 63].

2.2 Reference models for UWB channel

One distinguishing feature of the UWB channels in localization applications (especially indoor and short range outdoor) is their extremely rich multipath structure. As such, they are well suited for characterization with the Saleh-Valenzuela (SV) model or modifications thereof [64]. In the conventional SV model, the multipath rays arrive in clusters, where the cluster onset and ray arrival times within each cluster are described by two independent Poisson processes. In addition, the average power of successive clusters and rays vary according to a doubly exponential Power Delay Profile (PDP). The choice of the model parameters, especially the rates of the Poisson processes and the exponential decay factor, provide great flexibility to model different environments. Consequently, many experimental studies have been devoted to characterizing the UWB channel in light of the SV model.

The first experimental results on the measurement of the UWB propagation channel and impulse response in typical office buildings are presented in [65], where a signal bandwidth in excess of one GHz is employed. In addition to revealing the dense multipath structure and strong path loss attenuation of these environments, the results also demonstrate that UWB signals do not suffer from fading. Indeed signal fading is due to the overlapping superposition of unresolved multipaths, which is partly avoided due the use of short duration pulses. Hence, the UWB fade margin is only 3-4dB, as compared to 30-60dB for narrowband radio communications. Based on the properties of multipath profiles measured in different rooms of a modern office building over a finely spaced measurement grid, [66] further establishes a statistical model for UWB channels. This analysis leads to the formulation of a so-called Stochastic Tapped-Delay-Line (STDL) model, which take into account several physical features of the UWB channel, including the APDP, small-scale statistics and shadowing. In particular, it is found that the APDP can be well-described by a single exponential decay with a statistically distributed decay constant.

In recent years, many other experimental measurement campaigns have been undertaken, considering different radio environments. In [67], channel measurements are taken in both the time and frequency domains in a university hospital and the resulting parameters extracted from

the measurement data are compared with a modified SV model. In [68], the results of UWB measurements conducted in two industrial environments are presented. Again, the energy arrives in clusters, and the large amount of metallic scatterers present in the factory causes dense multipath scattering, which can be characterized by a generalized Saleh-Valenzuela model. Reference [69] investigates and summarizes some fundamental properties of UWB channels. In particular, it is found that if the relative bandwidth is large, the propagation processes, including path loss and shadowing, become frequency-dependent, while if the absolute bandwidth is large, the impulse response can become sparse and the fading depth is smaller.

The results of these and other similar works were combined and contributed to the final report of the IEEE 802.15 Channel Modeling Subgroup [70]. As mentioned before, the main IEEE standards for UWB radio channels are based on the works of the IEEE 802.15.3a and IEEE 802.15.4a Task Groups. While the former was originally intended for high data rate WPAN, the latter has been focusing on low data rate WPAN as well as source localization. The channel model proposed under IEEE 802.15.3a consists of 4 different scenarios, defined in terms of 7 key parameters. These are based on the SV model, where multipath rays arrive in clusters, with amplitude following a doubly-exponential decaying profile. IEEE 802.15.4a proposes 9 channel models for different frequency ranges and environments [6]. In particular, both the LOS and NLOS situations are considered for indoor residential, indoor office, industrial, while only NLOS is considered for open outdoor environments.

The generic channel models proposed for localization applications in IEEE 802.15.4a can be used for both the 0.1-1GHz and the 2-10 GHz ultra-wide frequency bands. The key features of these model include the following components:

- Pathloss as a function of distance d characterized by a d^{-n} law, with frequency dependent pathsloss exponent n.
- Use of a modified SV model for the multipath delay profile: paths arrive in clusters; mixed Poisson distribution for ray arrival times; cluster decay rate may depends on delay; Power Delay Profile (PDP) is allowed to first increase, then decrease.
- Small-scale fading is described by Nakagami-distribution, with different m-factors for different components.
- Block fading, i.e., propagation channel stays constant over data burst duration.

The pathloss, which is defined as the power ratio between the received and transmitted signals, serves as a key parameter for radio channel models. For UWB systems, pathloss not only depends on the distance the signal travels, but also on the frequency band of operation due to the very large bandwidth available for signal transmission. Indeed, frequency-dependent effects can not be ignored, i.e. the frequency components of a UWB signal propagate quite differently in the lower and upper bands of the spectrum. Let PL(d, f) denotes the pathloss as a function of the distance d and frequency f. The effect of these parameters can be treated independently, as in PL(d, f) = PL(d)PL(f), where PL$(f) \propto f^{-2m}$ and P$L(d) \propto d^{-n}$, and the decaying factors m and n depend on the environment. In addition to the decay factors, there are three other passloss related parameters in IEEE 802.15.4a for a typical UWB model, that is: pathloss at 1m distance PL_0, shadowing standard deviation σ_s and attenna loss A_{ant}

Shadowing, or large scale fading, characterizes the (slow) variations of the local received signal power around value predicted from the pathloss. Taking this effect into account, the net passloss in dB (averaged over small-scale fading), can be written as

$$\mathrm{PL}(d) = \mathrm{PL}_0 + 10n \log_{10}(\frac{d}{d_0}) + S \tag{2.6}$$

where the reference distance d_0 is set to 1m and S is a Gaussian-distributed random variable, with zero mean and standard deviation σ_s, used to model shadowing.

Small scale fading is a characteristic of radio propagation resulting from the presence of reflectors and scatterers that cause multiple versions of the transmitted signal to arrive at the receiver with different amplitudes, phases, TOA and AOA, thereby creating constructive or destructive interference as a function of the receiver position in space. In the IEEE 802.15.4a reference models, the complex baseband channel impulse response follows a modified SV model. The cluster arrival times are modeled as a Poisson process where the decay factor of each cluster depends on its onset (or arrival) time, while the ray arrival times within a cluster obey a mixed Poisson distribution. Accordingly, the impulse response in the complex baseband domain, is given by

$$h(t) = \sum_{l=0}^{L_c-1} \sum_{k=0}^{K-1} \alpha_{k,l} e^{j\phi_{k,l}} \delta(t - T_l - \tau_{k,l}), \tag{2.7}$$

where L_c is the number of clusters, K is the number of paths in each cluster, $\alpha_{k,l}e^{j\phi_{k,l}}$ is the complex gain (amplitude and phase) of the kth path of the lth cluster, T_l is the arrival time of

the lth cluster and $\tau_{k,l}$ is the delay of the kth of the cluster k path relative to T_l. The phases $\phi_{k,l}$ in (2.7) are uniformly distributed in the range $[0, 2\pi)$ and the amplitude $\alpha_{k,l}$ are positive random variables with a Nakagami distribution. In above model, only the amplitude, phase and arrival time are taken into consideration. While in practice this is adequate for single antenna receiver, AOA should also be incorporated in the UWB channel model when dealing with antenna array receivers. This aspect will be discussed in further detail in Chapter 4.

The number of clusters L_c in (2.7) follows a Poisson distribution, with probability mass function given by

$$P_{L_c}(l) = c\frac{(\bar{L}_c)^l e^{-\bar{L}_c}}{l!}, \quad l \in \{0, 1, \ldots\} \tag{2.8}$$

where the mean $\bar{L}_c$ depends on the environment. The cluster arrival times are modeled as a Poisson process, with conditional Probability Density Function (PDF).

$$f(T_l|T_{l-1}) = \Lambda_l e^{-\Lambda_l(T_l - T_{l-1})}, \quad l \in \{1, \ldots, L_c\}, \quad T_l > T_{l-1} \tag{2.9}$$

where Λ_l is the cluster arrival rate, which depends on the environment. The path arrival times in each cluster are modeled as a mixture of two Poisson processes, with conditional PDF as follows

$$\begin{aligned} f(\tau_{k,l}|\tau_{k-1,l}) = {} & \beta\lambda_1 e^{-\lambda_1(\tau_{k,l} - \tau_{k-1,l})} \\ & + (1-\beta)\lambda_2 e^{-\lambda_2(\tau_{k,l} - \tau_{k-1,l})}, \quad k \in \{1, 2, \ldots, K\}, \end{aligned} \tag{2.10}$$

where β is the mixture probability, with $0 \leq \beta \leq 1$, and the path arrival rates $\lambda_1 > 0$ and $\lambda_2 > 0$ depend on the environment. Note that for each cluster, $\tau_{0,l} = T_l$.

In the IEEE 802.15.4a UWB reference model, the Power Delay Profile (PDP) $P(\tau)$ is defined as the instantaneous average power of the channel response as a function of the propagation delay *tau*, to an impulse emitted at time $\tau = 0$. Considering the discrete nature of the channel impulse response in (2.7), this information is captured by computing the average power of the kth path of the lth cluster, i.e. $P(\tau) = E\{\alpha_{k,l}^2\}$, where the arrival time is $\tau = T_l + \tau_{k,l}$. The PDP decays exponentially within each cluster, as given by:

$$E\{\alpha_{k,l}^2\} = \Omega_l \frac{1}{\gamma_l[(1-\beta)\lambda_1 + \beta\lambda_2 + 1]} e^{\tau_{k,l}/\gamma_l} \tag{2.11}$$

where Ω_l is the integrated energy of the lth cluster and γ_l is the intra-cluster decay time constant, which linearly increases with T_l. The integrated energy Ω_l, which represents an average value

over the cluster shadowing and the small-scale fading, follows in general an exponential decay, i.e., it satisfies the following relation after taking a log operation:

$$10\log_{10}(\Omega_l) = 10\log_{10}(e^{-T_l/\Gamma}) + M_{cl} \tag{2.12}$$

where Γ is cluster decay time constant and M_{cl} is a normally distributed random variable, both of which being dependent on the environment.

For some NLOS environments (office and factory), the shape of the PDP can be different, as given by

$$E\{\alpha_{k,l}^2\} = (1-\chi e^{-\tau_{k,l}/\gamma_{rise}})e^{-\tau_{k,l}/\gamma_l}\frac{\gamma_l+\gamma_{rise}}{\gamma_l}\frac{\Omega_l}{\gamma_l+\gamma_{rise}(1-\chi)}. \tag{2.13}$$

In (2.13), the PDP first increases and then decreases as a function of the path index k. The parameters $0 < \chi \leq 1$, γ_{rise} and γ_l control the attenuation of the first few components, the rate of increase of the PDP to its maximum, and the decay rate of the PDP after reaching its maximum, respectively.

In addition to parameters controlling the pathloss, shadowing and PDP, auxiliary parameters of interest include the first arrival time τ_A, the mean excess delay τ_E, the root mean square delay spread τ_{rms}, the maximum excess delay τ_M, and the peak to lead delay τ_{pld}, which measures the time lag between the first and the strongest multipath component (MPC). For LOS channels, it is possible for the first arriving path to be the strongest one, which is very desirable in localization applications. For NLOS channels, τ_{pld} has a heavy-tailed distribution, which can potentially cause large localization errors.

The impulse responses of UWB channels in different environments can be quite different, as illustrated below. The case of a residential LOS situation in terms is depicted in Fig. 2.4, where the MPC are well separated and grouped in a few clusters. In this case, the first MPC happens to be the strongest one In contrast, Fig.2.5 depicts the UWB impulse response of an industrial NLOS environment. The maximum magnitude appears after about 40ns while the first few MPC are strongly attenuated. We note that the tail of the response in Fig.2.5 is much longer than that of the response in Fig.2.4.

For the frequency band from 2 to 10GHz, each channel model in the IEEE 802.15.4a classification corresponds to a specific environment, as summarized in the Table 2.1 for future reference. These channel models are widely applied by researchers working on UWB localization systems and algorithms, since the parameter values used for the generation of the corresponding channel

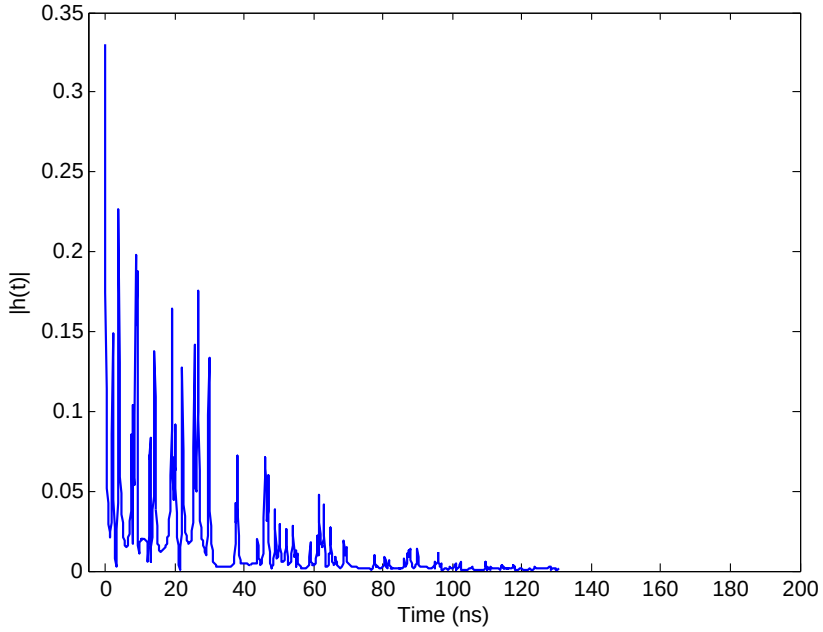

Fig. 2.4 Impulse response realization in CM1 (residential LOS)

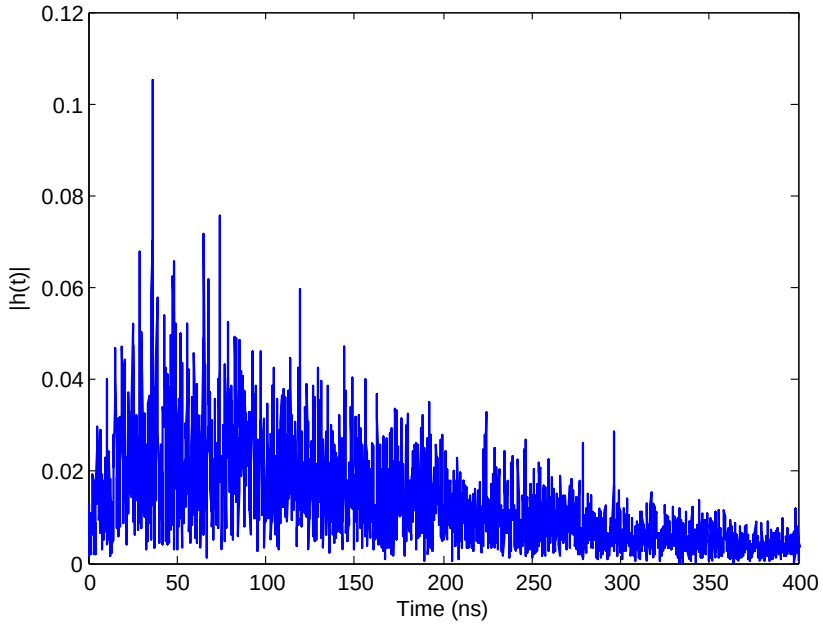

Fig. 2.5 Impulse response realization in CM8 (industrial NLOS)

responses have been obtained through extensive experimental measurements and analysis.

Table 2.1 Comparison of IEEE 802.15.4a standard channel models

Model name	Description	Range	Frequency
CM1	Residential LOS	7–20m	2–10GHz
CM2	Residential NLOS	7–20m	2–10GHz
CM3	Office LOS	3–28m	2–8GHz
CM4	Office NLOS	3–28m	2–8GHz
CM5	Outdoor LOS	5–17m	3–6GHz
CM6	Outdoor NLOS	5–17m	3–6GHz
CM7	Industrial LOS	2–8m	2–8GHz
CM8	Industrial NLOS	2–8m	2–8GHz
CM9	Open outdoor NLOS channel (snow-covered area, farm area)	–	2–8GHz

We note that, although the impulse response ((2.7) are presented in the above description is of continuous-time nature, a corresponding discrete-time version is ultimately obtained from any practical simulation software for the generation of such responses. In a discrete-time model of the impulse response, the time axis is quantized (i.e., divided into bins), where each bin may contribute 1 or more MPC after the Poisson arrival times are rounded to the nearest quantization bin. In many papers, (2.7) is therefore simplified as

$$h(t) = \sum_{l=0}^{L-1} \alpha_l e^{j\phi_l} \delta(t - \tau_l), \tag{2.14}$$

where $\alpha_l e^{j\phi_l}$ is the complex gain of the lth MPC, $\tau_l = lT_b$ is the corresponding delay, T_b is the time quantization step, and t is now a discrete-time variable, i.e. multiple of T_b.

While the use of the reference channel models proposed by IEEE 802.15.4a is the favored approach for channel simulation in many research works, the above tapped delay line model is also widely used in theoretical analysis and simulation experiments, and has therefore motivated further experimental work. In [18], the results of two indoor channel measurement campaigns are presented. The authors consider the small-scale fading distribution for the tap amplitudes α_l of the discrete-time baseband-equivalent channel impulse response and investigate the correlation

between adjacent taps. For UWB channels, it is found that channel taps can still be modeled by means of complex Gaussian distribution, despite the much larger bandwidth and the corresponding high temporal resolution. Although the individual channel taps remain correlated to some extent, it is proved that the temporal correlation is weak between most taps. In practice, when applying (2.14), the complex channel gains remain fixed over the channel coherence time, while channel realizations obtained at different coherence periods are statistically independent. Further details about the tapped-delay-line model (2.14) will be provided in the next chapter.

2.3 Position estimation techniques

GPS, the technology behind most outdoor geolocation tracking systems, is not able to provide position estimates inside buildings or in dense urban environments. This is simply because the GPS signal is not able to penetrate through most materials, and it gets blocked or corrupted easily. For these reasons, in indoor environments, localization using radio signals is used instead of GPS. Source localization through the use of narrowband or wideband signals relies on radio transmissions between of two types of nodes: fixed infrastructure (anchors or tag readers) with known positions and mobile devices (agents or tags) with unknown positions [71, 72]. A localization system obtains the position of agents through estimation of ranging parameters from the received signals and, in many cases, additional *a priori* information. However, precise position localization is still a challenging task, especially in harsh indoor environments due to radio blockage (where multipath fading can be a problem). UWB technology is becoming the most attractive candidate for indoor localization [14, 73] due to its obstacle-penetration capabilities and fine delay resolution. Since the bandwidth of most UWB systems is more than 2-3GHz, the ranging accuracy can achieve centimeter level. By further combining both location and control, the positioning system can sense people or machines in various environments. Typical applications include asset and inventory tracking in warehouses or car tracking in a large car park, people tracking or identification in offices, industrial factories, sports or even entertainment events.

A representative case of UWB positioning is UWB-based RFID positioning. As an electronic tagging technology, RFID uses radio wave communications to automatically identify and track the target in LOS environments, however, RFID technology can also be modified to work in NLOS environments. Future advanced RFID systems are expected to provide both identification and accurate localization (at the centimeter-level) of objects with extended operating range (hundreds of meters) while maintaining low power consumption and low cost. Due to their

characteristics such as very wide frequency spectrum and thus high-definition ranging capability, multiple-access capability, low power demands, low complexity and thus low cost, IR-UWB signals are very suitable for future RFID systems. Indeed, recently, UWB techniques and especially IR-UWB radio signals have been successfully applied in RFID systems [74, 75]. In addition, UWB-RFID chipsets based on CMOS technology are already available; recently, passive chipless UWB-RFID localization systems have also been proposed [76].

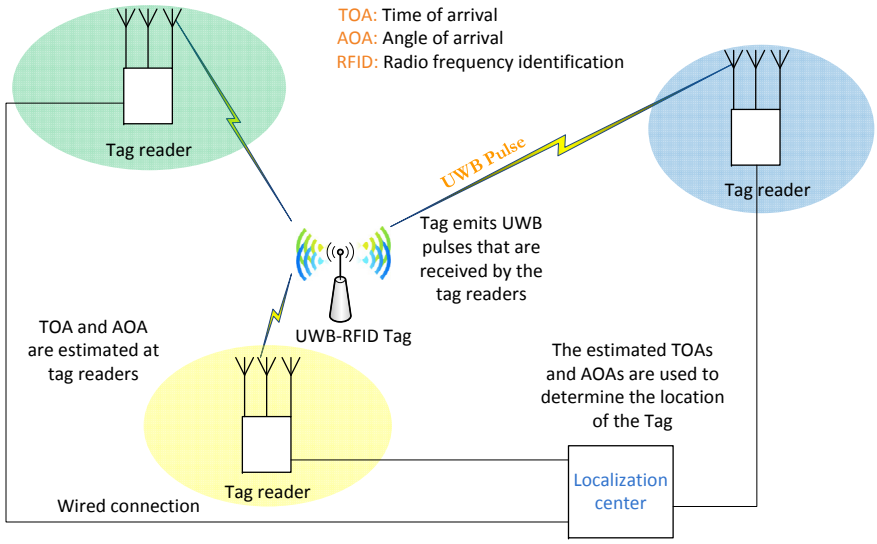

Fig. 2.6 UWB-RFID localization system

Fig. 2.6 depicts a typical UWB based RFID system. Pulse trains are transmitted from the tag, and received by multiple tag readers. In general, RFID may refer to both (semi-) passive and active situations, where in the first case the tag is powered by incoming radio waves emitted by the tag reader through electromagnetic induction, while in the second case it may use a local power source (battery) to emit its own signal; the latter case corresponds to the situation of interest in this work. In terms of range, the active tag can read up to 300 feet or more while the passive tag can read up to 40 feet. Passive tags, which are cheaper, are often used for the monitoring of small objects that come in very large numbers, while active tags are preferred when security or asset values are of consideration.

Most practical positioning systems adopt a two step approach. In the first step, the tag readers

estimate certain parameters from the received signals. The estimated parameters include: TOA, TDOA, AOA[1], and Received Signal Strength (RSS). Furthermore, it is also possible to combine different types of signal parameters to improve the positioning accuracy. At the second step, the estimated parameters are sent to the localization center where, after applying certain optimization algorithms, the position of source tag is finally obtained. The accuracy and structure of the final location estimation is greatly dependent upon the choice and number of underlying parameters (i.e., TOA, AOA, etc.) estimated in the first step. Generally speaking, the higher the number of parameter estimates used, the better the final localization accuracy is. In addition, estimation of these basic parameters can benefit from the incorporation of *a priori* knowledge in the UWB channel model.

RSS-based approaches assume that the relationship between distance and power loss is known. Therefore, after measuring the RSS at the receiver (assuming the transmit power is also known), the distance between the transmitter and the receiver can be calculated. To determine the location of a source node (a tag) on a 2-D plane, 3 reference nodes (tag readers) are needed. According to the CRB [77], it is observed that the best precision depends on channel parameters such as the standard deviation of the shadowing, achievable path loss exponent and the distances between the source node and reference nodes. To be more specific, the lower bound increases linearly with the distances and the standard deviation of the shadowing, and it decreases as the pass loss exponent increases. Therefore, RSS-based approaches can not provide highly accurate position estimates in UWB systems.

Time-based (e.g., TOA and TDOA-based) techniques [23, 78] that capitalize on the utmost advantage of IR-UWB (fine time resolution), are the most popular approaches for UWB indoor localization. In these approaches the distance between two nodes is estimated by measuring the time of flight of a signal that travels between them. Most TOA ranging schemes are based on the timing detection of the first arriving multipath component in the dense multipath channel. If there is a common clock for both the transmitter (source node) and the receivers (reference nodes), the TOA of the received signals can be estimated without clock drift. Similar to RSS-based techniques, 3 reference nodes are needed to locate a source node in a 2-D plane. In the absence of estimation error, the estimated source node location is the intersection of 3 circles, whose radius is calculated from the estimated TOA of each reference node. According to the derived CRB, the accuracy of a TOA measurement in the presence of error can be improved by increasing the SNR or the effective bandwidth [77].

[1] Also called Direction Of Arrival (DOA). In this context, we only use AOA.

If the transmitter and receivers do not share a common clock, there will be a timing offset at the receiver compared to transmitter and TDOA based techniques are used. If the signal transmitted by the source node reaches to 2 reference nodes at different locations, the arrival times will be different: this difference of arrival times is called TDOA. As long as there is a synchronization among all the receivers, which is easy to accomplish, TDOA between receivers can be measured precisely. Generally, two reference nodes are required to obtain one measurement of TDOA. Unlike the TOA, which determines a circle with a known radius, a measurement of TDOA determines a hyperbola on a 2-D plane. Thus 3 reference nodes are needed to determine the location of the source node on the plane given by the intersection of the 2 hyperbolic curves determined by the 2 TDOAs. If we need to localize a source node in a 3-D space, each TDOA determines one half of a two-sheeted hyperboloid and thus 2 TDOAs define a hyperbolic curve. Since the intersection of 3 hyperboloids or intersection of 2 hyperbolic curves can determine a point, 4 reference nodes are required for determining the location of the source node.

The TDOA can be obtained in two ways: we can either estimate 2 TOAs first and compute the deference of the 2 TOAs, or do the cross-correlation of the received signals at two reference nodes over an observation interval and obtain the corresponding TDOA by finding the maximum of the cross-correlation [79]. For the correlator-based method, since the UWB signal travels in a dense multipath environment, the performance will greatly degrade. Therefore, improved methods such as the Generalized Cross-Correlation (GCC) are proposed [80], can be applied to TDOA estimation in the UWB context. In GCC-based TDOA estimation, filtered versions of the received signals are used as the correlator inputs. Therefore, shaping filters should be considered carefully to improve the robustness against noise and multipath.

AOA is another widely used ranging parameter. AOA-based methods measure the direction of arrival of the received signal, i.e., the angle of the straight lines that connect the transmitter and receiver, as taken from a reference direction. These methods require the use of an antenna array configuration and associated circuitry at each reference node (i.e., multi-antenna tag reader). The number of antenna elements used in the array highly depends on the radio environment. In addition, AOA measurements require precise calibration of the antenna circuitry at the reference nodes. In a 2-D plane, 2 reference nodes equipped with antenna arrays are sufficient to locate a source node using an AOA-based approach. The location of the source node is simply the intersection of the 2 connecting lines with estimated angles. Unlike time-based approaches, AOA-based approaches do not require strict synchronization or clock precision among nodes. However, the use of antenna arrays will increase the systems complexity and corresponding cost.

Initially, the estimation of AOA mainly used subspace based methods[81, 82], which made the estimation very challenging under severe multipath propagation. More recently, sophisticated AOA estimation techniques appropriate for multipath environments have been developed [83, 84].

The current trend is to combine the previous techniques such as a fusion of TOA (TDOA) and AOA data to achieve more accurate localization is the current trend. Such hybrid systems attempt to capitalize on the advantages of both time-based and angle-based positioning techniques. Recently, hybrid systems that combine TOA and AOA estimation or TDOA and AOA estimation have received considerable attention for UWB location estimation. In [85], a hybrid TDOA/AOA is developed for indoor UWB scenarios using extended Kalman filters. A TOA/TDOA hybrid relative positioning system is presented in [86], with reduced receiver number and communication times in a positioning sequence. In [106] the CRB is derived for hybrid TDOA/AOA systems, using both non modulated and modulated IR-UWB waveforms.

2.4 Review of selected parameter estimation techniques for single-user

In this section we provide a more detailed summary of parameter estimation estimation techniques from the pertinent literature.

2.4.1 Single antenna TOA estimation

Energy detection based methods

Low power, low complexity TOA estimators using Energy Detection (ED) have been well developed and researched in recent years. In a typical ED receiver, shown in Fig. 2.7, the received

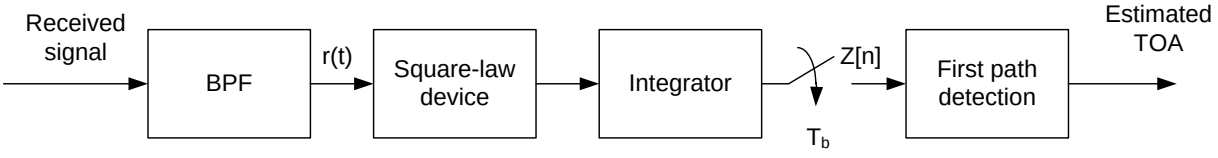

Fig. 2.7 Energy detection

signal is first passed through a Bandpass Filter (BPF), to eliminate out-of-band noise, followed by a square law device. Then, a time integrator collects the signal energy within a chosen time

window called a block. The integrator's output for the nth block is given by

$$z[n] = \int_{(n-1)T_b}^{nT_b} |r(t)|^2 dt \tag{2.15}$$

where $r(t)$ is the output of the BPF and T_b is the adjustable integration length (block length). Finally, timing estimation is performed by detecting the delay of the first path.

In the last step, several estimation methods can be used. The most common ones are Threshold Crossing (TC), Maximum Energy Select (MES), and MES-Search-Back (MES-SB) [87]. In the TC method, $z[n]$ is compared with a given threshold, say λ, to detect the presence of a signal. Specifically, the TOA is determined by the index of the first energy block exceeding the threshold, i.e., $\hat{\tau}_{TC} = \hat{n}_{TC} T_b$ where

$$\hat{n}_{TC} = \min\{n \,|\, 1 \leq n \leq N_u \text{ and } z[n] > \lambda\} \tag{2.16}$$

with N_u denoting the total number of samples in the TOA uncertainty region. The TC method is perhaps the simplest first path detection technique and often serves as a building block for more sophisticated TOA estimation techniques including the ones proposed in this thesis. Not surprisingly, its performance strongly depends on the choice of λ. On one hand, if λ is too small, there is a high probability of early (prior to the true TOA) detection of the first path. One the other hand, if λ is too large, there is a high probability of missing the actual first path and detecting, instead, an erroneous later path. In [32, 23], criteria for choosing the threshold are stated; many improved versions have also been proposed, see, e.g., [88, 89].

In MES method, the TOA estimate is simply determined by the index of the strongest energy block, i.e.,

$$\hat{n}_{MES} = \arg \max_{1 \leq n \leq N_u} \{z[n]\} \tag{2.17}$$

However, it is quite possible that in multipath conditions, the true TOA may not correspond to the first energy block exceeding the threshold nor to the energy block with the highest energy. The MSE-SB attempts to avoid these situations by combining the previous two methods. First, it finds the maximum energy block, and then searches backwards for several blocks until it reaches one that exceeds the threshold λ. The index of that block determines the TOA estimate.

Sub-Nyquist ML methods

Due to the impractical sampling rates of the exact ML estimators, ML estimators based on sub-Nyquist sampling models such as MESS, W-MESS, and DW-MESS have been proposed [26]. These estimators have the same structure as the ED based estimators, shown in Fig. 2.7; it is common, however, to replace the square law device and the integrator blocks with a filter matched to a locally stored reference pulse. In the following we describe these methods in more detail.

a) MESS: This method is similar to MES but considers the combined energy of samples in a sliding window instead of the energy of an individual sample. Denoting the window duration as N_w, the TOA is obtained as

$$\hat{n}_{MESS} = \arg \max_{1 \le n \le N_u} \{ \sum_{k=0}^{N_w-1} z[n+k] \} \tag{2.18}$$

Clearly, when $N_w = 1$, MESS reduces to MES.

b) W-MESS: When *a priori* knowledge about the channel is available in the form of its APDP, the MESS technique can be extended to incorporate this knowledge through a weighting procedure. The resulting method, called W-MESS, obtains the TOA as

$$\hat{n}_{W-MESS} = \arg \max_{1 \le n \le N_u} \{ \sum_{k=0}^{N_w-1} P[k] z[n+k] \} \tag{2.19}$$

where $P[k]$ is the sampled version of APDP. In many cases, APDP can be simply approximated by a single exponential. Alternatively, if the channel path energies are perfectly known, the APDP can also be replaced by the exact values of the path energies.

c) DW-MESS: This method is similar to W-MESS but the sample energies are further weighted by estimates of the mean and variance of their noise components. It is expected that at the true TOA, the mean μ_n and the standard deviation σ_n of the noise component are minimized. Therefore, using their inverses as a weighting factor will improve the likelihood of detecting the correct TOA. The resulting improved TOA estimator, DW-MESS, is given by

$$\hat{n}_{DW-MESS} = \arg \max_{0 < n < N_u} \{ \sum_{k=0}^{N_w-1} \frac{P[k] z[n+k]}{\mu_n \sigma_n} \} \tag{2.20}$$

The last two methods, W-MESS and DW-MESS require *a priori* information about the channel. However, such prior information may not be available in practice and should be accurately

estimated beforehand.

2.4.2 Cramer Rao Bound

The CRB provides a lower bound on the Mean-Squared-Error (MSE) of any unbiased estimator and, therefore, represents the theoretical limit of TOA estimation. ML estimators, such as the one developed in [21] for the UWB TOA estimation problem, can achieve this bound at high SNR. It was shown in [21] that the CRB for TOA estimation of the first path, is given by

$$CRB_{TOA} = \frac{\sigma^2}{N_{sym} E_b (\gamma_1 - \gamma_2^2) \alpha_{0,0}^2} \tag{2.21}$$

where N_{sym} is number of transmitted symbols[2], E_b is symbol energy, $\alpha_{0,0}$ is amplitude of the first path, σ^2 is the power spectral density of the white Gaussian noise, and finally

$$\gamma_1 = \frac{\int_0^{T_p} \left(\frac{dw(t)}{dt}\right)^2 dt}{\int_0^{T_p} w^2(t) dt} \quad \text{and} \quad \gamma_2 = \frac{\int_0^{T_p} \frac{dw(t)}{dt} w(t) dt}{\int_0^{T_p} w^2(t) dt} \tag{2.22}$$

are constants related to the specific pulse shape employed. It is clear that the CRB depends on the pulse shape, the path gains, and the SNR E_b/σ^2 and, as expected, the more symbols employed in the estimation, the lower the CRB is.

2.4.3 Joint TOA/AOA estimation

Joint parameter estimation has attracted increased attention in recent years. In this section, we review the work in [50], which will later be used as a benchmark in our own developed scheme.

As discussed earlier, AOA estimations methods require use of an antenna array, say with Q antenna elements, at each of the tag readers. The receiver chain at the qth antenna, $q \in \{0, \ldots, Q-1\}$, includes a BPF, followed by a square law device and, finally, a Low Pass Filter (LPF). The LPF output is averaged over several symbols in order to decrease the noise power; the resulting signals $z_q(t)$ are used to jointly estimate the TOA and AOA[3]. Let τ_q denote the TOA of the first path at the qth ($q = 0, \ldots, Q-1$) antenna and $\Delta\tau$ denote the TDOA of the first path

[2] In practice, the energy of the BPF output is averaged over N_{sym} symbols to minimize the effect of the additive noise.

[3] For simplicity in presentation, we use a continuous time formulation. In practice, the antenna outputs are sampled at the Nyquist rate and the algorithm operates in discrete time.

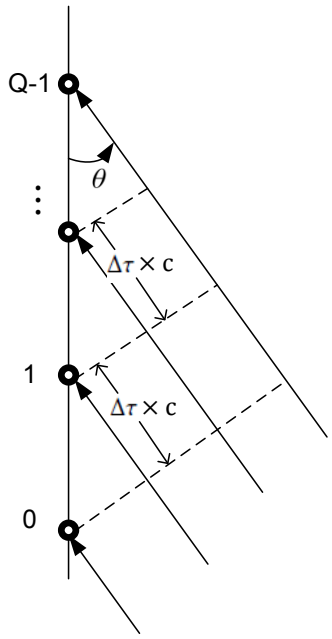

Fig. 2.8 Array geometry

between two adjacent antennas due to their spatial separation. Assuming a ULA with antenna 0 serving as the reference antenna illustrated in Fig. 2.8, we have the following relation between τ_q's and $\Delta\tau$:

$$\tau_q = \tau_0 + q\Delta\tau. \tag{2.23}$$

The joint estimation process of τ_0 and $\Delta\tau$ consists of 3 main steps. The first step obtains a rough estimate of τ_q at the qth antenna. The second step estimates $\Delta\tau$ and improves the estimate of τ_0 using the previously obtained rough estimates of $\hat{\tau}_q$. The third and last step obtains a fine estimate of the TDOA $\Delta\tau$ from which the final estimate on the AOA θ is obtained. The steps are described in more detail next.

a) Estimation of τ_q: At each antenna, a rough estimate, $\tilde{\tau}_q$, of the TOA τ_q is obtained using the TC method described in Section 2.4.1. The threshold λ is chosen such that the probability of early detection is in the order of 10^{-7}.

b) Estimation of $\Delta\tau$ and improved estimation of τ_0: The following linear model of the rough

estimates $\tilde{\tau}_n$ obtained in the previous step is assumed:

$$\tilde{\tau}_q = \tau_q + b + \epsilon_q \tag{2.24}$$

where b denotes a bias term and ϵ_q are independent, zero-mean random variables. Using this model, the LS estimates of τ_0 and $\Delta\tau$ can be obtained as:

$$\hat{\tau}_0 = \frac{2}{Q(Q+1)} \sum_{q=0}^{Q-1} [(2Q-1) - 3q]\tilde{\tau}_q \tag{2.25}$$

and

$$\Delta\tilde{\tau} = \frac{12}{Q(Q^2-1)} \sum_{q=0}^{Q-1} (q - \frac{Q-1}{2})\tilde{\tau}_q \tag{2.26}$$

c) Improved estimation of $\Delta\tau$: Assuming that $\hat{\tau}_0$ is a good approximation of the actual TOA τ_0, the averaged ED signal at the qth antenna can be decomposed into a sum of three terms:

$$z_q(t) = g(t - \hat{\tau}_0 - q\Delta\tau) + g'(t) + \bar{n}_q \tag{2.27}$$

where $g(t - \hat{\tau}_0 - n\Delta\tau)$ denotes the signal due to the first path, $g'(t)$ the contribution of paths arriving after the first path, and $\bar{n}_q$ is the noise contribution after averaging over K symbols with mean σ^2/K.

Under the assumption that the first two signal terms in (2.27) are well separated in time, the signal $y_q(t) = z_q(t) - \sigma^2/K$ is given by

$$y_q(t) = g(t - \hat{\tau}_0 - q\Delta\tau) + \bar{n}_q - \sigma^2/K \tag{2.28}$$

for values of t around $\tau_0 + q\Delta\tau$. Therefore, if $\Delta\tau$ were known, shifting $y_q(t)$ leftward by $\hat{\tau}_0 + q\Delta\tau$ would yield $g(t)$ plus noise. Because of this, in the summation

$$y(t; \hat{\tau}_0, \Delta\tau) = \frac{1}{Q} \sum_{q=0}^{Q-1} y_q(t + \hat{\tau}_0 + q\Delta\tau) \tag{2.29}$$

the first path signals of all antennas would add coherently to form $g(t)$, meanwhile the noise part would add incoherently and thus reduce the overall level of noise. Based on this observation and under the additional assumption that most of the pulse energy is concentrated in a interval of

length W_g starting at time t_g, the final estimate of $\Delta\tau$ is obtained as

$$\Delta\hat{\tau} = \arg \max_{\delta \in (\Delta\tilde{\tau}-\epsilon, \Delta\tilde{\tau}+\epsilon)} \int_{t_g}^{t_g+W_g} y^2(t; \hat{\tau}_0, \delta) dt \tag{2.30}$$

where $\Delta\tilde{\tau}$ is the estimate of $\Delta\tau$ obtained in the previous step, and ϵ is the maximum expected absolute error $|\Delta\tilde{\tau} - \Delta\tau|$). Estimates of t_g, W_g and ϵ can all be computed beforehand through the analysis of the pulse shape employed. Finally, the fine estimate $\Delta\hat{\tau}$ is transformed into the corresponding AOA estimate.

2.5 Concluding statements

In this chapter, we presented a review of some important concepts for parameter estimation in IR-UWB systems, including a brief discussion of pulse signaling, the IEEE 802.15.4a UWB channel model, current position estimation techniques and selected parameter estimation methods. These notions will serve as background material for the coming chapters in which we focus on new parameter estimation algorithms for TOA/AOA, which will be later used to develop corresponding hybrid positioning schemes.

Chapter 3

Estimation of TOA and APDP in Single-Antenna IR-UWB Systems

In this chapter[1], we consider the problem of TOA estimation for a single active user in single-antenna IR-UWB systems. Instead of assuming a known APDP, a parametric model with multiple exponentially decaying clusters is assumed for the APDP and its parameters are estimated along with the unknown TOA. A preliminary motivational discussion for this approach is provided in Section 3.1 and the corresponding system model is explained in Section 3.2. The proposed method for joint TOA and APDP estimation, which relies on a combination of ML and LS techniques, is presented in detail in Section 3.3. In Section 3.4, the CRB for joint estimation of these parameters is derived. Performance comparisons of the proposed method to other benchmark approaches are presented and discussed in Section 3.5. Finally, in Section 3.6, a short conclusion is given.

3.1 Motivation

Sub-Nyquist ML-based TOA estimators, e.g., [25, 26], currently assume some prior knowledge of the UWB channels in the form of the APDP, as explained in previous chapters. As we have been able to verify, a lack of adequate information about the APDP can significantly deteriorate their performance. Therefore, for these estimators to function properly, the APDP of UWB channels should be estimated beforehand. We note that in addition to its application in TOA estimation, the

[1]Parts of Chapter 3 have been presented at the 2012 International Conference on Communications [90] and in Signal Processing [91].

APDP is an important characteristic of the UWB channel in its own right. Indeed, it can provide useful information about the characteristics of the multipath radio channel, including the presence of dominant scatterers in the vicinity of the RFID transmitter as well as the reflection/absorption properties of the surrounding environment. Despite its importance, the estimation of the APDP from a statistical signal processing perspective has not yet been extensively explored. Intrigued by this, instead of assuming a known APDP of the UWB channel, we investigate the estimation of the APDP along with the desired TOA at sub-Nyquist sampling rate. To this end, and motivated by the work of the IEEE 802.15.4a Task Group on standard channel models for IR-UWB systems [6], we adopt a multiple cluster parametric model for the APDP. The parameters of this model include the clusters' arrival times, peak power levels and decay rates which, together with the unknown TOA, define the unknown parameter vector subject to estimation. Based on this model, we can derive the likelihood function of the observed data for the complete set of unknown parameters. Since a multi-dimensional exhaustive search for the ML estimates would be too complicated and therefore impractical, a sub-optimal scheme in which the APDP parameters are first estimated via a least-squares approach is considered. The resulting APDP is then used to find the TOA estimate via the ML criterion through a 1-dimensional (1D) search at the chip level (sub-Nyquist). We also derive the CRB for joint unbiased estimators of the APDP and TOA parameters. Through numerical simulations of IR-UWB signal propagation in realistic multipath UWB channels, the proposed joint estimator is shown to produce accurate estimates of the TOA and the APDP parameters. The newly obtained APDP estimate can also be used in other existing sub-Nyquist estimators which need this information beforehand. Using the same chip sampling rate at the receiver, we show that the proposed joint TOA estimator outperforms the previous ones as it can achieve a finer accuracy in practical UWB TOA estimation scenarios. The proposed method has reasonable complexity and is well-suited for real-time implementation.

3.2 System model

We consider a RFID-based location system in which the tag transmits a time-hopping (TH) IR-UWB signal $s(t)$. TOA estimation is typically performed during the preamble section of a ranging packet. As described by the IEEE 802.15.4a standard, the preamble can contain a large number of symbols (e.g., up to 4096) [92]. To improve processing gain and suppress noise, averaging over the preamble symbols is a very common operation [93, 23]. The signal $s(t)$ consists of N_f consecutive frames of duration T_f, that amount to a total observation interval $T_o = N_f T_f$. In turn,

each frame is divided into N_c consecutive chips of equal duration T_c, so that $T_f = N_c T_c$. Within the jth frame, $j = 0, 1, \ldots, N_f - 1$, a single IR-UWB pulse $w(t)$ is transmitted with a time offset of $c_j T_c$ relative to the beginning of the frame, where $c_j \in \{0, \ldots, N_c - 1\}$ denotes the TH sequence. We assume that the UWB pulse waveform $w(t)$ has finite duration T_c, i.e., $w(t) = 0$ for $t \leq 0$ and for $t \geq T_c$. In addition, the pulse transmitted within the jth frame is affected by a polarity code, $d_j \in \{+1, -1\}$, used for spectrum smoothing [94]. A data aided approach is employed in this work in which a known training sequence (i.e., all zero) is used, which is very common in this application, e.g., [95, 96].

Accordingly, the transmitted signal can be expressed in mathematical form as

$$s(t) = \sum_{j=0}^{N_f-1} d_j \sqrt{E_p}\, w(t - jT_f - c_j T_c), \quad 0 \leq t \leq T_o \tag{3.1}$$

where $E_p > 0$ will denote the transmitted energy per pulse. In practice, both sequences c_j and d_j are known to the receiver. In this thesis, since we consider the single user case, no TH code will be used; without loss in generality, we therefore set $c_j = 0, \forall j$.

The transmitted UWB signal $s(t)$ propagates over a multipath channel before reaching the tag reader. A tapped delay line model is employed to characterize the UWB multipath channel, as in [34, 97, 98]. Assuming a tap spacing of T_c, this model represents the impulse response $h(t)$ of the channel as the sum of scaled and delayed impulses:[2]

$$h(t) = \sum_{l=0}^{L-1} a_l \delta(t - \tau_l) \tag{3.2}$$

where $\delta(\cdot)$ is the Dirac delta function, a_l is a zero-mean random variable representing the amplitude of the lth multipath component, $\tau_l = lT_c + \tau_0$ is the propagation time delay of the lth multipath, $\tau_0 > 0$ is the deterministic but unknown delay of the first path, and L is the number of time resolvable multipaths. According to (3.2), the channel delay spread is given by $\tau_{ds} = LT_c$. Here, the focus is on sub-Nyquist TOA resolution and hence we assume that τ_o is a multiple of the chip duration, i.e., $\tau_0 = DT_c$ where D is an integer [34]. This approach reduces the search complexity of the delay estimation; yet, as will be illustrated in Section 3.5, our proposed algorithm can be applied with arbitrary values of τ_0.

[2]The pulse distortion on each multipath component, due to the fine (time unresolvable) structure of the channel, is ignored for simplicity.

Since the above tapped delay line model is based on the use of resolvable time delay bins, the temporal correlation coefficients between adjacent tap amplitudes are very small and can be neglected according to previous studies [66, 99, 27]. Therefore, the channel tap vector, defined as $\boldsymbol{h} = [a_0, ..., a_{L-1}]^T$, has zero mean and covariance matrix

$$\boldsymbol{R}_h = E[\boldsymbol{h}\boldsymbol{h}^T] = \begin{bmatrix} P_0 & 0 & \dots & 0 \\ 0 & P_1 & & \vdots \\ \vdots & & \ddots & 0 \\ 0 & \dots & 0 & P_{L-1} \end{bmatrix} \tag{3.3}$$

where the sequence of the diagonal entries, $P_l = E[a_l^2]$, for $l = 0, \dots, L-1$, constitutes the APDP of the channel.

The UWB channel model proposed by the IEEE 802.15.4a task group is based on the modified Saleh-Valenzuela model [6], according to which each channel tap amplitude a_l follows a Nakagami distribution, and the APDP conforms to a doubly-exponential decay model with Poisson inter-arrival time. For mathematical convenience, we consider a simplified version of this model in which the amplitudes of the resolvable multipaths in (3.2) follow a Gaussian distribution, with the associated APDP expressed as a sum of multiple, exponentially decaying clusters, as follows (see also Fig. 3.1):

$$P_l = \sum_{k=0}^{C-1} \beta_k e^{-\alpha_k (l - c_k)} u(l - c_k), \quad l = 0, ...L-1 \tag{3.4}$$

where C is the total number of clusters, $k \in \{0, \dots, C-1\}$ is the cluster index, the non-negative parameters β_k, α_k and c_k represent the peak power level, exponential decay rate and start time (i.e., arrival time of the first path) of the kth cluster, respectively, and $u(l)$ denotes the unit step function (i.e., $u(l) = 1$ for $l \geq 0$ and 0 otherwise). We note that c_k represents the arrival delay of the first path within the kth cluster, relative to the first arrival delay D. Therefore $c_0 = 0$ and $c_k < c_{k+1}$.

The parameters of this APDP model, depend on the characteristics of the UWB radio propagation environment. We emphasize that the above modeling simplifications are made purely for the sake of developing a mathematically tractable algorithm; in our simulation experiments in Section 3.5, the resulting algorithm will be shown to perform adequately when applied to more accurate UWB channel models that comply with the IEEE 802.15.4a standard.

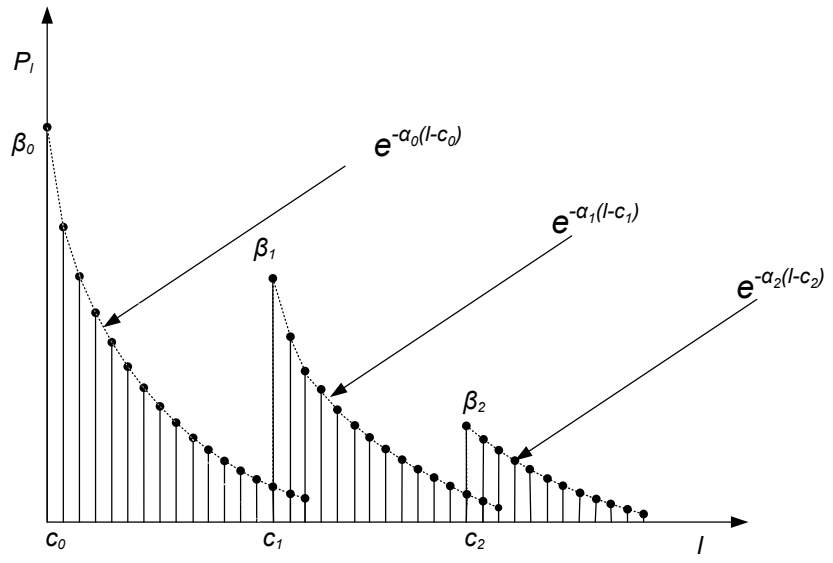

Fig. 3.1 APDP in Saleh-Valenzuela model.

After multipath propagation, the received UWB signal at the tag reader can be expressed as

$$r(t) = \sum_{l=0}^{L-1} a_l s(t - \tau_l) + n(t), \quad 0 \le t \le T_o \tag{3.5}$$

where $n(t)$ is an additive noise term modeled as a white gaussian process with PSD level $\sigma_n^2 = N_0/2$. We assume that T_f is sufficiently large such that there is no Inter-Frame Interference (IFI), that is: the scaled and delayed replicas of the transmitted pulse during the jth frame are received during that frame, which is possible if $0 \le \tau_0 \le \tau_{max}$ where the maximum delay satisfies $0 \le \tau_{max} \le T_f - \tau_{ds}$. In practice, the transmitted pulse signal has a low duty cycle, of the order of 1Mbits/s or less, while the delay spread of a typical indoor channel is of the order of a few 100ns or less. Hence, this assumption is well justified. Nevertheless, the effect of a small amount of IFI is further considered in our simulation experiments (see Section 5). Under this assumption, it follows from (3.1) and (3.5) that

$$r(jT_f + t) = d_j \sqrt{E_p} \sum_{l=0}^{L-1} a_l w(t - \tau_l) + n(jT_f + t), \quad 0 \le t < T_f. \tag{3.6}$$

To derive the TOA estimator, an equivalent discrete-time version of the above signal model will be used. We first consider uniform sampling at the rate $1/T_s$, where $T_s \leq 1/2B$ and B is the bandwidth of the transmitted IR signal. Let $M = T_c/T_s$ be an integer, so that each frame is represented by MN_c samples and let $\boldsymbol{r}_j = [r(jT_f), \ldots, r(jT_f + (MN_c - 1)T_s)]^T$ denote the column vector of discrete-time noisy signal samples of the jth frame. Similarly, the IR pulse $w(t)$ can be represented by the column vector $\boldsymbol{w} = [w(0), ..., w((M-1)T_s)]^T$ and we let $\boldsymbol{w}$ have unit energy. We emphasize that the sampling period T_s mentioned here is used only to analyze the discrete-time system model; in the end, the proposed estimator will only require the evaluation of the likelihood function at the sub-Nyquist chip rate of $1/T_c$ (see Section 3.3).

Making use of (3.6), the vector of received signal samples $\boldsymbol{r}_j$ in the jth frame can be written as

$$\boldsymbol{r}_j = d_j \sqrt{E_p} \boldsymbol{W} \boldsymbol{h} + \boldsymbol{n}_j \tag{3.7}$$

where $\boldsymbol{W} = [\boldsymbol{w}_D, \boldsymbol{w}_{D+1}, \ldots, \boldsymbol{w}_{D+L-1}]$ is a $MN_c \times L$ matrix with columns

$$\boldsymbol{w}_d = [\underbrace{0, \ldots, 0}_{dM}, \boldsymbol{w}^T, \underbrace{0, \ldots, 0}_{MN_c - M - dM}]^T \tag{3.8}$$

for $d \in \{D, D+1, \ldots, D+L-1\}$, and $\boldsymbol{n}_j$ is the discrete-time vector representation of the zero mean Gaussian noise $n(t)$ in the jth frame.

Given the set of observations $\boldsymbol{r}_j$, for $j \in \{0, \ldots, N_f - 1\}$ and the knowledge that the UWB channel's APDP can be described as in model (3.4), our aim is to develop estimators for the unknown integer delay, D, and the modeling parameters of the APDP, that is, the number of clusters C, and the individual clusters' parameters α_k, β_k and c_k for $k \in \{0, \ldots, C-1\}$. In the absence of IFI, D is limited to the range $0 \leq D \leq D_{max} = N_c - L$. The cluster parameters α_k, β_k are positive real numbers, and the associated shift parameters c_k are non-negative integers.

3.3 Joint estimator of APDP and TOA for single user case

In this section, we develop a novel approach for jointly estimating the unknown integer delay D and the parameters of the APDP. The block diagram of the proposed method is given in Fig. 3.2. We first derive the LLF for the joint estimation problem, based on the modeling assumptions previously discussed. To avoid the computational complexity of maximizing the likelihood function by searching over the complete parameter space, we propose a sub-optimal approach in which

the APDP parameters are estimated via least-squares fitting using the parametric model in (3.4). The APDP estimates so obtained are substituted back into the LLF, which is finally maximized to obtain the desired delay estimate D.

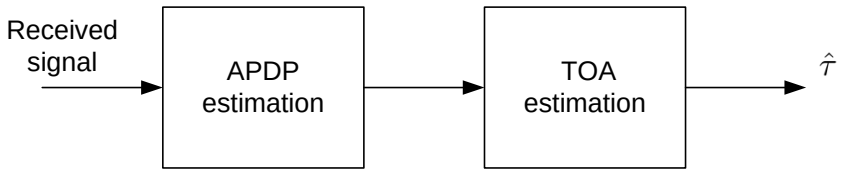

Fig. 3.2 Block diagram of proposed approach

3.3.1 Log-likelihood function derivation

Since the channel tap vector $\boldsymbol{h}$ and the additive noise vector $\boldsymbol{n}_j$ are independent Gaussian with zero-mean, it immediately follows from (3.7) that the vector of observations in the jth frame, $\boldsymbol{r}_j$, is also Gaussian with zero mean and covariance matrix

$$\boldsymbol{R}_{\boldsymbol{r}_j} = E[\boldsymbol{r}_j \boldsymbol{r}_j^T] = E_p \boldsymbol{W} \boldsymbol{R}_h \boldsymbol{W}^T + \sigma_n^2 \boldsymbol{I} \tag{3.9}$$

where $\boldsymbol{R}_h$ is given by (3.3). Note that in establishing the discrete form (3.9), we assume that the vector $\boldsymbol{w}$ has unit energy instead of $\int_0^{T_c} w^2(t)dt = 1$, and correspondingly, the covariance matrix $\sigma_n^2 \boldsymbol{I}$ is used instead of $2B\sigma_n^2 \boldsymbol{I}$. [3]

In addition, because of the white noise assumption, the covariance matrix between observation vectors in different frames is simply

$$\boldsymbol{R}_{\boldsymbol{r}_i \boldsymbol{r}_j} = E[\boldsymbol{r}_i \boldsymbol{r}_j^T] = d_i d_j E_p \boldsymbol{W} \boldsymbol{R}_h \boldsymbol{W}^T. \tag{3.10}$$

Therefore, the covariance matrix of the complete received signal vector within the observation time $T_o = N_f T_f$, represented by $\boldsymbol{r} = [\boldsymbol{r}_0^T, \ldots, \boldsymbol{r}_{N_f-1}^T]^T$, can be described as the following block matrix

$$\boldsymbol{R}_{\boldsymbol{r}} = E_p \boldsymbol{W}_r \boldsymbol{R}_h \boldsymbol{W}_r^T + \sigma_n^2 \boldsymbol{I} \tag{3.11}$$

where $\boldsymbol{W}_r = \boldsymbol{d} \otimes \boldsymbol{W}$, $\boldsymbol{d} = [d_0, \ldots, d_{N_f-1}]^T$ with size $N_f \times 1$, and $\otimes$ represents the Kronecker product. We note that there are $N_f \times N_f$ blocks in the first term on the right-hand side of (3.11)

[3] In this chapter, we use the symbol $\boldsymbol{I}$ invariably to denote an identity matrix of appropriate dimension.

and the identity matrix has dimension MN_cN_f.

Under the Gaussian assumption, the LLF of the received signal $\boldsymbol{r}$ can be written in the following form:

$$L(\boldsymbol{r};\boldsymbol{\theta}) = -\underbrace{\boldsymbol{r}^T\boldsymbol{R}_{\boldsymbol{r}}^{-1}\boldsymbol{r}}_{L_1} - \underbrace{\ln(\det(\boldsymbol{R}_{\boldsymbol{r}}))}_{L_2} \tag{3.12}$$

where $\boldsymbol{\theta} = (P_0, \ldots, P_{L-1}, D)$ is the vector of unknown parameters, consisting of the APDP values and the integer delay. The dependence of the LLF on $\boldsymbol{\theta}$ is through the covariance matrix, i.e., $\boldsymbol{R}_{\boldsymbol{r}} \equiv \boldsymbol{R}_{\boldsymbol{r}}(\boldsymbol{\theta})$ in (3.11).

After some manipulations, we find that the terms L_1 and L_2 in the right hand side of (3.12) are equal to

$$L_1 = -\frac{E_p}{\sigma_n^4}\boldsymbol{r}^T\boldsymbol{W}_r(\boldsymbol{R}_h^{-1} + \frac{E_pN_f}{\sigma_n^2}\boldsymbol{I})^{-1}\boldsymbol{W}_r^T\boldsymbol{r} + C_1 \tag{3.13}$$

and

$$L_2 = \sum_{l=0}^{L-1}\ln\det(\frac{E_pN_f}{\sigma_n^2}\boldsymbol{R}_h + \boldsymbol{I}) + C_2 \tag{3.14}$$

where C_1 and C_2 are constants independent of the unknown parameter vector $\boldsymbol{\theta}$. The inverse of $\boldsymbol{R}_{\boldsymbol{r}}$, which is needed in L_1, can be obtained with the help of the matrix inversion lemma [100].

In light of (3.13), it is convenient to define the $L \times 1$ vector $\boldsymbol{z} = \frac{1}{N_f}\boldsymbol{W}_r^T\boldsymbol{r}$, whose lth entry can be expressed as

$$z(l;D) = \frac{1}{N_f}\sum_{j=0}^{N_f-1} d_j\boldsymbol{w}_{D+l}^T\boldsymbol{r}_j \tag{3.15}$$

where the dependence on D is now made explicit. Note that, on the basis of (3.8), the inner product $\boldsymbol{w}_l^T\boldsymbol{r}_j$ represents the lth output (at the chip rate) of a filter matched to the transmitted pulse $w(t)$, when applied to the observed data in the jth frame. Accordingly, the vector $\boldsymbol{z}$ contains delayed values (by D) of the matched filter output, further averaged over the N_f available frames.

Making use of (3.15) and (3.3) in (3.13) and after further simplifications, the final expression of the LLF can be obtained as

$$L(\boldsymbol{r};\boldsymbol{\theta}) = \sum_{l=0}^{L-1}\Big[\frac{\mathrm{SNR}_l}{(1+\mathrm{SNR}_l)}\frac{z^2(l;D)N_f}{\sigma_n^2} - \ln(1+\mathrm{SNR}_l)\Big] \tag{3.16}$$

where we define

$$\mathrm{SNR}_l = \frac{N_fE_pP_l}{\sigma_n^2}, \quad l = 0, 1, \ldots, L-1. \tag{3.17}$$

The latter gives the SNR for the lth propagation path and is a function of the unknown parameter P_l.

The joint ML estimator of the integer delay D and the APDP values P_l, $l = 0, \ldots, L-1$, can be obtained by maximizing the log-likelihood function with respect to these parameters. Unfortunately, the large dimension (i.e., $L+1$) of the resulting parameter vector $\boldsymbol{\theta}$ prohibits a practical implementation of this search. In the next section, we develop a simplified scheme based on a lower-dimensional parametric model of the APDP.

3.3.2 Estimation of average power delay profile

If the APDP were known, one could estimate the TOA via a simple one-dimensional search of the LLF in (3.16) over the discrete delay parameter D. Motivated by this observation, we propose to first estimate the APDP and then substitute the results back in (3.16) for the final search. Ideally, as described in Section 2, the APDP of a UWB channel exhibits a double-exponential decay as a function of the excess delay parameter l, as given by (3.4). Here, we adopt a curve fitting approach based on a weighted LS rule to fit such a model to a function of the observed data. Because of the importance of the single cluster case ($C = 1$) in the literature and the resulting simplifications in the APDP estimation, we treat it separately from the multiple clusters ($C > 1$) case.

Single cluster fitting

Differentiating (3.12) with respect to P_l and setting the result to 0, we first obtain a preliminary APDP estimate conditioned on D as follows:

$$\hat{P}_l^{(0)}(D) = \max\{\frac{1}{E_p}[z(l;D)^2 - \sigma_n^2], \delta_0\}, \quad l = 0, \ldots, L-1 \tag{3.18}$$

where $z(l;D)$ is the time-shifted correlator output (3.15), δ_0 is a small positive number and the maximum operation is used to ensure that the estimate $\hat{P}_l^{(0)}(D) \geq \delta_0 > 0$ for all l.

For the single cluster model, we seek to fit the calculated $\hat{P}_l^{(0)}(D)$ in (3.18) to a simplified form of the APDP (3.4) with only a single exponentially decaying envelope, i.e., $P_l = \beta e^{-l\alpha}$ for $l = 0, \ldots, L-1$, with parameters $\alpha > 0$ and $\beta > 0$. Since an exponential decay in linear scale becomes a straight line in logarithmic scale, we choose to carry out the curve fitting in the log-domain and seek values of α and β that best fit $\ln \hat{P}_l^{(0)}(D)$ in a weighted LS sense. Specifically,

these parameters are obtained by solving the following optimization problem:

$$\min_{\alpha,\beta} \sum_{l=0}^{L-1} \mu_l \left| \ln \hat{P}_l^{(0)}(D) - (\ln\beta - l\alpha) \right|^2 \tag{3.19}$$

where $\mu_l \geq 0$ denotes a suitable weighting sequence. Our use of μ_l and our choice for its specific form have a simple intuitive justification. Ideally, we would like to include in the fitting only the data points that correspond to actual Multipath Components (MPCs). Also, due to the log operation, we find that paths with very low power would be overemphasized in the above objective function, which lead to poor fitting. Therefore, we propose to include in the fitting only the local maxima as they are more likely to correspond to MPCs, and discard the very low power values at the same time. Accordingly, we set $\mu_l = 1$ if there is a local maximum, i.e., $\hat{P}_{l-1}^{(0)}(D) < \hat{P}_l^{(0)}(D) > \hat{P}_{l+1}^{(0)}(D)$, and 0 otherwise. This approach, which has been confirmed experimentally, allows us to mask out the noisy low power data points, as desired.

The analytic solution to (3.19) is given by

$$\hat{\alpha} = -\frac{\sum_{l=0}^{L-1} \mu_l (l - A_1) \ln \hat{P}_l^{(0)}(D)}{A_0 A_1^2 - A_0 A_2} \tag{3.20}$$

$$\hat{\beta} = \exp\left(\frac{1}{A_0} \sum_{l=0}^{L-1} \mu_l \ln \hat{P}_l^{(0)}(D) + A_1 \hat{\alpha}\right) \tag{3.21}$$

where we define

$$A_0 = \sum_{l=0}^{L-1} \mu_l, \quad A_1 = \frac{1}{A_0} \sum_{l=0}^{L-1} l\mu_l, \quad A_2 = \frac{1}{A_0} \sum_{l=0}^{L-1} l^2 \mu_l. \tag{3.22}$$

Note that A_0 is the total number of local maxima, while A_1 and A_2 corresponds to the first and second moments of the weighting μ_l.

With the above values of $\hat{\alpha}$ and $\hat{\beta}$, a new APDP estimate is obtained as follows

$$\hat{P}_l^{(1)}(D) = \hat{\beta} e^{-l\hat{\alpha}}, \quad l = 0, \ldots, L-1. \tag{3.23}$$

This estimate can be easily calculated for every possible D in the range of $1, 2, \ldots, D_{max}$, and then substituted back in (3.16) to finalize the one-dimensional search over the delay parameter, as further discussed in section 3.3.1. Although single cluster fitting may lead to an oversimplified description of the overall APDP, its use in connection with the LLF (3.16) can still provide a

fine estimation of the unknown delay D. However, in cases where there are multiple separated clusters in the UWB channel, we find that the TOA performance can be improved by using a more sophisticated fitting approach that better reflects this situation.

Multiple clusters fitting

In this case, we would like to adjust the parameters in the complete model (3.4) to achieve the best fit with the available data obtained for a specific channel. Since a more complicated APDP model is adopted, it is desirable to estimate its parameters only once; that is, to reduce complexity, we will not seek to estimate a new $\hat{P}_l^{(1)}$ for every possible D. It turns out that for this purpose, only a rough estimate of D is needed, and this can be obtained by considering the complete set of instantaneous power values at the matched filter output, i.e., $\hat{P}_i^{(0)}(0)$, as given by (3.18) with $D = 0$ but with the range of the subscript i now extended over the entire frame, i.e., $i = 0, \ldots, N_c - 1$. To obtain the preliminary delay estimate of D, say $\hat{D}_p$, we use a method similar to the MESS in [26], with the main difference that a threshold is used to rule out impossible timing points. As a result, the search range for the delay is now much smaller, which greatly reduces the computational cost. Based on the estimate $\hat{D}_p$, we form the sequence $\hat{P}_l^{(0)}(\hat{D}_p)$ for $l = 0, \ldots, L - 1$ and use it to fit the parameters of the multiple cluster model in (3.4). To this end, we propose an iterative weighted LS approach, which searches for, and fits consecutive clusters one at a time, until a stopping criterion has been met.

A detailed description of the proposed algorithmic steps follows.[4]

Step 1: We fit the instantaneous log power data for the whole frame (i.e., $\ln \hat{P}_i^{(0)}(0)$, $i = 0, ..., N_c - 1$) to a straight line $l_{TH_1}(i) = \ln\beta - i\alpha$, which will be used as a basic threshold. In particular, the parameters α and β are obtained via a weighted LS fitting similar to (3.19), but where the range of summation is now from 0 to $N_c - 1$:

$$\arg\min_{\alpha,\beta} \sum_{i=0}^{N_c-1} \mu_i \left|\ln \hat{P}_i^{(0)}(0) - (\ln\beta - i\alpha)\right|^2 \tag{3.24}$$

where $\mu_i = 1$ if $\hat{P}_i^{(0)}(0)$ is a local maximum and 0 otherwise. The use of $l_{TH_1}(i)$ will greatly reduce the search range for the preliminary estimate of $\hat{D}_p$ in the next step.

Step 2: We identify the local maxima of $\ln \hat{P}_i^{(0)}(0)$ which are above the basic threshold line

[4] At this point, the reader may consult Fig. 3.3 for further clarifications on these steps; the experimental methodology for generating this figure will be explained in detail in Section 3.5.

$l_{TH_1}(i)$. Among these local maxima, we consider those in the range $0 \leq i \leq D_{max}$. For each of these points, we calculate the sum $\sum_{l=0}^{L-1} \ln \hat{P}_l^{(0)}(i)$. The value of i for which this sum is maximum is taken as the estimate $\hat{D}_p$. The latter also gives us the position of the first cluster in the frame, i.e., $c_0 = \hat{D}_p$.

Step 3: We fit the local maxima of $\ln \hat{P}_l^{(0)}(\hat{D}_p)$, $l = 0, \ldots, L-1$ to a new straight line, denoted by $l_{TH_2}(l)$, using the same procedure as in the single exponential case. This new threshold, obtained using the data of all the clusters, will be used to determine the onset of any new cluster, that is: the APDP value at the starting point of each cluster, given by parameter β_k, should be above $l_{TH_2}(l)$.

Step 4: We search for new clusters using $l_{TH_2}(l)$ as a threshold. Assuming that the starting time of the current cluster c_k is known, we detect a new cluster if we find at least one point $\hat{P}_l^{(0)}(\hat{D}_p)$ that is above $l_{TH_2}(l)$ in the range $c_k + \lfloor \tau_{mic}/T_c \rfloor \leq i \leq c_k + L$, where τ_{mic} is the minimum inter-cluster delay depending on the channel environment, e.g., $\tau_{mic} = 10$ns. We denote the corresponding abscissa l for these points as l_j, $j = 1, \ldots, J$, where J is the total number of such points.

Step 5: Once a new cluster is detected, we have to identify its starting time. Intuitively, l_1 could be considered as the new cluster starting time. However, this may not be the best choice due to noise and the random nature of the channel. Therefore, to select the starting time of the new cluster c_{k+1}, we proceed as follows. For each $j = 1, \ldots, J$, we temporarily set $c_{k+1} = l_j$ and perform a weighted LS fitting of the current exponential cluster between c_k and l_j according to

$$\arg\min_{\alpha_k, \beta_k} \frac{\sum_{i=c_k}^{l_j-1} \mu_i \left| \ln \hat{P}_i^{(0)}(0) - (\ln \beta_k - (i - c_k)\alpha_k) \right|^2}{\sum_{i=c_k}^{l_j-1} \mu_i}. \tag{3.25}$$

The value of l_j with the smallest average LS fitting error is chosen as the new cluster starting time, that is $c_{k+1} = l_j$, and the corresponding values of α_k and β_k are used as model parameters for the current cluster.

Step 6: We repeat Steps 4 and 5 until there are no new clusters detected and we let C denote the total number of detected clusters.

3.3.3 TOA Estimation

For the single cluster case, we let the estimated $\hat{P}_l^{(1)}(D)$ in (3.23) depend on the integer delay D. Since we simply assume one decaying exponential, it is simple to calculate this APDP estimate for every possible D. Note that α should be positive to ensure an exponential decay; therefore,

tentative delays D that lead to a negative value of α should be discarded. For every possible D in the search range, we substitute $\hat{P}_l^{(1)}(D)$ back into the LLF (3.16), and then search for the maximum over D, which is the only unknown parameter left to be estimated.

For the multiple clusters case, the APDP estimate $\hat{P}_l^{(1)}$ obtained from the above procedure bears no dependence on D. Inserting the refined APDP estimate $\hat{P}_l^{(1)}$ back into the LLF (3.16), again, the only unknown parameter left to be estimated is D, which can be finally obtained via a simple one-dimensional integer search. We note that once the APDP has been estimated, the final LLF $L(D)$ only depends on the matched filter outputs $z(l; D)$ and the background noise variance σ_n^2, which can be obtained from *a priori* estimation. We denote the final delay estimate by $\hat{D}$.

3.3.4 Complexity analysis

The computational complexity of our proposed approach mainly depends on two factors, namely, the preliminary LS-based APDP estimation and the subsequent TOA estimation which involves the maximization of the LLF.

For the sake of conciseness, our analysis of the APDP estimation complexity focuses on multiple cluster fitting as in Section 3.3.2. This approach begins in Step 1 with the LS fitting in (3.24) at a total cost of $4N_c$ flops. [5] The core of the procedure then relies on the application of multiple LS estimation steps, in which a set of power measurements, represented here by a vector $\boldsymbol{b}$ of generic length m, are fitted to a straight line in the log domain, represented by the product $\boldsymbol{A}\boldsymbol{x}$ where $\boldsymbol{A}$ is a known matrix of size $m \times 2$ and $\boldsymbol{x} = [\alpha, \ln\beta]^T$ is the vector of unknown parameters. The efficient implementation of the LS method then involves the QR factorization of matrix $\boldsymbol{A}$, with a cost of $8m$, followed by the computation of the unknown parameters with a cost of $4m$. Therefore, the total cost for each LS estimation step is $12m$, which is linear in m. In Step 1, we have $m < N_c$, while in Step 3, we have $m < L \leq N_c$. For Step 5, it is necessary to perform multiple LS fittings of various sizes. For simplicity, let us assume a constant value of J for each cluster index k. Because the cost of each LS fit is linear in m, it can be verified that the total cost of Step 5 is upper bounded by $12JL$. The total complexity of the multiple cluster APDP estimation algorithm is therefore upper bounded by $16N_c + 12(J + 1)L$ where J would typically be a small integer. Because we only use local maxima in the fitting, these bounds tend to be very conservative.

[5] The computational complexity is evaluated in terms of the number of required floating point operations (flop), where a multiply-add, a division and a numerical function evaluation (e.g. log) each count for 1 flop.

For each frame, we assume that the N_c squared correlator values, i.e., $z(l;0)^2$ for $l = 0, \ldots, L-1$, are available. For each $l \in \{0, \ldots, L-1\}$, we first compute the numerical coefficients $a_l = \mathrm{SNR}_l/(1 + \mathrm{SNR}_l)$, at the cost of $4L$. From there, each evaluation of the LLF (16) amounts to the calculation of an inner product. The total cost of the ML search is therefore of the order of LD_{max}, where D_{max} delimits the range for the TOA search. This cost for the evaluation and maximization of the LLF is comparable to that of competing sub-Nyquist estimators which, when implemented at the same sampling rate, require the evaluation of an inner product with similar size for each tentative value of the unknown delay [26],[27].

In practice, we find that the search range $D_{max} \geq 12J$, so that the total computational cost is dominated by the ML search for the TOA estimation, with the APDP estimation representing only a small fraction.

3.4 Cramer Rao Bound

The CRB provides a lower bound on the covariance matrix of any unbiased point estimator of a parameter vector. Specifically, if $\hat{\boldsymbol{\theta}}(\boldsymbol{r})$ denotes such an estimator of vector $\boldsymbol{\theta} = [\theta_1, \ldots, \theta_{L+1}]$ as a function of the observation vector $\boldsymbol{r}$, we have that

$$\mathrm{Cov}(\hat{\boldsymbol{\theta}}(\boldsymbol{r})) \geq \boldsymbol{J}(\boldsymbol{\theta})^{-1} \tag{3.26}$$

where $\mathrm{Cov}(\cdot)$ denotes the covariance matrix of its matrix argument, and $\boldsymbol{J}(\boldsymbol{\theta})$ is the $(L+1)\times(L+1)$ Fisher Information Matrix (FIM). The latter is defined in terms of its entries

$$J_{i,j}(\boldsymbol{\theta}) = -E\left[\frac{\partial^2 L(\boldsymbol{r};\boldsymbol{\theta})}{\partial\theta_i \partial\theta_j}\right] \tag{3.27}$$

where the expectation is based on the data model with parameter vector $\boldsymbol{\theta}$. The CRB is of practical interest here since the ML estimator can achieve this bound asymptotically under certain limiting conditions [22]. In this section, we derive the CRB for the joint estimation of the TOA and APDP, as represented by the unknown parameter vector $\boldsymbol{\theta}$.

To simplify the derivations, and especially manipulations involving differentiation with respect to time, we begin by introducing an equivalent integral representation for the discrete sam-

ple values at the matched filter output. That is, we let

$$z(l;D) \approx \frac{1}{N_f T_s} \int_0^{T_o} r(t)\xi(t-(l+D)T_c)dt \tag{3.28}$$

where the template signal $\xi(t)$ is defined by

$$\xi(t) = \sum_{j=0}^{N_f-1} d_j w(t - jT_f). \tag{3.29}$$

This approximation is well justified for small values of T_s, i.e., $T_s \leq 1/2B$ as previously assumed.

We differentiate (3.16) with respect to P_l and D, to obtain

$$\frac{\partial L(\boldsymbol{r};\boldsymbol{\theta})}{\partial P_l} = \frac{\partial L(\boldsymbol{r};\boldsymbol{\theta})}{\partial \mathrm{SNR}_l}\frac{\partial \mathrm{SNR}_l}{\partial P_l}$$

$$= \frac{E_p N_f}{\sigma_n^2(1+\mathrm{SNR}_l)}\Big[\frac{z^2(l;D)N_f}{\sigma_n^2(1+\mathrm{SNR}_l)} - 1\Big] \tag{3.30}$$

and

$$\frac{\partial L(\boldsymbol{r};\boldsymbol{\theta})}{\partial D} = \frac{2N_f}{\sigma_n^2}\sum_{l=0}^{L-1}\frac{\mathrm{SNR}_l}{1+\mathrm{SNR}_l} z(l;D)z'(l;D) \tag{3.31}$$

where we define

$$z'(l;D) = \frac{\partial z(l;D)}{\partial D} = -\frac{M}{N_f}\int_0^{T_0} r(t)\xi'(t-(l+D)T_c)dt \tag{3.32}$$

and

$$\xi'(t) = \frac{d\xi(t)}{dt}. \tag{3.33}$$

Based on (3.30) and (3.31), we can further obtain the required second order derivatives:

$$-E\Big[\frac{\partial^2 L(\boldsymbol{r};\boldsymbol{\theta})}{\partial P_{l_1}\partial P_{l_2}}\Big] = 0, \quad \forall\, l_1 \neq l_2 \tag{3.34}$$

$$-E\Big[\frac{\partial^2 L(\boldsymbol{r};\boldsymbol{\theta})}{\partial P_l^2}\Big] = \frac{E_p^2}{(E_p P_l + \sigma_n^2/N_f)^2}\Big(\frac{2E[z(l;D)^2]}{E_p P_l + \sigma_n^2/N_f} - 1\Big) \tag{3.35}$$

$$-E\Big[\frac{\partial^2 L(\boldsymbol{r};\boldsymbol{\theta})}{\partial P_l \partial D}\Big] = -\frac{2E_p N_f^2}{\sigma_n^4}\frac{E[z(l;D)z'(l;D)]}{(1+\mathrm{SNR}_l)^2} \tag{3.36}$$

and

$$E[\frac{\partial^2 L(\boldsymbol{r};\boldsymbol{\theta})}{\partial^2 D}] = -\frac{2N_f}{\sigma_n^2}\sum_{l=0}^{L-1}\frac{\mathrm{SNR}_l}{1+\mathrm{SNR}_l}\Big(E[z(l;D)z''(l;D)] + E[z'(l;D)^2]\Big). \tag{3.37}$$

Next, to calculate the above terms we need to evaluate the expected values $E[z(l;D)^2]$, $E[z(l;D)z'(l;D)]$ and $E[z(l;D)z''(l;D) + z'(l;D)^2]$ at the true value of D.

For the transmitted pulse, since $w(T_c) = w(0) = 0$ is the common case in practice, it comes naturally that

$$\int_0^{T_c}\frac{dw(t)}{dt}w(t)dt = \frac{1}{2}[w^2(T_c) - w^2(0)] = 0 \tag{3.38}$$

and therefore

$$\int_0^{T_c}\frac{d^2w(t)}{dt^2}w(t)dt = -\int_0^{T_c}(\frac{dw(t)}{dt})^2 dt. \tag{3.39}$$

After some manipulations using the above identities, the required expectations in (3.35)-(3.37) can be obtained as follows:

$$E[z(l;D)^2] = E_p P_l + \frac{\sigma_n^2}{N_f} \tag{3.40}$$

$$E[z(l;D)z'(l;D)] = 0 \tag{3.41}$$

and

$$E[z(l;D)z''(l;D) + z'(l;D)^2] = -\gamma E_p P_l T_c^2 \tag{3.42}$$

where the parameter

$$\gamma = \frac{\int_0^{T_c}(\frac{dw(t)}{dt})^2 dt}{\int_0^{T_c} w(t)^2 dt} \tag{3.43}$$

is positive and determined by the pulse shape.

Based on (3.36) and (3.41), it follows that

$$-E[\frac{\partial^2 L(\boldsymbol{r};\boldsymbol{\theta})}{\partial P_l \partial D}] = 0, \quad \forall l \tag{3.44}$$

Together with (3.34), this implies that the Fisher information matrix $\boldsymbol{J}(\boldsymbol{\theta})$ is diagonal. Using

(3.35), (3.37), (3.40) and (3.42), the diagonal entries of $\boldsymbol{J}(\boldsymbol{\theta})$ can be obtained as

$$J_{l,l} = -E[\frac{\partial^2 L(\boldsymbol{r};\boldsymbol{\theta})}{\partial^2 P_l}] = [\frac{E_p N_f}{\sigma_n^2(1+\mathrm{SNR}_l)}]^2, \quad l = 0,\ldots,L-1 \tag{3.45}$$

and

$$J_{L,L} = -E[\frac{\partial^2 L(\boldsymbol{r};\boldsymbol{\theta})}{\partial^2 D}] = \frac{2\gamma E_p N_f T_c^2}{\sigma_n^2}\sum_{l=0}^{L-1} P_l \frac{\mathrm{SNR}_l}{1+\mathrm{SNR}_l}. \tag{3.46}$$

Consequently, the CRBs are given by

$$\mathrm{Var}(\hat{P}_l) \geq J_{l,l}^{-1} = P_l^2\Big(1+\frac{1}{\mathrm{SNR}_l}\Big)^2 \tag{3.47}$$

$$\mathrm{Var}(\hat{D}) \geq J_{L,L}^{-1} = \frac{1}{2\gamma T_c^2}\Big(\sum_{l=0}^{L-1}\frac{\mathrm{SNR}_l^2}{1+\mathrm{SNR}_l}\Big)^{-1}. \tag{3.48}$$

From the above formulas, it is obvious that the CRBs depend on the SNR_l. When $\mathrm{SNR}_l \gg 1$, the above expressions for the CRB take simplified forms as follows:

$$\mathrm{Var}(\hat{P}_l) \geq J_{l,l}^{-1} \approx P_l^2 \tag{3.49}$$

and

$$\mathrm{Var}(\hat{D}) \geq J_{L,L}^{-1} \approx \frac{\sigma_n^2}{2(\sum_{l=0}^{L-1} P_l)\gamma E_p N_f T_c^2}. \tag{3.50}$$

Consequently, the CRB for the TOA estimate $\hat{\tau}$ becomes

$$\mathrm{Var}(\hat{\tau}) \geq \frac{\sigma_n^2}{(\sum_{l=0}^{L-1} P_l)2\gamma E_p N_f}. \tag{3.51}$$

We note from (3.49) that the standard deviation for the APDP at the lth tap is lower bounded by the corresponding power value, which is consistent with well-known results from the theory of smoothed power spectrum estimation [101]. Lower bounds on the estimation variance of the APDP parameters α_k and β_k can be obtained in turn by applying the chain rule for derivatives to (3.27) and making use of the results in (3.34) and (3.45). As for the CRB of the TOA in (3.51), it is inversely proportional to the total average power over the L taps, $\sum_{l=0}^{L-1} P_l$, the ratio of pulse energy-to-noise variance E_p/σ_n^2, the pulse shape factor γ in (3.43), and the number of frames N_f.

3.5 Numerical results

3.5.1 Methodology

In the simulations carried out here, the frame duration is set to $T_f = 200$ns; each frame is further divided into $N_c = 400$ chips of duration $T_c = 0.5$ns. Unless specified otherwise, the number of transmitted frames is set to $N_f = 60$. It is also assumed that each frame is equivalent to a single symbol. The transmitted UWB pulse $w(t)$ is a unit-energy Gaussian doublet [63] with duration T_c and effective bandwidth $B = 4$GHz. The energy per pulse E_p is given in terms of the SNR parameter E_p/σ_n^2. The synthesized pulse sequence is then filtered by a multi-path UWB channel.

The channel impulse responses used in our work are derived from the IEEE 802.15.4a typical channel models [6]. These impulse responses are randomly generated such that the multipath arrival times are grouped into multiple clusters, each cluster being characterized by an exponentially decaying average power envelope. Several such models have been developed to fairly represent channel conditions in different types of environments, such as residential, office, outdoor and industrial settings. The parameters of these models have been adjusted based on measurements over a representative range of frequencies and distances.

As mentioned in Section 3.3, the single cluster fitting method represents the overall fading of the channel versus delay by assuming a single exponentially decaying profile. Despite its simplified nature, this simple method is fairly robust and can be applied to all kinds of realistic channels. The multi-cluster fitting method seeks to further exploit finer details present in the APDP structure, i.e., by representing it in terms of multiple exponentially decaying components caused by the physical environment. When there is a clear multi-cluster structure in the channel, this method will indeed lead to better TOA estimation performance than the previous one. We note that the multi-clusters structure is very common for indoor UWB channels, as indicated by the measurement results in [18].

In our experiments, minor modifications were made to these IEEE channel models to allow for explicit control of the APDP parameters, i.e., number of clusters C, and for each cluster, shape parameters α_k, β_k, c_k. The results presented next focus on the CM3 channel model, which is representative of an indoor office environment; however, similar results and conclusions were obtained with other standard channels. The following parameter values were used: delay spread $\tau_{ds} = 120$ns, number of taps $L = 240$, and maximum delay $\tau_{max} = 80$ns. We note that the tap spacing of the created channel can be smaller than T_c, while our method still works fine with the assumption of T_c spaced taps.

Zero-mean white noise is added to the time domain samples at the UWB channel output. At the receiver side, the baseband antenna signal is passed through a (digital) filter matched to a local copy of the transmitted reference $s(t)$. The MF output is then sampled at the sub-Nyquist rate $1/T_c$ and the resulting samples are used in the ML estimator of τ and P_l as explained in Section 3. In addition, several TOA estimators from the recent literature are implemented and used as benchmarks.

The TOA estimation performance is evaluated in terms of the root mean square error (RMSE), defined as $\sqrt{E[(\hat{D}T_c - \tau_0)^2]}$ where $\hat{D}$ and τ_0 denote the estimated integer delay and the true value of the delay, respectively. In the Monte-Carlo simulations, the RMSE is approximated by averaging over 1000 independent channel trials, where in each trial a different value of τ_0 is selected randomly from the interval $(0, \tau_{max}]$. Note that here, τ_0 is arbitrary and not limited to being an integer multiple of T_c.

3.5.2 Results and discussion

The fitting in semi-logarithmic scale for several clusters is illustrated in Fig. 3.3 for a particular set of observed data with SNR = 30dB, as obtained with a CM3 channel displaying three identifiable clusters in its APDP structure. The longest straight line is the basic threshold $l_{TH_1}(i)$, which helps to select the first preliminary estimate $\hat{D}_p$ and the corresponding log values $\ln \hat{P}_l^{(0)}(\hat{D}_p)$, $l = 0, \ldots, L-1$. The second longest straight line represents the new threshold $l_{TH_2}(l)$, that is used in turn to detect the clusters. Finally, the $C = 3$ clusters detected in this example are fitted using the 3 shorter straight lines of varying slopes.

After getting all the needed parameters, i.e., C and the set of triplets $\{\alpha_k, \beta_k, c_k\}_{k=0}^{C-1}$, the final APDP estimate $\hat{P}_l^{(1)}$ can be calculated according to the general expression in (3.4). The newly estimated APDP $\hat{P}_l^{(1)}$ is plotted in linear scale in Fig. 3.4, along with the true APDP P_l based on the exact parameter values. It is seen that the proposed method provides a sufficiently accurate estimation of the true APDP. In this figure, we also show the result of single cluster estimation, showing that the single cluster method can be used to provide useful information about the rate of decay of the APDP even in this case.

To see whether multi-cluster fitting offers any performance advantages over single-cluster fitting, we compare the average fitting error and final TOA estimation performance as a function of the assumed number of clusters. For each experimental trial, we generate TOA estimates corresponding to different numbers of clusters, specifically: fixing $C = 1$, 2 and 3. For each

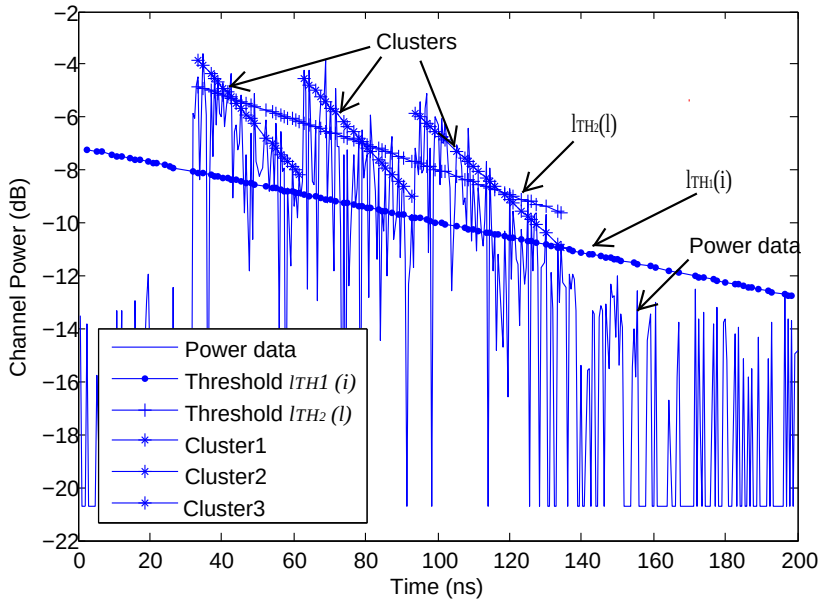

Fig. 3.3 Comparison of APDP fitting to raw power data in log scale (SNR = 30dB).

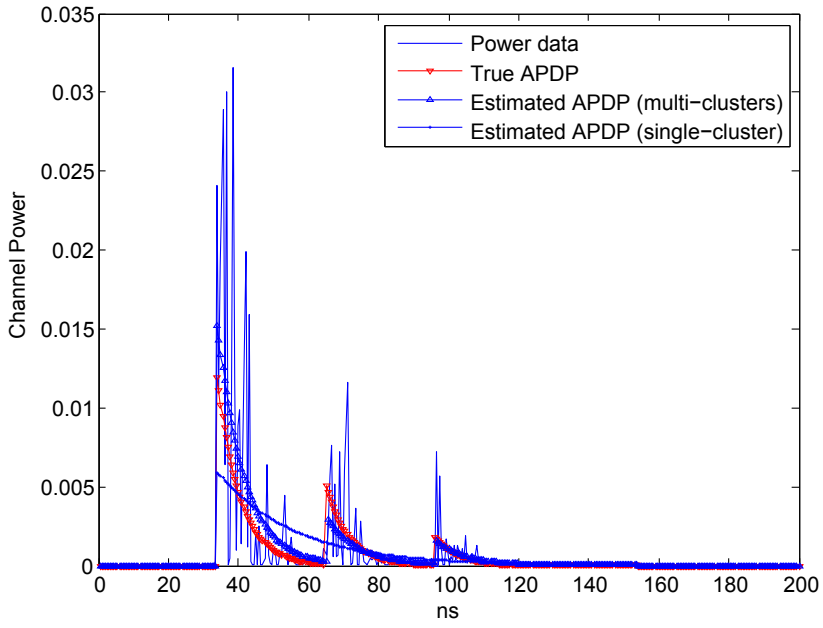

Fig. 3.4 Comparison of estimated and true APDP on a linear scale (SNR = 30dB).

of the considered cases, we show in Fig. 3.5 the average fitting error (defined by $\sum_{l=0}^{L-1} \mu_l |\hat{P}_l^{(0)} - \hat{P}_l^{(1)}|^2 / \sum_{l=0}^{L-1} \mu_l$) as a function of the SNR. It can be seen that multi-cluster fitting yields the lowest fitting error, followed by 2-cluster fitting and 1-cluster fitting.

In Fig. 3.6 we show the corresponding RMSE of TOA estimation. The same trend as in Fig. 3.5 is observed where it is seen that multi-cluster fitting also yields the best TOA estimation performance. It is remarkable that while the variations in the average fitting errors are relatively small, the gain in TOA performance can be quite significant, especially in the mid to high SNR range, i.e., between 15dB to 30dB, which is of great practical interest.

Fig. 3.7 shows the TOA estimation performance of the proposed multi-cluster fitting-based method as a function of the SNR for different values of the number of frames N_f. As expected, the TOA estimation accuracy improves as the number of frames increases, due to the averaging operation that reduces the effect of noise.

Next, we compare the proposed TOA estimator with the WMESS, DW-MESS [26] and ML with Partial channel information (MLP) [27] estimators. Since these methods require *a priori* knowledge of the APDP, we evaluate their performance with the true APDP (used to generate the CM3 channels) and with the estimated APDP obtained using the proposed multi-cluster method in Section 3.2. For a fair comparison, all the methods use the same sub-Nyquist sampling period of 0.5ns. The window length for the reference methods is set to 120ns, which is equal to the channel delay spread τ_{ds}. The other parameter values are the same as for the proposed method. Fig. 3.8 shows the performance of the 4 methods under consideration as a function of the SNR. We can see that the proposed method achieves a better accuracy than the previously proposed methods when the latter use the estimated APDP. Even when they use the true APDP, the proposed method outperforms WMESS and performs closely to the other two methods at high SNR.

We also investigate the behavior of the proposed approach under low levels of IFI. To this end, we consider an extended version of the CM5 channel model of total duration $\tau_{ds} = 280$ns, which now exceeds the frame duration $T_f = 200$ns. The tail portion of the response that extends over the next frame, consisting of the paths with delay in excess of 120ns, is linearly scaled so that its energy $\mathcal{E}_2$ is equal to a given percentage of the energy $\mathcal{E}_1$ within the frame, as represented by $\rho = \mathcal{E}_2/\mathcal{E}_1$. The comparative results obtained with the various sub-Nyquist TOA estimators under consideration in this study, are presented in Fig. 3.9, which shows the RMSE of the TOA estimates as a function of ρ at an operating SNR of 25dB. If the level of IFI level is not too large, all the sub-Nyquist estimators can still work properly and maintain the same, or a slightly degraded level of performance. However, when the IFI becomes too large, all the TOA estimators

will degrade significantly.

Finally, Fig. 3.10 compares the RMSE performance of the proposed TOA estimator as a function of the SNR when different time resolutions are used to obtain a finer estimate by searching around the initial estimate $\hat{D}T_c$. The CRB for TOA estimation derived in Section 5 is also shown for reference. From this figure, we conclude that conducting a fine local search using a higher sampling rate can significantly improve the estimation performance. However, this improvement comes at a slightly higher implementation cost. Note that the performance can not reach the CRB since the performance is still limited by the sub-Nyquist sampling; we will elaborate more on this in the next chapter.

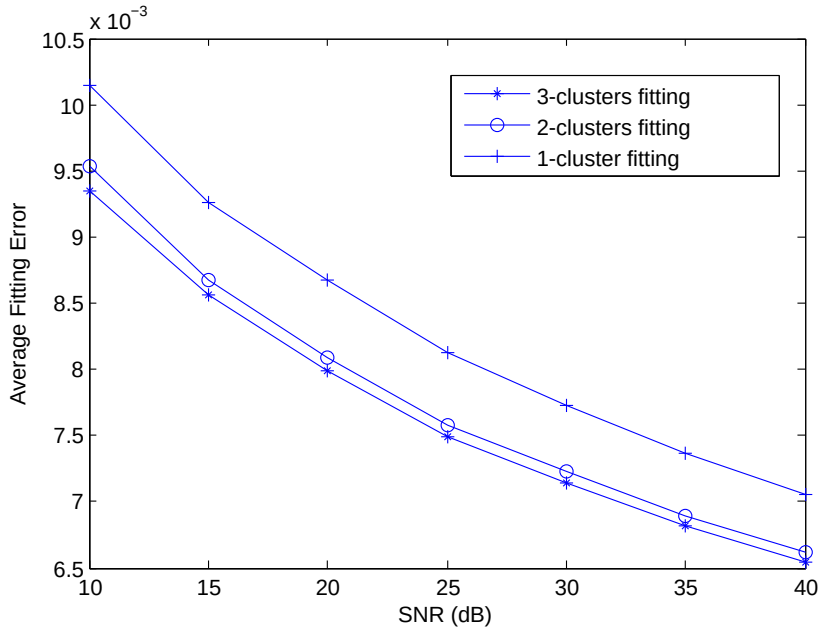

Fig. 3.5 Average APDP fitting error versus SNR.

3.6 Conclusion

In this chapter, we proposed and investigated a joint sub-Nyquist ML-based estimator of the TOA and APDP to UWB impulse radio applications. A parametric model was assumed for the APDP and its parameters were estimated jointly with the unknown TOA by exploiting the interplay between the ML and LS approaches. This is in contrast to previous sub-Nyquist methods which require *a priori* knowledge of the APDP. Through simulations, we showed that the proposed

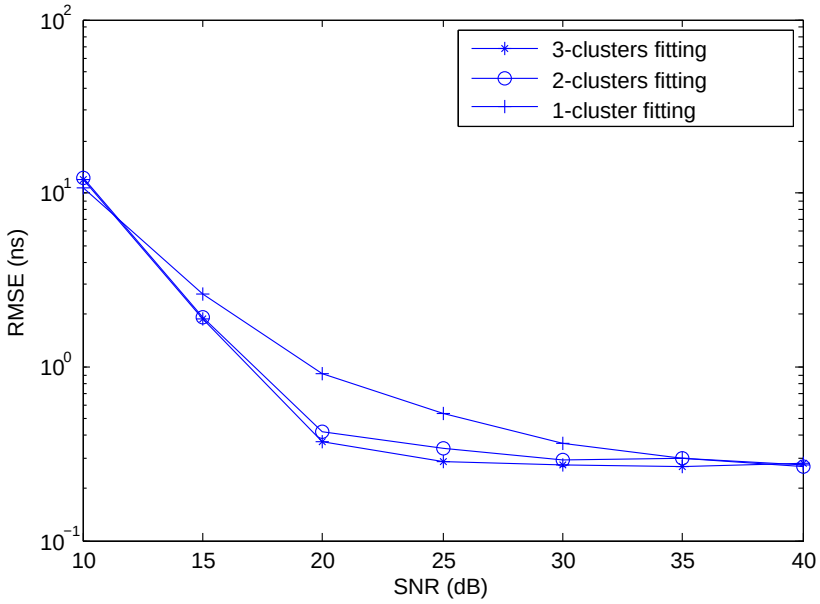

Fig. 3.6 RMSE of proposed TOA estimator for different (assumed) number of clusters.

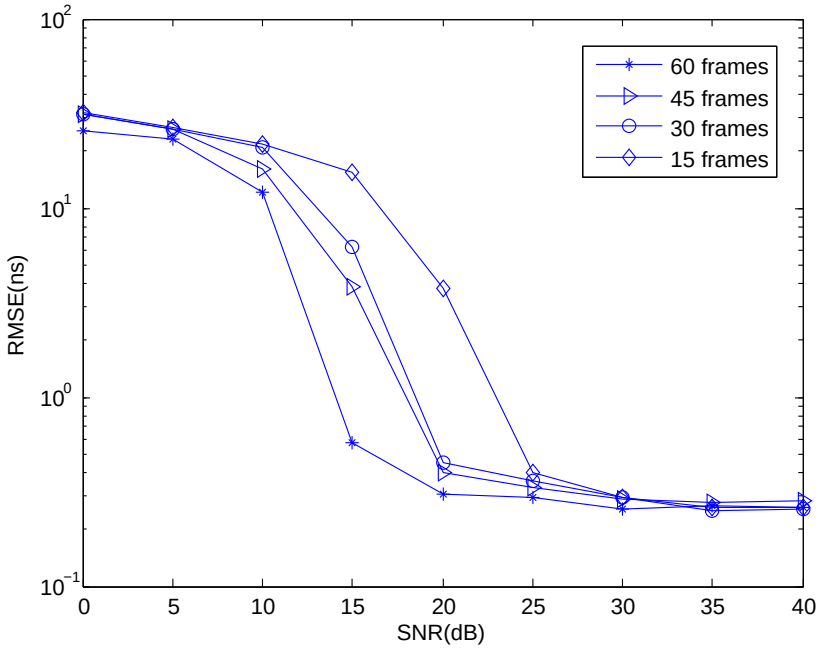

Fig. 3.7 RMSE of proposed TOA estimator for different number of frames.

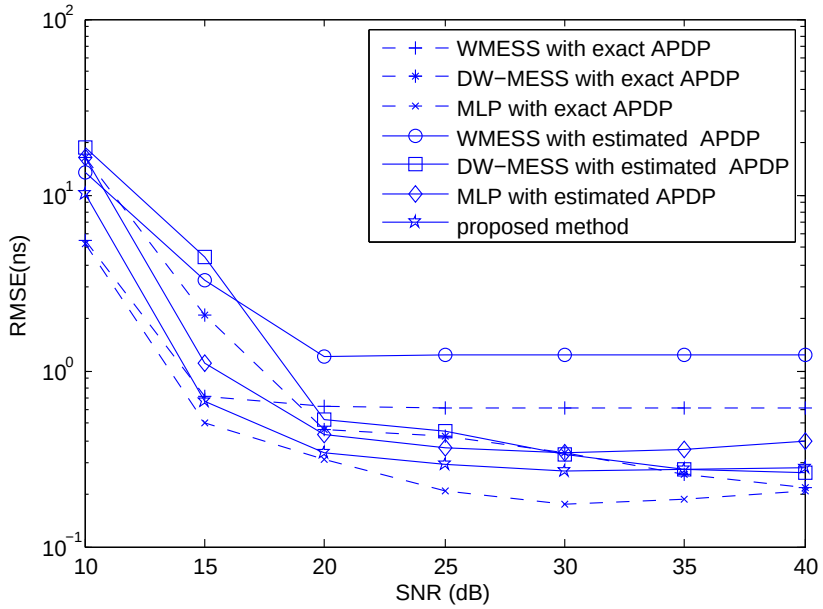

Fig. 3.8 RMSE of TOA estimates for different algorithms.

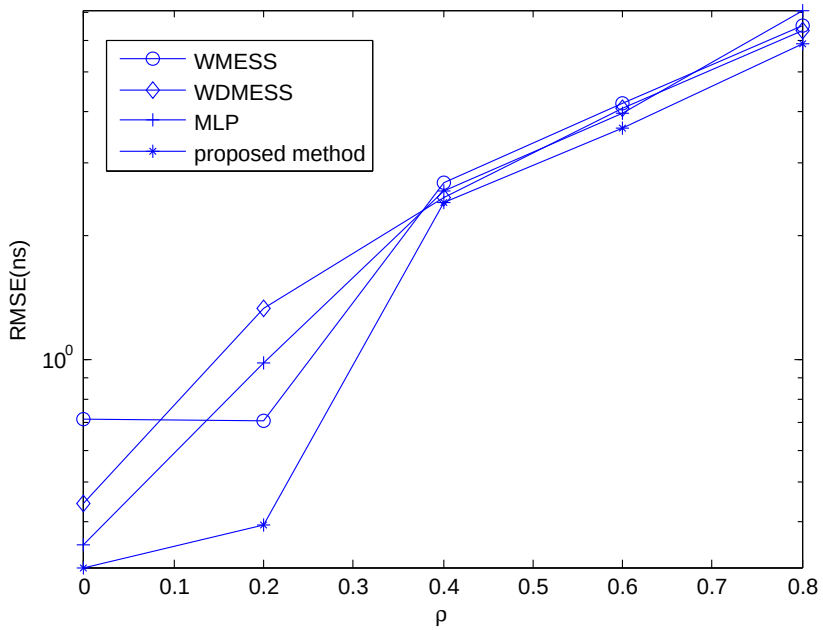

Fig. 3.9 RMSE of TOA estimation with IFI (SNR=25dB).

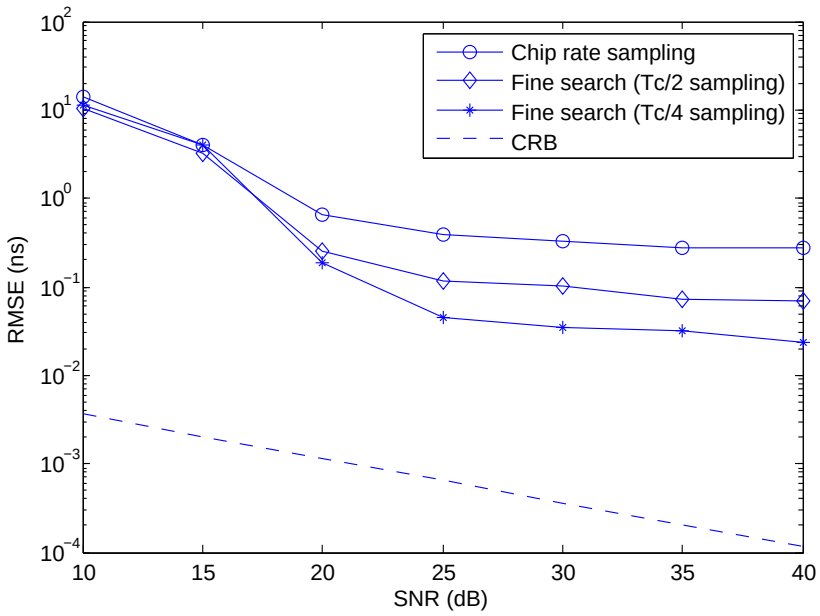

Fig. 3.10 RMSE of proposed TOA estimator for different sampling rates.

TOA estimator has a good accuracy and can outperform earlier methods when using the same estimated APDP. While the joint estimation of the APDP adds to the complexity, the increase is still reasonable since all digital processing is done at the lower chip (sub-Nyquist) rate. The accuracy of the proposed TOA estimator can be improved by fine search with a higher sampling rate.

Chapter 4

Joint TOA and AOA estimation in multi-antenna IR-UWB systems

In this chapter[1], we consider the problem of joint TOA and AOA estimation in IR-UWB systems. To enable estimation of the latter, an antenna array is employed at the receiver side. This chapter is organized as follows. In Section 4.1, the motivation for the work presented in this chapter is discussed. In Section 4.2, we present the IR-UWB system model under study and formulate the estimation problem in mathematical terms. In Section 4.3, we derive a general LLF expression for this problem and expose the processing structure of the joint ML estimator of the TOA and AOA. In Section 4.4, the CRBs for both TOA and AOA are derived for the proposed multipath signal model. In Section 4.5, we discuss practical aspects related to the implementation of the new estimator. Section 4.6 presents the methodology and results of the numerical simulation experiments, including comparisons to the CRB. Finally, Section 4.7 concludes this chapter.

4.1 Motivation

In theory, the number of required readers for localization can be reduced if the AOA of the transmitted pulses can be estimated jointly with the TOAs [72]. In this case, each tag reader must be equipped with an array of antennas and have the capability to process their outputs coherently, allowing for the extraction of spatial information from the observed wavefield. This is possible if the antenna outputs are sampled at a sufficiently high rate to allow for the fine timing accuracy

[1]Parts of Chapter 4 have been presented at the 2013 International Conference on Acoustic, Speech and Signal Processing [102].

needed in coherent spatial processing. A multiple-antenna IR-UWB reader designed for AOA estimation of the transmitted signal will therefore require a much higher level of sophistication than a single-antenna reader performing basic TOA estimation. Nevertheless, considering recent advances in the field of IR-UWB electronics, especially Analog-to-Digital (A/D) converter and demodulator functionality [103], new algorithms with improved performance for the joint TOA/AOA estimation of radio pulses with an antenna array become a real possibility.

Indeed, the literature review of AOA estimation methods presented in Chapter 1 revealed the recent trend of jointly estimating TOA and AOA in order to improve estimation performance. In the methods we have studied, it is common to estimate AOA based on the TDOA between the installed antenna elements. Inspired by the same idea, in this chapter we propose a novel joint estimator of TOA and AOA for a multi-antenna IR-UWB receiver based on the ML criterion. To simplify its implementation, the proposed estimator consists of two steps: (1) preliminary estimation of the TOA and the APDP; (2) joint refinement of the TOA and estimation of the AOA by local maximization of a new LLF which employs the estimates from the first step. Besides preliminary TOA estimation using energy-based threshold crossing, the first step includes the estimation of the APDP using LS fitting to a decaying exponential model, which is not found in prior methods. A key feature of the proposed approach lies in the choice of an original statistical model, in which the primary pulse image and the superposition of the secondary images are represented by a deterministic component and a zero-mean Gaussian random process, respectively. The latter is characterized by a wideband space-time correlation function, which uses a special gating mechanism to represent the onset of the secondary paths (after the primary one) and takes into account the APDP of the multi-path components. This model leads to a previously unknown form of the LLF in step (2). Extensive simulation studies are carried out based on multipath UWB channel models featuring diffuse and directional secondary image fields. In both cases, our approach exhibits superior performance to that of a competing method from the recent literature.

4.2 Problem formulation

We consider a RFID localization system, as depicted in Fig. 4.1, in which a tag equipped with a single antenna transmits an IR-UWB signal. The transmitted signal propagates in a multi-path environment where it is reflected, scattered or diffracted by walls and other objects or surfaces. A tag reader equipped with an antenna array acquires the propagating UWB signal, and estimates relevant parameters (in our case, TOA and AOA), which will be used later for the tag localization.

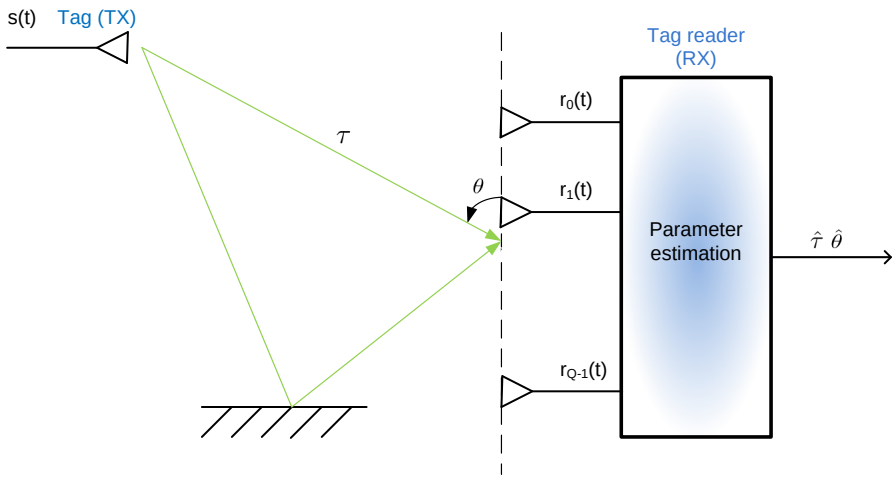

Fig. 4.1 RFID-based localization system.

As per the IEEE 802.15.4a standard, the parameter estimation is performed during the ranging preamble of a synchronization header using a pulse train [92]. As in the previous chapter, the tag-emitted signal $s(t)$ consists of N_{sym} consecutive pulses and is given by

$$s(t) = \sum_{j=0}^{N_{\text{sym}}-1} a_j \sqrt{E_p}\, w(t - jT_{\text{sym}}), \quad 0 \le t \le T_o \tag{4.1}$$

where $w(t)$ represents the transmitted pulse waveform, assumed to have finite duration $[0, T_c]$ and unit energy, and E_p denotes the transmitted energy per pulse. The pulse repetition period is denoted by T_{sym} and the transmitted signal spans a total observation time of $T_o = N_{\text{sym}} T_{\text{sym}}$. For the purpose of ranging, a known training sequence is adopted here, i.e., $a_j = 1, \forall j$.

The transmitted IR-UWB signal $s(t)$ propagates along multiple paths that combine additively at the tag reader, where a ULA of $Q > 1$ identical antenna elements is employed for signal acquisition.[2] Under the far field assumption, the wavefronts arriving at the receiver's ULA along different paths can be taken as planar. In particular, for the primary path (the first one in a LOS environment), the TOA at the qth antenna can be written as

$$\tau_q = \tau + (q - \frac{Q-1}{2})\Delta\tau, \quad q \in \{0, \ldots, Q-1\} \tag{4.2}$$

[2] The use of a ULA is assumed mainly for mathematical convenience; generalization of the proposed techniques to other antenna configurations is conceptually straightforward.

where τ denotes the TOA or propagating delay at the antenna array geometric center and $\Delta\tau$ is the TDOA between adjacent antennas. For a 2-dimensional geometry, the TDOA can be expressed in terms of the AOA, θ, as

$$\Delta\tau = \frac{d}{c}\cos\theta \tag{4.3}$$

where d is the inter-antenna spacing and c is the speed of light.

The propagation channel between the tag and the tag reader's antenna array is modeled as a linear time-invariant Single-Input Multiple-Output (SIMO) system, with components $\mathcal{H}_q\{\cdot\}$ where $q \in \{0, ..., Q-1\}$. In this work, we represent the channel response to the pulse waveform $w(t)$ at the qth antenna as a superposition of two distinct components:

$$\mathcal{H}_q\{w(t)\} = \eta(t-\tau_q) + \zeta_q(t) \tag{4.4}$$

where $\eta(t)$ represents the pulse image arriving along the primary path and $\zeta_q(t)$ represents the total contribution (linear superposition) of the images received along secondary paths, i.e., excluding the primary one. This signal structure is depicted in Fig. 4.2, where the duration of $\eta(t)$ is shown comparable to that of $w(t)$, while that of the secondary images extends from around τ_q to $\tau_q + \tau_{\text{ds}}$, where τ_{ds} is the delay spread of the channel. Note that there may be overlap between the primary and secondary pulse images. In addition, we assume there is no interference between successive pulses, i.e., $\tau_{\text{ds}} < T_{\text{sym}}$. In IR-UWB localization, $s(t)$ has a low duty cycle of the order of 1Mbits/s or less, while τ_{ds} for a typical indoor channel is on the order of a few 100ns or less. This assumption is therefore well justified from a practical standpoint and it is common in the literature (e.g., [94]).

We model the primary pulse image $\eta(t)$ as a deterministic signal, which may possibly include some unknown (nuisance) parameters. A simple such description is $\eta(t) = aw(t)$, where a denotes a (real) path gain. However, more sophisticated filtering operations can be applied to model pulse distortion resulting from the fine (time-unresolvable) structure of the channel or the receiver front-end filters. In this setting, the filtering parameters will be deterministic but unknown, and can be estimated jointly with the desired TOA and AOA.

The superimposed secondary pulse images $\zeta_q(t)$ are modeled as independent Gaussian random processes with zero mean. Considering the dense indoor environments, we represent the space-time cross-correlation of $\zeta_q(t)$ by

$$E[\zeta_q(t)\zeta_{q'}(u)] = \sigma_q(t)\sigma_{q'}(u)\delta_c(t-u)\varrho(q,q') \tag{4.5}$$

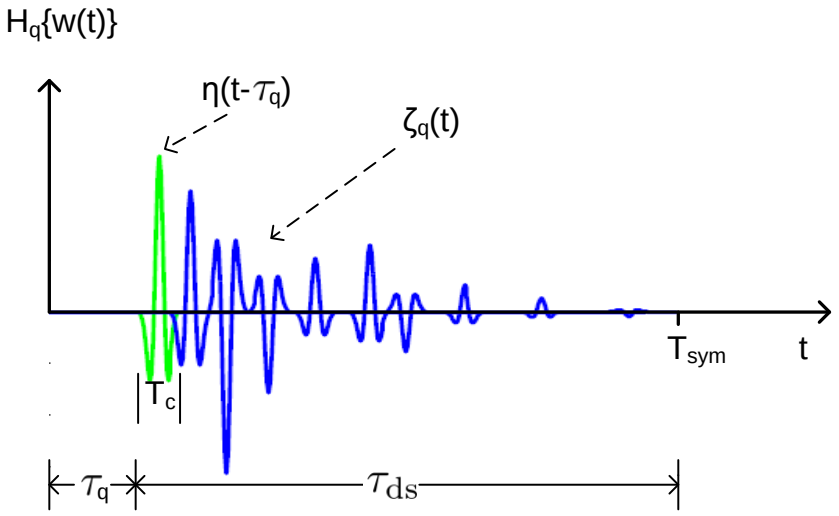

Fig. 4.2 Decomposition of the multi-path channel response to transmitted pulse $w(t)$ into a sum of primary, $\eta(t-\tau_q)$, and secondary, $\zeta_q(t)$, components.

where $\delta_c(t)$ is the Dirac delta function, $\varrho(q,q')$ is the spatial correlation and $\sigma_q^2(t)$ is the instantaneous power (level) of $\zeta_q(t)$. The use of $\delta_c(t-u)$ in (4.5) is motivated by the fact that the extent of the temporal correlation for multipath components is usually very small [27, 99]. Regarding $\varrho(q,q')$, it has been observed that the spatial correlation decreases rapidly with the inter-antenna spacing [104], and accordingly, we set $\varrho(q,q')=1$ for $q=q'$ and 0 otherwise. The instantaneous power level can be further represented by

$$\sigma_q^2(t) = g(t-\tau_q)P(t) \tag{4.6}$$

where $P(t)$ is the APDP and $g(t)$ is a gating function. Specifically, the APDP models the decay in the small-scale average power of the received pulse images as a function of the propagating delay, for an impulse emitted at time $t=0$ [66]. In this work, it is assumed that $P(t)$ is a slowly varying function of time relative to the pulse duration and travel time across the antenna array. The gating function $g(t)$ is introduced to model the onset of the secondary pulse images after the primary one at $t=\tau_q$ and is assumed to satisfy the following conditions: $g(t)=0$ for $t\le 0$, equal to 1 for $t\ge T_c$ and monotonically increasing for $0<t<T_c$.

Finally, the noisy IR-UWB signal received at the qth antenna at time t, after multipath propa-

gation, can be expressed as

$$\begin{aligned} r_q(t) &= \mathcal{H}_q\{s(t)\} + n_q(t) \\ &= \mu_q(t) + \xi_q(t) + n_q(t), \quad 0 \le t \le T_o \end{aligned} \tag{4.7}$$

where

$$\mu_q(t) = \sum_{j=0}^{N_{\text{sym}}-1} \sqrt{E_p}\, \eta(t - \tau_q - jT_{\text{sym}}) \tag{4.8}$$

$$\xi_q(t) = \sum_{j=0}^{N_{\text{sym}}-1} \sqrt{E_p}\, \zeta_q(t - jT_{\text{sym}}) \tag{4.9}$$

and $n_q(t)$ is an additive noise term modeled as a spatially and temporally white Gaussian process with zero mean and known power spectral density level σ_n^2. We assume that the noise terms $n_q(t)$ are statistically independent from the secondary pulse images $\zeta_{q'}(t)$.

We can now describe the problem considered in this chapter as follows: Given the observation of the received antenna signals at the reader, that is $\{r_q(t)\}$ for $0 \le t \le T_o$ and $q \in \{0, \ldots, Q-1\}$, we seek to jointly estimate the TOA and AOA parameters of the primary path, respectively τ and θ in (4.2), which are needed for localizing the tag. A key feature of our proposed approach is the formal consideration of distinct models for the primary pulse image $\eta(t)$ and the combined secondary images $\zeta_q(t)$, and especially the use of the space-time correlation function (4.5)-(4.6) which incorporates the gating and APDP functions. This formulation will allow us to derive a new ML estimator with improved performance, and gain a deeper insight into its operation. While we shall consider the effect of unknown (nuisance) parameters of $\eta(t)$ and $\zeta_q(t)$ on the estimation process, our main interest lies in the estimation of the geometrical TOA and AOA parameters. Appropriately, in our proposed approach, it will be sufficient to use educated guesses of the functions $\eta(t)$, $g(t)$ and $P(t)$ in order to benefit from the merits of the ML formulation. The choice of these functions will be further discussed in Sections 4.5 and 4.6.

4.3 Joint maximum likelihood estimation

In this section, we first derive the LLF for the SIMO system model previously introduced. We then formulate the joint ML estimator of the TOA and AOA parameters, which will play a key role in our proposed scheme.

In practice, the received antenna signals $r_q(t)$ are uniformly sampled at a rate F_s, which is greater than or equal to the Nyquist rate. Therefore, we let $t = nT_s$, where n is an integer and $T_s = 1/F_s$ denotes the sampling period which meets the Nyquist criterion for bandpass signals. In addition, for the sake of simplicity, we assume that each pulse repetition period consists of exactly M time samples, i.e., $T_{\text{sym}} = MT_s$ where M is a positive integer.

Let us represent the set of received antenna signals during the jth symbol by the vector function

$$\mathbf{r}_j(t) = [r_0(t + jT_{\text{sym}}), \ldots, r_{Q-1}(t + jT_{\text{sym}})]^T \tag{4.10}$$

where $r_q(t + jT_{\text{sym}})$ is given by (4.7) and discrete-time $t \in \mathcal{T} = \{nT_s : n = 0, 1, \ldots, M-1\} \subset [0, T_{\text{sym}})$. In the absence of interference between adjacent pulses, with t restricted in this manner, it follows from (4.8) and (4.9) that $\mu_q(t + jT_{\text{sym}}) = \sqrt{E_p}\eta(t - \tau_q)$ and $\xi_q(t + jT_{\text{sym}}) = \sqrt{E_p}\zeta_q(t)$, respectively. Therefore, we can write

$$\mathbf{r}_j(t) = \boldsymbol{\mu}(t) + \boldsymbol{\xi}(t) + \mathbf{n}_j(t) \tag{4.11}$$

where we define

$$\boldsymbol{\mu}(t) = \sqrt{E_p}[\eta(t - \tau_0), \ldots, \eta(t - \tau_{Q-1})]^T \tag{4.12}$$

$$\boldsymbol{\xi}(t) = \sqrt{E_p}[\zeta_0(t), \ldots, \zeta_{Q-1}(t)]^T \tag{4.13}$$

$$\mathbf{n}_j(t) = [n_0(t + jT_{\text{sym}}), \ldots, n_{Q-1}(t + jT_{\text{sym}})]^T. \tag{4.14}$$

In the context of IR-UWB localization, the received pulse train is usually averaged to increase the SNR. Leting $\mathbf{x}(t) = [x_0(t), \ldots, x_{Q-1}(t)]^T$ denote the symbol-averaged array output vector, it follows from (4.11) that

$$\mathbf{x}(t) = \frac{1}{N_{\text{sym}}} \sum_{j=0}^{N_{\text{sym}}-1} \mathbf{r}_j(t) = \boldsymbol{\mu}(t) + \boldsymbol{\xi}(t) + \mathbf{n}(t) \tag{4.15}$$

where the additive noise term $\mathbf{n}(t) = \frac{1}{N_{\text{sym}}} \sum_j \mathbf{n}_j(t)$.

Invoking the Gaussian assumption on the secondary images and background noise processes, it follows that $\mathbf{x}(t)$ is a Gaussian vector process with non-zero mean, $E[\mathbf{x}(t)] = \boldsymbol{\mu}(t)$, and $Q \times Q$

matrix auto-covariance function

$$\begin{aligned}\mathbf{K}_x(t,u) &= E[(\mathbf{x}(t)-\boldsymbol{\mu}(t))(\mathbf{x}(u)-\boldsymbol{\mu}(u))^T] \\ &= \mathbf{K}_\xi(t,u)+\mathbf{K}_n(t,u)\end{aligned} \tag{4.16}$$

where, in turn, $\mathbf{K}_\xi(t,u) = E[\boldsymbol{\xi}(t)\boldsymbol{\xi}(u)^T]$ and $\mathbf{K}_n(t,u) = E[\mathbf{n}(t)\mathbf{n}(u)^T]$ denote the auto-covariance functions of $\boldsymbol{\xi}(t)$ and $\mathbf{n}(t)$, respectively. In these expressions, u is a discrete-time variable with the same range as t. Using the expression (4.5)-(4.6) of the space-time cross-correlation function of $\zeta_q(t)$, and taking into account the band-limited (i.e., anti-aliasing) filtering implicit in the uniform sampling of the antenna signals, we obtain

$$\mathbf{K}_\xi(t,u) = E_p\delta(t-u)\,\mathbf{D}(t)\frac{1}{T_s} \tag{4.17}$$

where $\delta(t)$ is the Kronecker delta function[3] and $\mathbf{D}(t)$ is a $Q\times Q$ diagonal matrix with qth diagonal entry $\sigma_q^2(t)$. Meanwhile, we have

$$\mathbf{K}_n(t,u) = \sigma_{\tilde{n}}^2\delta(t-u)\mathbf{I}_Q\frac{1}{T_s} \tag{4.18}$$

where we define $\sigma_{\tilde{n}}^2 = \sigma_n^2/N_{\text{sym}}$ and $\mathbf{I}_Q$ is an identity matrix of order Q.

Let the unknown parameters under estimation be represented by the row vector $\boldsymbol{\phi} = [\tau, \theta, \boldsymbol{\phi}_\eta, \boldsymbol{\phi}_\zeta]$, where $\boldsymbol{\phi}_\eta$ contains the (nuisance) parameters associated with the pulse image from the primary path, $\eta(t)$, and $\boldsymbol{\phi}_\zeta$ contains those associated with the pulse images from the secondary paths, $\{\zeta_q(t)\}_{q=0}^{Q-1}$. Also let $\boldsymbol{x}$ denote the complete set of symbol-averaged array output vectors available for estimation, i.e., $\{\mathbf{x}(t) : t\in\mathcal{T}\}$. For the non-zero mean Gaussian signal model under consideration in this study, the LLF of the observations can be expressed (up to a constant factor) in the form [105]

$$\ln\Lambda(\mathbf{x};\boldsymbol{\phi}) = -\frac{1}{2}(l_1(\mathbf{x};\boldsymbol{\phi})+l_2(\boldsymbol{\phi})). \tag{4.19}$$

The two terms composing this expression are examined in detail below.

The data-dependent term $l_1(\mathbf{x};\boldsymbol{\phi})$ is given by

$$l_1(\mathbf{x};\boldsymbol{\phi}) = \sum_{t\in\mathcal{T}}\sum_{u\in\mathcal{T}}(\mathbf{x}(t)-\boldsymbol{\mu}(t))^T\mathbf{K}_x^{-1}(t,u)(\mathbf{x}(u)-\boldsymbol{\mu}(u)) \tag{4.20}$$

[3]That is, $\delta(nT_s)$ is equal to 1 for $n=0$ and to 0 for all integers $n\neq 0$.

where the quantity $\mathbf{K}_x^{-1}(t,u)$ denotes the inverse kernel of the auto-covariance function $\mathbf{K}_x(t,u)$ in (4.16), and is obtained as the solution to the inverse problem:

$$\sum_{u\in\mathcal{T}} \mathbf{K}_x(t,u)\mathbf{K}_x^{-1}(u,v) = \delta(t,v), \quad (t,u) \in \mathcal{T}^2. \tag{4.21}$$

For the special form of the auto-covariance function in (4.16), it can be verified that the solution to (4.21) is given by:

$$\mathbf{K}_x^{-1}(t,u) = \delta(t-u)T_s(E_p\mathbf{D}(t) + \sigma_{\tilde{n}}^2\mathbf{I}_Q)^{-1}. \tag{4.22}$$

Substituting this expression in (4.20), and after further manipulations, we find that

$$l_1(\mathbf{x};\boldsymbol{\phi}) = T_s \sum_{q=0}^{Q-1} \sum_{t\in\mathcal{T}} \frac{[x_q(t) - \sqrt{E_p}\eta(t-\tau_q)]^2}{E_p g(t-\tau_q)P(t) + \sigma_{\tilde{n}}^2}. \tag{4.23}$$

The second term in (4.19), $l_2(\boldsymbol{\phi})$, is given by

$$l_2(\boldsymbol{\phi}) = \ln\det\mathcal{K} \tag{4.24}$$

where $\mathcal{K}$ is a Hermitian matrix of order MQ, composed of M^2 blocks of size $Q\times Q$, with $\mathbf{K}_x(t,u)$ as its (t,u)th block. In the situation of interest here, due to the presence of the delta function in $\mathbf{K}_x(t,u)$ (4.16)-(4.18), this term simplifies to

$$l_2(\boldsymbol{\phi}) = T_s \sum_{q=0}^{Q-1} \sum_{t\in\mathcal{T}} \ln\left[E_p g(t-\tau_q)P(t) + \sigma_{\tilde{n}}^2\right]. \tag{4.25}$$

Given the set $\mathbf{x}$ of symbol-averaged array output vectors, the joint ML estimator of parameter vector $\boldsymbol{\phi}$ is obtained by maximizing the LLF $\ln\Lambda(\mathbf{x};\boldsymbol{\phi})$ in (4.19), or equivalently:

$$\hat{\boldsymbol{\phi}}_{\mathrm{ML}} = \arg\min_{\boldsymbol{\phi}\in\mathcal{P}} \left(l_1(\mathbf{x};\boldsymbol{\phi}) + l_2(\boldsymbol{\phi})\right) \tag{4.26}$$

where $l_1(\mathbf{x};\boldsymbol{\phi})$ and $l_2(\boldsymbol{\phi})$ are given by (4.23) and (4.24), respectively, and $\mathcal{P}$ denotes the parameter space over which the search is performed. In practice, the search range for the TOA and AOA parameters, τ and θ, will be restricted by geometrical considerations. This aspect is further discussed in Section 4.5. Other limitations may apply to the search ranges of the nuisance

parameters in ϕ_η and ϕ_ζ when they are part of the estimation process.

It is worth noting that, for $l_2(\phi)$, the inner sum over t is almost the same for the different possible values of the unknown delay τ and differential delay $\Delta\tau$. Indeed, as long as the channel delay spread is smaller than the pulse repetition period T_{sym}, the value of this term is almost constant. Therefore, maximizing the data dependent term $l_1(\mathbf{x};\phi)$ with respect to τ and θ becomes our main consideration. This term dictates the signal processing operations that need to be performed on the observed data $\mathbf{x}$ to obtain $\hat{\phi}_{\text{ML}}$. Upon closer examination of (4.23), we note that the ML processing is tantamount to obtaining, for each antenna index q, the best match between $x_q(t)$ and $\sqrt{E_p}\eta(t-\tau_q)$ during the initial period, while ensuring that the instantaneous power in the residual signals $x_q(t) - \sqrt{E_p}\eta(t-\tau_q)$ conforms to the available *a priori* information about the APDP. In the low SNR regime where $E_p \ll \sigma^2_{\bar{n}}$, the ML processor simply measures and seeks to minimize the energy of the difference signals at the Q antennas over the symbol duration.

4.4 Cramer Rao Bound

As discussed in the previous section, of the four elements comprising the unknown parameter vector $\phi = [\tau, \theta, \phi_\eta, \phi_\zeta]$ we are interested in just the first two, τ and θ. The first step towards derivation[4] of the CRB of τ and θ is to evaluate the FIM given by

$$J = \begin{bmatrix} J_{11} & J_{12} \\ J_{21} & J_{22} \end{bmatrix} = -\begin{bmatrix} E\left[\frac{\partial^2 \ln \Lambda(\mathbf{x};\tau,\theta)}{\partial^2 \tau}\right] & E\left[\frac{\partial^2 \ln \Lambda(\mathbf{x};\tau,\theta)}{\partial \tau \partial \theta}\right] \\ E\left[\frac{\partial^2 \ln \Lambda(\mathbf{x};\tau,\theta)}{\partial \theta \partial \tau}\right] & E\left[\frac{\partial^2 \ln \Lambda(\mathbf{x};\tau,\theta)}{\partial^2 \theta}\right] \end{bmatrix}. \tag{4.27}$$

First, we focus on entry J_{11} in (4.27). Using "prime" to denote differentiation w.r.t. time t, as in, e.g., $\eta'(t) = \frac{\partial \eta(t)}{\partial t}$, we have

$$\frac{\partial \ln \Lambda(\mathbf{x};\tau,\theta)}{\partial \tau} = -\frac{T_s}{2}\sum_{q=0}^{Q-1}\sum_{t\in\mathcal{T}}\left[\frac{2\sqrt{E_p}y_q(t)\eta'(t-\tau_q)}{\gamma(t,\tau_q)} - \right.$$

$$\left.\left(\frac{y_q(t)^2}{\gamma(t,\tau_q)^2} + \frac{1}{\gamma(t,\tau_q)}\right)\frac{\partial \gamma(t,\tau_q)}{\partial \tau}\right] \tag{4.28}$$

[4] Although closed form expressions for the CRB of TOA and AOA estimation can be found in previous works [106, 46], the CRB for the signal model considered here still needs to be investigated.

where

$$\gamma(t,\tau_q) = E_p g(t-\tau_q)P(t) + \sigma_{\tilde{n}}^2 \tag{4.29}$$

$$y_q(t) = x_q(t) - \sqrt{E_p}\eta(t-\tau_q) \tag{4.30}$$

and

$$\frac{\partial\gamma(t,\tau_q)}{\partial\tau} = -E_p g'(t-\tau_q)P(t). \tag{4.31}$$

Taking the derivative of (4.28), and applying the expectation operation, we can write J_{11} as

$$J_{11} = -E[\frac{\partial^2 \ln\Lambda(\mathbf{x};\tau,\theta)}{\partial^2\tau}] = \sum_{q=0}^{Q-1} S_q \tag{4.32}$$

where we define

$$S_q = \sum_{t\in\mathcal{T}} [\frac{E_p\eta'(t-\tau_q)^2}{\gamma(t,\tau_q)} + \frac{1}{2\gamma(t,\tau_q)^2}(\frac{\partial\gamma(t,\tau_q)}{\partial\tau})^2]T_s. \tag{4.33}$$

To obtain (4.32) we used the fact that, according to the channel model described in Section II, we have

$$E[y_q(t)] = 0 \tag{4.34}$$

and

$$E[y_q(t)^2] = \gamma(t,\tau_q). \tag{4.35}$$

Due to the slowly varying nature of the APDP and the fact that no signal power is received at the very beginning and end of a symbol interval, it follows that, in practice, S_q does not vary appreciably with the antenna index. That is, $S_q \approx S$ for all q, where we can write

$$S = \mathrm{SNR}(S_1 + S_2) \tag{4.36}$$

with

$$S_1 = T_s \sum_{t\in\mathcal{T}} \frac{\eta'(t-\tau)^2}{1+\mathrm{SNR}g(t-\tau)P(t)} \tag{4.37}$$

$$S_2 = \frac{T_s}{2} \sum_{t\in\mathcal{T}} \frac{\mathrm{SNR}g'(t-\tau)^2P(t)^2}{(1+\mathrm{SNR}g(t-\tau)P(t))^2} \tag{4.38}$$

and we define SNR = $E_p/\sigma^2_{\tilde{n}}$. Therefore, we finally obtain

$$J_{11} = S\,Q. \tag{4.39}$$

Performing similar calculations for the rest of the entries of the FIM, it is straightforward to check that they share a common form, except for a multiplicative factor that accounts for the relationship between τ_q in (4.2)-(4.3) and the specific combination of the parameters τ and θ involved in each entry. In particular, we have that

$$J_{12} = J_{21} = -E[\frac{\partial^2 \ln \Lambda(\mathbf{x};\tau,\theta)}{\partial\tau\partial\theta}] \tag{4.40}$$

$$= S\sum_{q=0}^{Q-1}\frac{\partial\tau_q}{\partial\theta} = 0 \tag{4.41}$$

and

$$J_{22} = -E[\frac{\partial^2 \ln \Lambda(\mathbf{x};\tau,\theta)}{\partial^2\theta}] \tag{4.42}$$

$$= S\sum_{q=0}^{Q-1}(\frac{\partial\tau_q}{\partial\theta})^2 = S\frac{d^2}{c^2}(\sin\theta)^2\Psi \tag{4.43}$$

where the last equalities in (4.41) and (4.43) follow from (4.2), and the constant Ψ is defined as $\Psi = Q(Q-1)(Q+1)/12$.

Consequently, the CRBs of τ and θ are given by

$$\mathrm{CRB}(\tau) = J_{11}^{-1} = \frac{1}{S\,Q} \tag{4.44}$$

and

$$\mathrm{CRB}(\theta) = J_{22}^{-1} = \frac{c^2}{S\,d^2(\sin\theta)^2\Psi}. \tag{4.45}$$

We can now make the following observations:

1. In the absence of secondary paths, $g(t) = 0$ and S reduces to

$$S = \mathrm{SNR}\int_0^{T_c}\eta'(t)^2dt. \tag{4.46}$$

In this case, (4.44) and (4.45) are identical to the conventional form of the CRB found in the literature [106, 46].

2. In practice, the transmitted signal will be subjected to multipath, that is, $g(t) \neq 0$. If there is overlap between the primary and secondary images (in which case, the overlapping secondary images act as interference in the estimation), the denominator in (4.37) will be larger than $\sigma_{\bar{n}}^2$ over a corresponding time interval. Therefore, the value of S_1 will be reduced and, in turn, this will contribute to an increase of the CRB.

3. Recall that $g(t)$ is used to characterize the onset of the secondary paths. Therefore, the instantaneous power level of the secondary images, as given by $\sigma_q^2(t)$ in (4.6), provides some information about the unknown delay τ_q through the function $g(t-\tau_q)$. In this respect, a sharp transition in the term $g(t)$ would contribute to an increase of the term S_2 in (4.38), and thereby reduce the CRB.

4. Finally, we note that the achievable performance of both TOA and AOA estimators depends on the pulse shape, SNR, total number of antennas Q and the number of symbol N_{sym} in the observation period. While the analysis was carried out for a ULA, the use of a different array geometry would also affect the performance.

These properties of the CRB shed additional light on the achievable performance level of joint TOA/AOA estimators in the presence of overlapping primary and secondary images.

4.5 Practical implementation

According to the developments in Section 4.3, in order to obtain the joint ML estimates of the unknown TOA and AOA parameters, we need to minimize the data dependent term of the LLF, as given by expression (4.23). Assuming that the required *a priori* information about the APDP $P(t)$ and the primary pulse image $\sqrt{E_p}\eta(t)$ is available, this minimization can be performed in theory by carrying a full 2D search over the set of permissible values for τ and θ. The computational cost associated with a full search is, however, prohibitive and this approach is not feasible practically. Instead, we consider a low-cost alternative, shown in Fig. 4.3, that consists of two steps: In the first step, we perform a preliminary estimation of the TOAs τ_q, based on which we then obtain suitable estimates of $P(t)$ and $\sqrt{E_p}\eta(t)$. In the second step, using the obtained estimates, we find the best combination of τ and θ that minimizes (4.23) via a simplified search strategy that takes

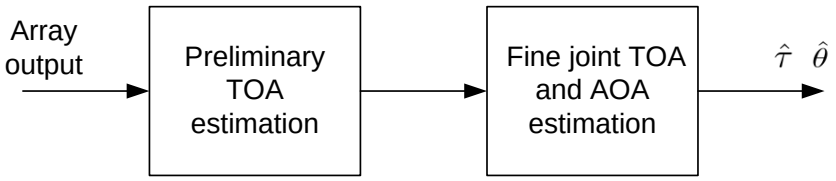

Fig. 4.3 The implementation block diagram.

advantage of the preliminary TOAs along with localized time domain interpolation. The detailed description that follows covers the following aspects of the proposed method: preliminary TOA estimation, subsequent estimation of *priori* information (i.e., APDP and primary pulse image), 2D search of LLF for optimum parameters with interpolation, and finally, complexity analysis.

4.5.1 Preliminary TOA estimation

As with many other high-resolution techniques for joint TOA/AOA estimation of UWB signals, our proposed approach will require a preliminary estimation of the unknown TOAs in order to reduce the size of the search space and minimize the complexity of the final estimation. Several low-complexity TOA estimators are available for this purpose from the literature. Among these, energy detection approaches that do not require explicit knowledge of the pulse shape are well suited for this task. In particular, a simple energy detector based on a threshold crossing (TC) as in [32] can be adopted for this purpose. This technique can be applied at a single antenna or independently at multiple antennae, followed by averaging of the multiple TOA estimates.

Specifically, in the TC-based method, the TOA estimate at the qth antenna is obtained as the smallest value of time t for which the instantaneous power at the antenna output, $x_q^2(t)$, exceeds a given threshold λ. That is

$$\hat{\tau}_q = \arg \min_{0<t<T_u} \{x_q^2(t) > \lambda\} \tag{4.47}$$

where T_u is the initial search range (uncertainty region) for the TOA. In our work, the value of the threshold λ is adjusted experimentally to obtain the best TOA estimation performance, considering the trade-off between the probabilities of false alarm and missed detection. Once TOA estimates $\hat{\tau}_q$ are obtained for each one of the antennas, we can further compute a LS estimate of τ as [49, 50]

$$\hat{\tau}_{LS} = \frac{1}{Q} \sum_{q=0}^{Q-1} \hat{\tau}_q. \tag{4.48}$$

4.5.2 Estimation of *a priori* information

The required *a priori* information needed to implement the proposed joint ML estimator consists of two elements, namely: the APDP $P(t)$ and the primary pulse image $\sqrt{E_p}\eta(t)$. In practice, this information may not be readily available and it therefore needs to be estimated before hand. While this estimation can be done jointly with the desired TOA and AOA through the parametric model introduced in Section 4.2, and especially the nuisance parameters ϕ_ζ and ϕ_η, it may impose a significant computational burden. In this work, to limit the processing complexity, we consider an alternative approach in which the required *a priori* information is obtained separately through simplified estimators. Still, as will be shown in Section 6, this is adequate to obtain significant performance gains in the joint, ML-based TOA/AOA estimation. Below, we discuss in further details the determination of $P(t)$ and $\sqrt{E_p}\eta(t)$.

In the context of UWB propagation, the APDP is typically modeled as the superposition of doubly-exponential decaying clusters with Poisson inter-arrival times, as per the Saleh-Valenzuela model [6]. Here, we propose the use of a single decaying exponential, as given by

$$P(t) = \beta e^{-\alpha t} \tag{4.49}$$

where $\alpha > 0$ is the decay rate and β is the peak power level. To estimate the APDP, we propose to fit the instantaneous power at the output of a selected antenna to this model. Let $l_o = \lfloor \hat{\tau}_{LS}/T_s \rfloor$ and $L = \lfloor \tau_{ds}/T_s \rfloor$ respectively denote the LS estimate of τ and the maximum channel delay spread in samples, with $\lfloor \cdot \rfloor$ being the floor function. We seek the choice of α and β that yields the best fit between the segment of $P_0(l) = x_0((l_o + l)T_s)^2$ from $l = 0$ to $L - 1$, and the function $\beta e^{-l\alpha}$. As in Chapter 3, we perform the curve fitting in the log domain using a weighted LS criterion, i.e.,

$$\min_{\alpha,\beta} \sum_{l=0}^{L-1} \mu_l \left| \ln P_0(l) - (\ln\beta - l\alpha) \right|^2. \tag{4.50}$$

In this approach, the weight $\mu_l = 1$ if there is a local maximum, i.e., $P_0(l-1) < P_0(l) > P_0(l+1)$, and $\mu_l = 0$ otherwise. This choice of μ_l allows us to include in the fitting only the local maxima, as they are more likely to correspond to multipath components, and to mask out the noisy low power data points. Denoting as $\hat{\beta}$ and $\hat{\alpha}$ the solutions to (4.50), we obtain a preliminary estimate of the APDP as

$$\hat{P}(nT_s) = \hat{\beta} e^{-\hat{\alpha}(n - l_o)}, \quad n = 0, ..., M-1. \tag{4.51}$$

where $M = \lfloor T_f/T_s \rfloor$. We note that, the initial samples of $\hat{P}(t)$ are not critical in (4.23) since they will be zeroed by the gating function $g(t - \tau_q)$. It is worth noting that, in Chapter 3, there is no preliminary TOA estimation stage. The TOA is estimated together with the APDP, and therefore the fidelity requirement for the APDP is higher, that is, a more sophisticated model that describes well the clusters structure is needed. In the joint estimation considered here, the APDP is used as part of a weighting function in the LLF (4.23), which in turn is used in the fine estimation stage only. In general, we have found through simulations that the use of a single cluster model is adequate to exploit the main benefits of this weighting mechanism. Therefore, for the sake of simplicity in implementation, we have chosen to use a single exponential in modeling the APDP in this work.

Due to local (small-scale) channel dispersion as well as the effects of the transmit and receive filters, the shape of the primary pulse image $\eta(t)$ will be distorted, when compared to the originally transmitted pulse waveform $w(t)$. This distortion can be significant; we observed that for the type of multipath channels under consideration in this work, the use of the known pulse shape $w(t)$ in place of $\eta(t)$ does not give satisfactory results . Therefore, it is necessary to estimate the scaled primary primary image $\sqrt{E_p}\eta(t)$ prior to carrying the search for the minimizers of (4.23). To this end, we proposed to estimate this quantity simply as a time-shifted version of $x_0(t)$ over an interval of duration T_c. Specifically, for each candidate values of τ and θ, we replace the function $\sqrt{E_p}\eta(t)$ in (4.23) by

$$\sqrt{E_p}\hat{\eta}(t;\tau_0) = x_0(t+\tau_0), \quad 0 \le t < T_c. \tag{4.52}$$

As will be demonstrated through simulations, this approach is robust to small-scale distortion and leads to satisfactory performance in the absence of exact knowledge of the received pulse shape.

4.5.3 Parameter search and interpolation

With the assumed knowledge of the APDP $P(t)$ and primary pulse image $\sqrt{E_p}\eta(t)$, the joint ML estimator of the TOA τ and AOA θ can now be obtained as the minimizers

$$(\hat{\tau}, \hat{\theta}) = \arg \min_{(\tau,\theta)\in\mathcal{P}} l_1(\mathbf{x};\tau,\theta) \tag{4.53}$$

where the objective function is computed according to (4.23) and $\mathcal{P}$ is the set of permissible values over which the 2D search is performed. The choice of the search space $\mathcal{P}$ is further discussed in next part below.

Once a local optimizer has been found, refined estimates of the desired parameters with improved resolution can be obtained through a final interpolation of the objective function. That is, the time dependent terms in (4.23) will be replaced by their interpolated versions and the 2D search will be resumed with a finer step size near the previously found minimizer. In the sequel, we refer to the refined search step as T_{int}, which is typically set to T_s/K_{int}, with K_{int} a positive integer. In this work, we use interpolation based on quadratic polynomial fit, but other interpolation methods could be used as well. The performance of the proposed estimator depends on the final value of T_{int}, and in general, reducing the value of this parameter contributes to a decrease of the estimator variance. However, the trade-off between accuracy and complexity should always be considered.

4.5.4 Computationall complexity

An advantage of the proposed joint estimator of the TOA and AOA is the relatively moderate computational complexity of its realization, as explained next.

In the first step, the main computation cost lies in the preliminary estimation of the TOA and the APDP. According to the TC method, once a suitable threshold λ has been chosen in (4.47), the TOA estimation cost is mainly dictated by the size of the search range, and is therefore upper bounded by $Q\lfloor T_u/T_s \rfloor$, where Q is the number of antennas. The LS estimation of the APDP aims to represent a set of power measurements by a straight line in the log domain, or equivalently, a product $\boldsymbol{A}\boldsymbol{v}$, where $\boldsymbol{A}$ is a known matrix of size $m \times 2$ ($m < L$) and $\boldsymbol{v} = [\alpha, \ln\beta]^T$ is the vector of unknown parameters. The efficient implementation of the LS method then involves the QR factorization of matrix $\boldsymbol{A}$, with a cost of $8m$, followed by the computation of the unknown parameters with a cost of $4m$. Therefore, the total cost for the LS fitting is $12m$, which is linear in m.

In the second step, the main cost lies in the computation of the objective function (4.23) over the two-dimensional search range of interest. According to our previous discussion and based on further experimentation, we found that only a small search range is needed to obtain adequate estimation results. In particular, the search for the TOA will be limited to K_1 samples around the previously obtained estimate $\hat{\tau}_{LS}$, where K_1 is a small integer. The search over θ will be limited to a non-uniform set of $K_2 = 2\lfloor d/cT_s \rfloor + 1$ values given by $\theta_k = \arccos(kcT_s/d)$, where the range of $|k| \leq \lfloor d/cT_s \rfloor$ depends on the antenna separation and the sampling period.

Therefore, the two-dimensional search space consists of K_1K_2 points in total, where for each

point, the evaluation of (4.23) requires $5QM$ numerical operations. We find that the complexity of the 2D search is consequently less than $5K_1K_2QM$ operations per application of the algorithm. In our experiments, typical values of the product K_1K_2 are on the order of 1000 or less, as will be elaborated upon in the next section.

4.6 Numerical results

In this section, computer simulations are used to evaluate the performance of the proposed joint estimator of the TOA and AOA, and the corresponding results are discussed. A recently proposed scheme from the literature as well as the CRB are used as benchmarks in this evaluation. Also, for completeness, results are presented for two different types of secondary image fields, i.e., diffuse and directional.

4.6.1 Methodology

We use a Gaussian doublet as the transmitted pulse $w(t)$ with effective bandwidth $B = 4$GHz. The other system parameters of interest on the transmitter side are chosen as follows: pulse duration $T_c = 0.5$ns, pulse repetition period $T_{\text{sym}} = 200$ns and number of transmitted pulses $N_{\text{sym}} = 1000$. The receiver is equipped with a ULA of $Q \in \{2, 3, 4\}$ identical antenna elements, with inter-element spacing $d = 50$cm, except for the the study in Fig. 4.7 where the antenna spacing is varied. The nominal sampling rate at the receiver is $F_s = 16$GHz. The UWB radio channels are generated using the models in the IEEE 802.15.4a standard [6]. To properly emulate the plane wave propagation, spatial dependence should be introduced when an antenna array is employed at the receiver. Accordingly, certain modifications are needed to account for this aspect. In particular, we generate the channel response according to model CM1 (residential LOS) and then add the spatial dependence to the model according to [107, 108]. That is, the AOA of each path follows a Laplacian distribution with a cluster mean value uniformly distributed in a given range and a standard deviation of 5° for each cluster.

For each Monte Carlo run, we synthesize a SIMO channel according to the above approach and use it to generate the received antenna signals, to which we add white Gaussian noise at the desired power level. This data is used to jointly estimate the TOA and AOA by means of our newly proposed approach, realized in two steps as described in Section 4.5. In the first step, we set the initial search range to $T_u = 80$ns, while in the second step, considering the above choices

for the UWB setup, we use $K_1 = 17$ and $K_2 = 55$ in defining the size of the two-dimensional search space (prior to interpolation). Regarding the gating function $g(t)$ needed in the evaluation of (4.23), in the absence of further *a priori* knowledge, we make the simplest possible choice and use a unit step function with delay T_c. We compare our approach to the recently proposed method from [50] as well as the CRB derived in Section 4.4. As described in Chapter 2, [50] also estimated TOA of qth antenna through TC method. Similar to the proposed method, the obtained TOAs are then used to estimate the TDOA and reference TOA. However, the last step is quite different, the method in [50] only attempts to improve TDOA by maximize energy sum using fine search over 1D interval while the proposed method minimizes the developed LLF function using 2D fine search. The performance of the joint estimators of the TOA and AOA is evaluated in terms of the root mean square error (RMSE), based on a sample size of 500 runs using independent channels and additive noise realizations, and shown plotted as a function of the SNR = E_p/σ_n^2.

4.6.2 Diffuse image field

This situation, which is the most typical case for UWB applications, occurs in dense, highly reverberant environments, where a large number of secondary images impinge on the reader's antenna array from a wide range of directions. In our computer implementation of the SIMO UWB channel, this configuration is achieved by selecting the mean AOA of each cluster from a uniform distribution over the range $[45^o, 135^o]$.

Fig. 4.4 compares the AOA estimation performance of our proposed method to that in [50] for ULAs with $Q = 3$ and 4 antennas. While the AOA estimation accuracy of both methods improves as the number of antennas increases, it can be seen that the proposed method achieves a significantly better accuracy under the same choice of parameters. At high SNR, the attainable RMSE value of the proposed method is only limited by the step size used in the ML search (represented as the sampling limit in Fig. 4.4). To obtain the CRB value, in the CRB expression (4.44) we use a gating function that linearly ramps up from 0 to 1 over the interval $[T_c - T_{\text{rise}}, T_c]$ where T_{rise} represents the overlap between the primary and secondary paths. More specifically,

$$g(t) = \begin{cases} 0 & t \le T_c - T_{\text{rise}} \\ \frac{t - T_{\text{rise}}}{T_{\text{rise}}}, & T_c - T_{\text{rise}} < t \le T_c \\ 1, & T_c \le t \end{cases} \tag{4.54}$$

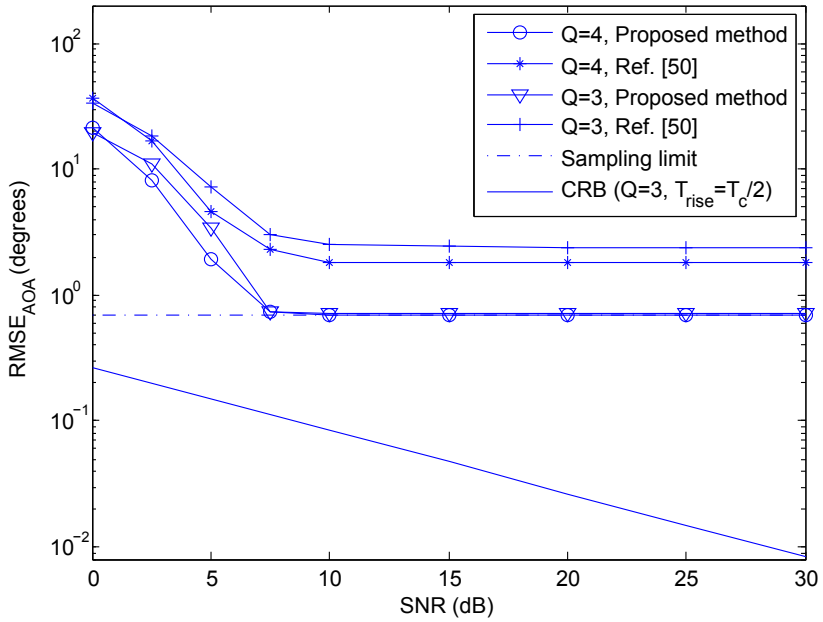

Fig. 4.4 RMSE of AOA estimates versus SNR for different numbers of antennas (F_s=16GHz).

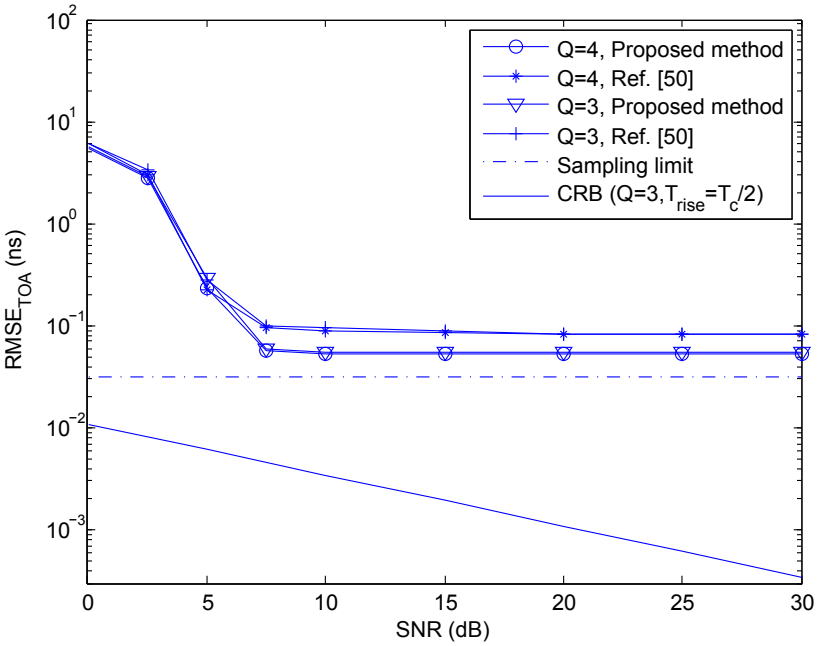

Fig. 4.5 RMSE of TOA estimates versus SNR for different numbers of antennas (F_s=16GHz).

Results for TOA estimation in Fig. 4.5 also show a superior performance with the proposed method.

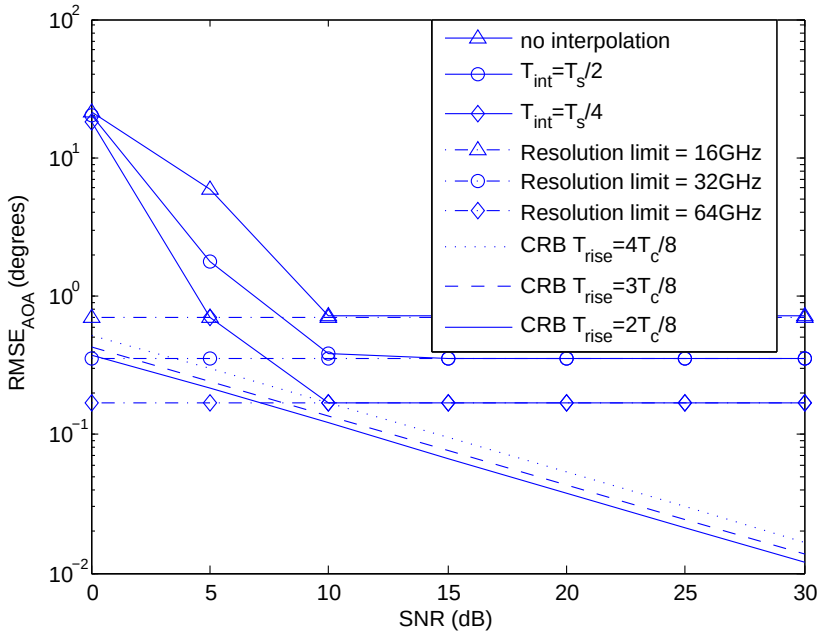

Fig. 4.6 RMSE of AOA estimates of proposed method versus SNR for different resolutions in the interpolation step (Q=2).

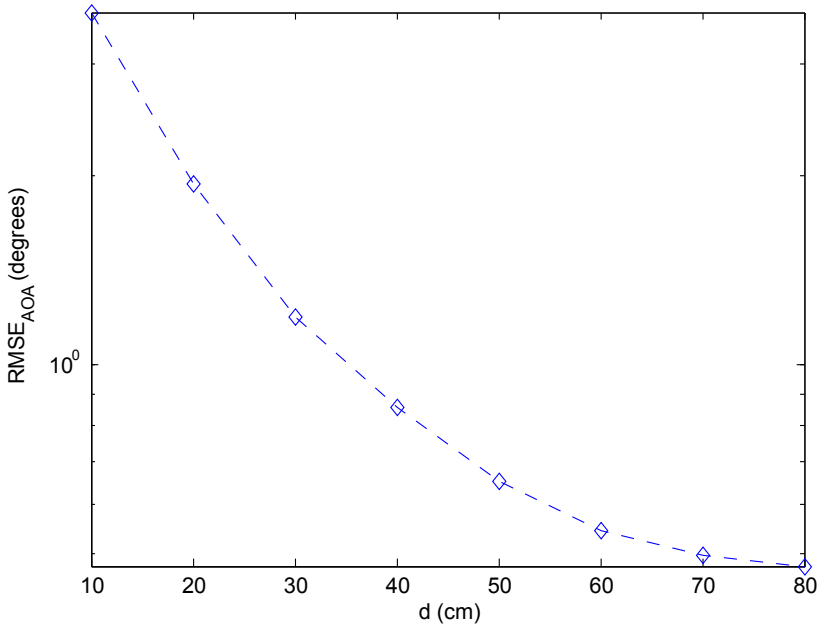

Fig. 4.7 RMSE of AOA estimates versus antenna spacing (Q=2, SNR=20dB).

Fig. 4.6 compares the AOA estimation performance of the proposed method with different values of the step size in the interpolation, i.e., $T_{\text{int}} = T_s/2$ and $T_s/4$. It can be seen that when the

resolution is finer (i.e., T_{int} is reduced), a better accuracy is obtained in the estimation. We note that the performance gap between the CRB and AOA estimates is reduced when the resolution is improved, although at higher SNR, the time resolution will ultimately limit the achievable performance. To show the effect on the achievable performance of the amount of overlap between the primary and secondary images, we consider three values for the parameter T_{rise}, namely, $2T_c/8$, $3T_c/8$ and $4T_c/8$. It is seen that when the overlap between the primary and secondary images is decreased, corresponding to a smaller value of T_{rise}, a small reduction is obtained in the CRB. However, the performance is still bounded by the resolution which, as we know, is decided by minimum search size. A small error in time domain will produce a transversal error of several degrees in angle.

Fig. 4.7 shows the AOA estimation performance of the proposed method for different values of the antenna spacing d between two adjacent antenna elements. As d increases, the RMSE of the AOA estimates decreases, as expected. In particular, a notable gain in performance is achieved when the spacing is increased from 10 to 60cm. Beyond this value, other effects such as the loss of spatial correlation over the primary path wavefront, would limit the estimation accuracy in practice.

The relationship between accuracy in spatial localization and TOA/AOA measurement is discussed in terms of the CRB in [11]. The CRB formulas provided in this chapter can be used to compute the improvement in localization accuracy that result from the smaller estimation RMSE with our proposed approach as compared to [50]. However, this requires the specification of an explicit operating configuration in terms of the number and position of the receivers, number of antennas, etc. Here, we shall limit our discussion of this issue to a simplified scenario, that is: single receiver equipped with Q=3 antennas, source node located along the array broadside ($\theta = 90^o$) at a distance of 4m from array center, and SNR=10dB. For this configuration, the RMSE values in Fig. 4.6 and 4.7 translate into a radial and tangential localization RMSE of 1.5cm and 6cm for the proposed method, versus 3cm and 17cm, respectively, for [50].

4.6.3 Directional image field

A limiting case of interest is that of a highly directional image field, in which all paths are arriving from almost the same angle, within a very narrow aperture. This could be the case in a LOS environment, where the emitting tag is surrounded by multiple reflecting objects in its immediate vicinity. In our simulations, to emulate this configuration, we simply set the mean angle of

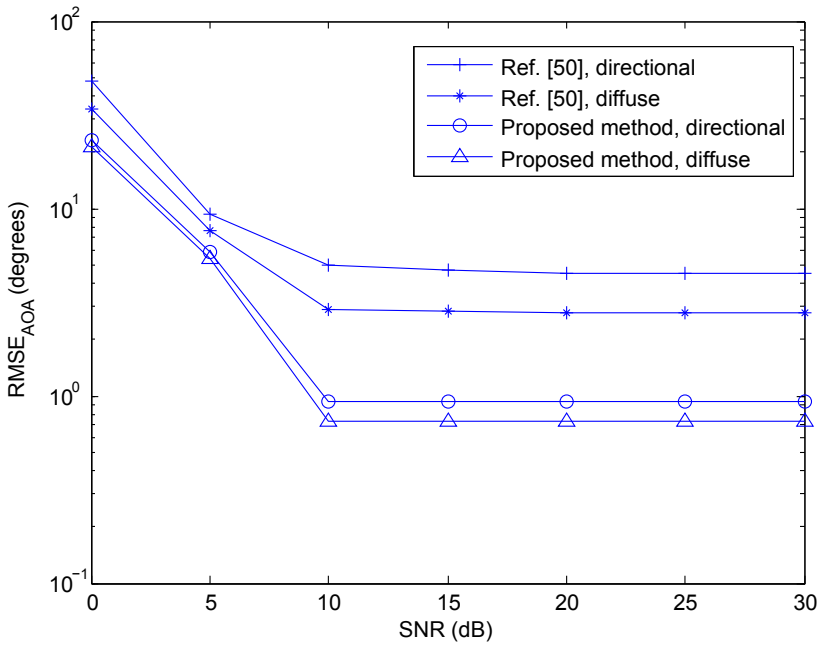

Fig. 4.8 RMSE of AOA estimates versus SNR for directional and diffuse secondary image fields (Q=2).

each cluster to the same value, i.e., 60°. As before, the AOA of each path follows a Laplacian distribution with standard deviation of 5°.

Fig. 4.8 shows the performance of both the proposed method and the one in [50] under this special condition of propagation. Comparing these results with those for the diffuse image field, we note that the AOA estimation accuracy of both methods is degraded. This is due to the fact that it is now more difficult to exploit the spatial information to separate the primary image path from the secondary ones. Nevertheless, in this more challenging scenario, the proposed estimator still outperforms the one in [50]. Similar conclusions can be drawn from the results of TOA estimation shown in Fig. 4.9.

4.7 Conclusion

In this chapter, we proposed a novel joint TOA and AOA estimator for dense multipath UWB environments. The proposed method consists of two steps: (1) preliminary estimation of the TOA and required *a priori* information; (2) joint estimation of the TOA and AOA by maximization of a new LLF which employs the preliminary estimates from the first step. The derivation of this LLF relies on a special formulation in which the superposition of pulse images from the

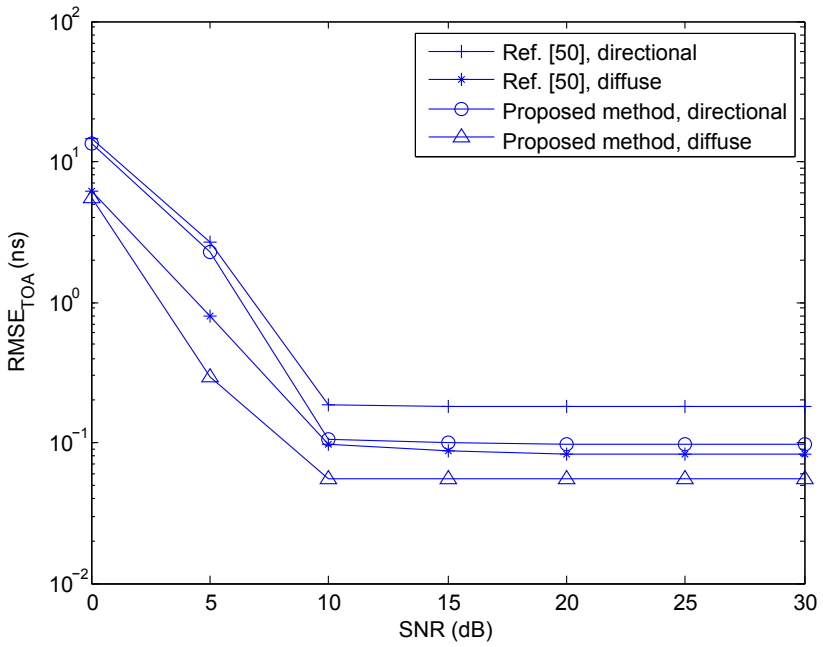

Fig. 4.9 RMSE of TOA estimates versus SNR for directional and diffuse secondary image fields (Q=2).

secondary paths is modeled as a Gaussian random process characterized by a wideband space-time correlation function which uses a gating mechanism to represent the onset of the secondary paths and also takes into account the APDP.

In simulation experiments based on multipath UWB channel models, our approach exhibits superior performance to that of a competing scheme from the recent literature. For a typical UWB environment based on the standard CM1 channel model and diffuse image field, with 2 antennas spaced 50cm apart, a SNR of 10dB and a sampling rate of 16GHz, the proposed joint estimator can provide an angular accuracy around 0.7° and a timing accuracy of less than 0.1 ns (corresponding to 3cm in range). Furthermore, the estimation accuracy improves with finer interpolation of the LLF as well as by increasing the number of antennas. The proposed estimator was also tested in an extreme case of highly directional noise field, where the obtained estimation accuracy remains competitive both for TOA and AOA parameters.

Chapter 5

Joint TOA and AOA Estimation in the presence of Multi-User Interference

In this chapter, the problem of joint estimation of the TOA and AOA in IR-UWB localization systems under the presence of MUI is modeled and discussed. A preliminary motivational discussion for this approach is provided in Section 5.1. In Section 5.2, we explain how the system model can be introduced in the multiuser context, by considering the MUI as background noise. The proposed joint estimation method is presented in detail in Section 5.3. Section 5.4 demonstrates the performance of the method using numerical experiments. Finally, in Section 5.5, a short conclusion is given.

5.1 Motivation

While most of the current works focus on TOA and AOA estimation in single-user systems, in the context of multiuser systems the parameter estimation for user of interest would be much more challenging due to the presence of interfering signals from undesired users. In [109], the authors derive a Ziv-Zakai lower bound for TOA estimation in the presence of MUI for single-path AWGN channels. However, the single path assumption severely limits the applicability of the derived results to realistic multipath channel scenarios. To the best of our knowledge, joint TOA/AOA estimation of IR-UWB signals in the presence of MUI has not been previously considered. Therefore, we attempt to fill this gap by proposing a practical low-complexity, yet highly accurate joint TOA/AOA estimator for a desired user whose signal is corrupted by MUI.

The work in the chapter is an extension of the the work presented in Chapter 4 to the multi-user case. The proposed method now includes 3 steps: (1) Time-alignment and averaging to reduce the effect of MUI; (2) preliminary TOA estimation based on energy detection followed by quadratic averaging; (3) joint TOA and AOA estimation using a LLF extended to consider the effect of MUI. The performance of the proposed method is demonstrated by numerical simulations.

5.2 Problem formulation

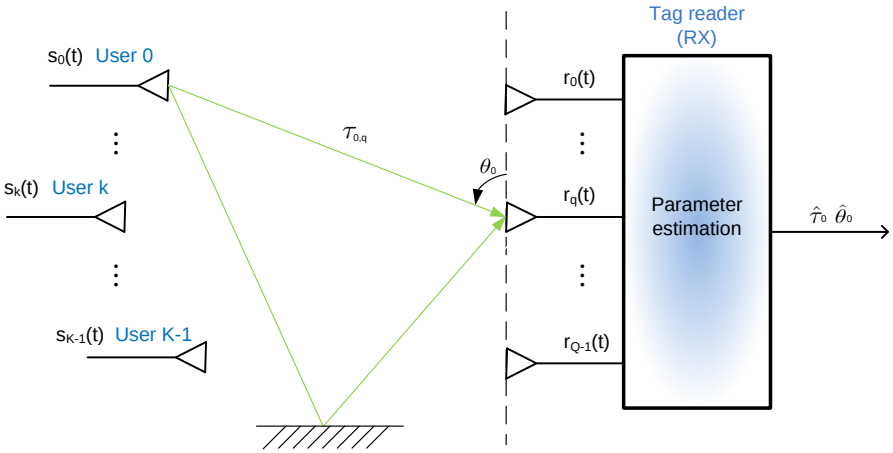

Fig. 5.1 Multiuser localization system.

We consider a multiuser localization system as depicted in Fig. 5.1, with K active users (tags) each equipped with a single antenna transmitter, and a receiver (tag reader) equipped with an antenna array. We are interested in the localization of a single user of interest, say user 0, in the presence of MUI.

The IR-UWB signal $s_k(t)$ transmitted by user $k \in \{0, \ldots, K-1\}$ is composed of N_{sym} consecutive symbols of duration T_{sym}, each of which consists of N_f frames of duration T_f (i.e., $N_{\text{sym}} = N_f T_f$) . Each frame is further divided into N_c chips of length T_c ($T_f = N_c T_c$) where each chip consists of N_p pulse periods of duration T_p ($T_c = N_p T_p$). Within the jth frame of the ith symbol, a single unit-energy pulse $w(t)$ of length T_p is transmitted in the chip identified by the unique TH code $c_k(j) \in \{0, \ldots, c_{\max}\}$ assigned to user k. In practice, the maximum code value satisfies $c_{\max} < N_c - 1$ to allow for guard intervals between successive frames and thereby avoid inter-frame interference (IFI) in the signal reconstruction process, as discussed later in Section

5.3. The pulse position is further modulated by a known training sequence $a_k(i) \in \{0, \ldots, N_p - 1\}$, adopted by user k for the purpose of ranging.

Hence, over the observation interval of length $T_o = N_{\text{sym}} T_{\text{sym}}$, the signal $s_k(t)$ is described by

$$s_k(t) = \sum_{i=0}^{N_{\text{sym}}-1} \sum_{j=0}^{N_f-1} \sqrt{E_k}\, w(t - iT_{\text{sym}} - jT_f - c_k(j)T_c - a_k(i)T_p) \tag{5.1}$$

where E_k is the transmitted energy per pulse of the kth user.

After multipath propagation, the transmitted signals are acquired at the tag reader by a ULA of $Q \geq 1$ identical antenna elements.[1] Under the far field assumption, the TOA at the qth antenna of user 0's signal through the primary path, i.e., the first path in a LOS environment, can be written as

$$\tau_{0,q} = \tau_0 + (q - \frac{Q-1}{2})\Delta\tau_0, \quad q \in \{0, \ldots, Q-1\} \tag{5.2}$$

where τ_0 denotes the TOA at the antenna array geometric center and $\Delta\tau_0$ is the TDOA between adjacent antennas. For a 2-dimensional (2D) geometry, the TDOA is related to the AOA, θ_0, by $\Delta\tau_0 = \frac{d}{c}\cos\theta_0$ with d denoting the inter-antenna spacing and c the speed of light.

The multipath channel between the kth user and qth antenna element is represented by $\mathcal{H}_{k,q}\{\cdot\}$, with $k \in \{0, ..., K-1\}$ and $q \in \{0, ..., Q-1\}$. The response to the emitted pulse $w(t)$ of the channel between user 0 and the qth receive antenna, is modeled as the superposition

$$\mathcal{H}_{0,q}\{w(t)\} = \eta_0(t - \tau_{0,q}) + \zeta_{0,q}(t) \tag{5.3}$$

where $\eta_0(t)$ denotes the pulse image arriving along the primary path and $\zeta_{0,q}(t)$ represents the total contribution of the images received along secondary paths, i.e., excluding the primary one. We model the primary pulse image $\eta_0(t)$ as a deterministic signal and the secondary pulse images $\{\zeta_{0,q}(t)\}_q$ as independent Gaussian random processes with zero mean and cross-correlation function

$$E[\zeta_{0,q}(t)\zeta_{0,q'}(u)] = g(t - \tau_{0,q})P(t)\delta_c(t-u)\delta_{q,q'}. \tag{5.4}$$

In (5.4), $P(t)$ is the average power delay profile (APDP) of the wireless channel, $\delta_c(t)$ is the Dirac delta function, $\delta_{qq'}$ is the Kronecker delta function, and $g(t)$ is a gating function used to characterize the onset of the secondary images (after the primary one) [102]. In this work, we set

[1] Here, a ULA is assumed for mathematical convenience, but generalization to other antenna configurations is straightforward.

$g(t) = u(t - T_p)$, where $u(t)$ denotes the standard unit step function.

The response to $w(t)$ of the channel between an interfering user k and the qth receive antenna, is modeled simply as

$$\mathcal{H}_{k,q}\{w(t)\} = \zeta_{k,q}(t), \quad k \in \{1, ..., K-1\} \tag{5.5}$$

where $\zeta_{k,q}(t)$ represents the total contribution of the pulse images received along all paths, i.e., including the primary one. We model $\{\zeta_{k,q}(t)\}_q$ as independent Gaussian random processes with zero mean and cross-correlation function

$$E[\zeta_{k,q}(t)\zeta_{k,q'}(u)] = P(t)\delta_c(t-u)\delta_{q,q'}. \tag{5.6}$$

Image components $\zeta_{k,q}(t)$ corresponding to different users (including $k = 0$) are assumed to be statistically independent.

The noisy IR-UWB signal at the output of the qth receive antenna can be expressed as

$$r_q(t) = \sum_{k=0}^{K-1} \mathcal{H}_{k,q}\{s_k(t)\} + n_q(t), \quad 0 \le t \le T_o \tag{5.7}$$

where $n_q(t)$ is an additive noise term modeled as a spatially and temporally white Gaussian process with zero mean and known power spectral density level σ_n^2. The noise terms $n_q(t)$ are assumed to be statistically independent from the pulse image component signal $\zeta_{k,q}(t)$.

The problem addressed in this letter can be stated as follows. Given the observation of the received antenna signals at the reader, $\{r_q(t) : 0 \le t \le T_o,\ q = 0, \ldots, Q-1\}$, we seek to jointly estimate the TOA and AOA parameters of the primary path, respectively τ_0 and θ_0 in (5.2) for user 0, in the presence of interference from the other users $k \in \{1, \ldots, K-1\}$.

5.3 Proposed method

The proposed method for joint parameter estimation consists of three main steps, as depicted in Fig. 5.2. These can be summarized as follows: (1) symbol and frame alignment followed by averaging to reduce MUI and white noise; (2) preliminary TOA estimation to narrow down the search range; (3) joint fine estimation of TOA and AOA based on an ML criterion. Note that the first step is very important in a multiuser environment; indeed, without a good MUI cancellation

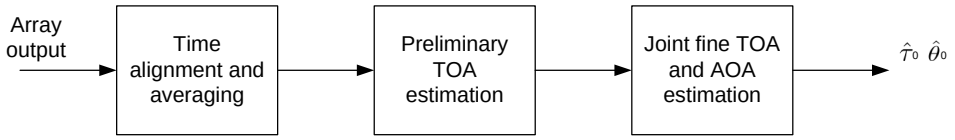

Fig. 5.2 Block diagram for proposed algorithm.

scheme, one cannot proceed to the next steps.

5.3.1 Frame alignment and averaging

First, the received signals $r_q(t)$ at each antenna $q \in \{0, \ldots, Q-1\}$ are time-aligned and averaged according to the TH code and training sequence of user 0, which are known at the receiver side, resulting into

$$x_q(t) = \frac{1}{N_{\text{sym}} N_f} \sum_{i=0}^{N_{\text{sym}}-1} \sum_{j=0}^{N_f-1} r_q(t + iT_{\text{sym}} + jT_f + c_0(j)T_c + a_0(i)T_p), \quad 0 \le t \le T_f. \tag{5.8}$$

As explained in Section II, each user k is assigned a unique TH identification code $c_k(j)$ and training sequence $a_k(i)$. These sequences are used in the PPM scheme (cf. (5.1)) to shift the transmitted pulses from user k at a specific location within each frame of each symbol. Since these sequences are different for each user k and have a random character, when we time-align the received signals within each frame of each symbol according to the TH code and training sequence of user 0, $c_0(j)$ and $a_0(i)$, pulses from the interfering users $k \in \{1, \ldots, K-1\}$ will fall at random locations within the different frames. Then, by averaging all time-aligned received data frames, the effects of the MUI as well as the additive noise can be reduced to a certain degree. In Fig. 5.3, we show the effects of time alignment and averaging. As can be seen in Fig. 5.3(a), before the time alignment and averaging, the received signal during a single frame is similar to a noise signal due to the MUI from other users and the background noise. After time alignment and averaging according to the TH code and training sequence of the desired user, we can detect the signal of interest as in Fig. 5.3(b). It is clear that in Fig. 5.3(b) both the MUI and white noise are greatly reduced after the operation. In Fig. 5.4, we show the result of alignment and averaging for each of four equipower users. It is clear that the process of decoupling the users' signals based on their unique codes is very effective: the actual TOA (indicated by a dotted line) is very close to the signal onset time for each user.

We note that while the training sequences $a_k(i)$ are usually chosen randomly, the selection of

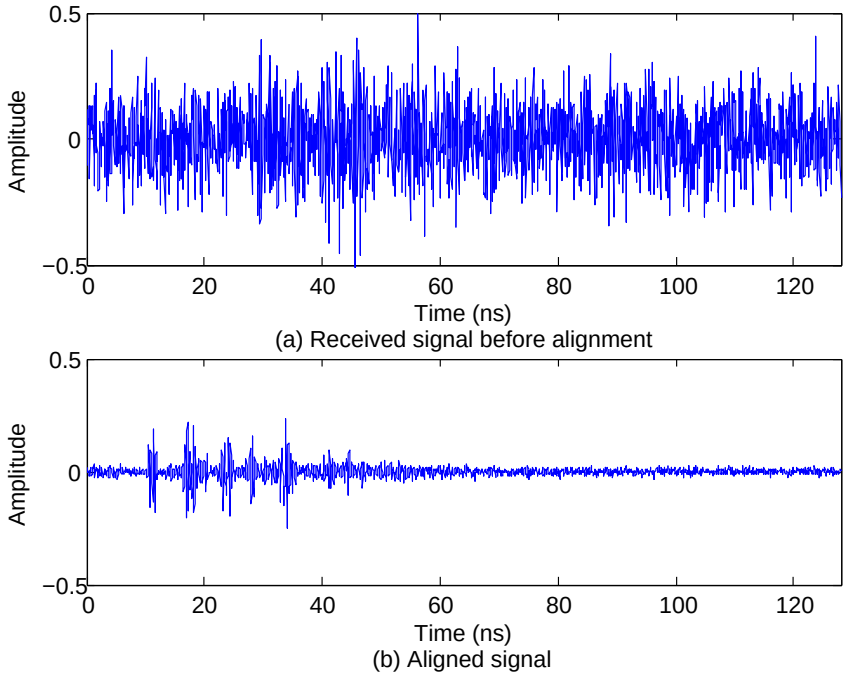

Fig. 5.3 Effects of alignment.

the TH codes $c_k(j)$ directly affects MUI mitigation. In this regard, the choice of a well-designed set of TH codes for the K users can greatly reduce the effect of MUI, and thus improve the final performance of the parameter estimation. Also, by increasing the values of N_{sym} and N_f, the more effective is the averaging operation (5.8) in reducing MUI and noise.

Upon substitution of (5.7) into (5.8), and making use of (5.1), (5.3) and (5.5), we can express the received signal at the output of the qth antenna, after averaging and time alignment for desired user 0, in the form

$$x_q(t) = \sqrt{E_0}[\eta_0(t - \tau_{0,q}) + \zeta_{0,q}(t)] + \bar{n}_q(t) + z_q(t) \tag{5.9}$$

where the MUI term $z_q(t)$ is given by

$$z_q(t) = \frac{1}{N_{\text{sym}} N_f} \sum_{k=1}^{K-1} \sum_{i=0}^{N_{\text{sym}}-1} \sum_{j=0}^{N_f-1} \sqrt{E_k}\zeta_{k,q}(t - \tau_{i,j,k}) \tag{5.10}$$

and $\bar{n}_q(t)$ is a zero-mean white Gaussian noise with power spectral density level $\bar{\sigma}_n^2 = \frac{1}{N_{\text{sym}} N_f}\sigma_n^2$.

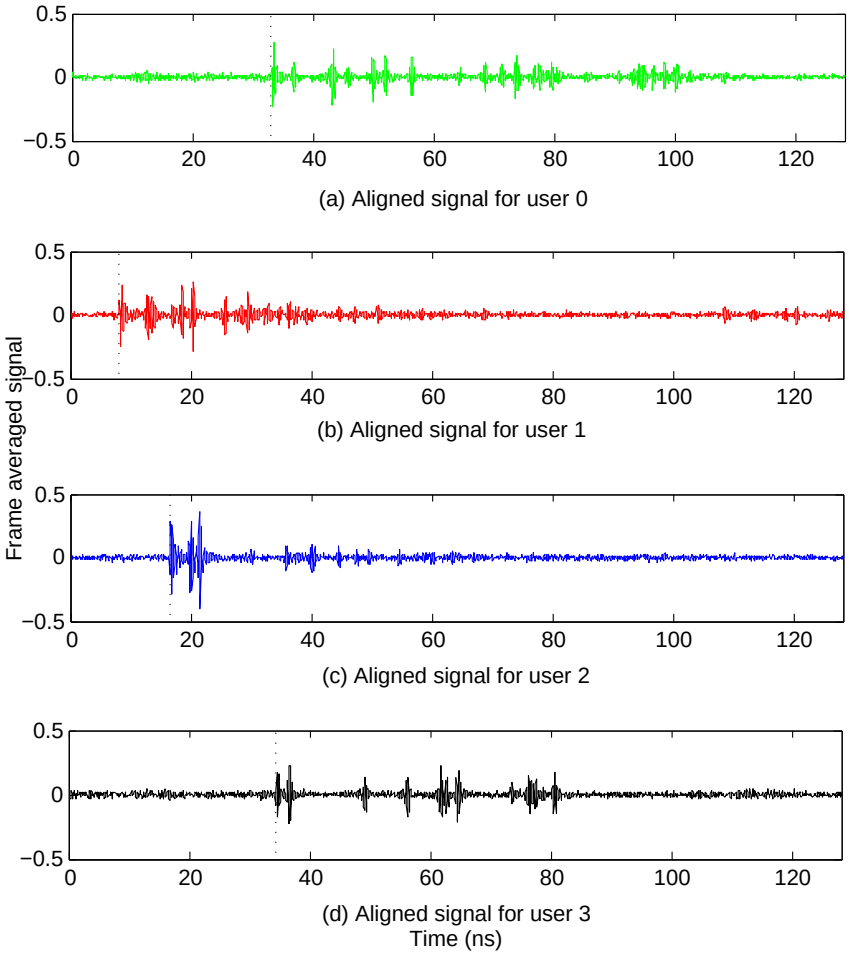

Fig. 5.4 Aligned signals of 4 different users.

The time shifts $\tau_{i,j,k}$ in (5.10), defined as

$$\tau_{i,j,k} = (c_k(j) - c_0(j))T_c + (a_k(i) - a_0(i))T_p \tag{5.11}$$

are bounded by $|\tau_{i,j,k}| \leq T_f - T_p$. According to (5.10), $z_q(t)$ is a sum of multipath contributions $\zeta_{k,q}(t)$ from the different users at the qth antenna, shifted by all possible values of the delays $\tau_{i,j,k}$, i.e., after proper alignment for desired user 0.

In this work, for simplicity, we model the summation of all the interference terms from other users $k \in \{1, \ldots, K-1\}$ in (5.10) as a Gaussian distributed random process with zero mean, but independent from the noise and desired signal. However, other assumptions such as the generalized Gaussian approximation or the Gaussian mixture [110, 111] could be also explored.

5.3.2 Preliminary TOA estimation

After obtaining the time-aligned array output signals $\{x_q(t)\}$, a preliminary TOA estimation is carried out for each antenna q. This step is used to alleviate the computational cost of the fine 2D search for joint TOA/AOA estimation in the final step. To this end, any current TOA estimation scheme for single antenna with satisfying performance can be adopted. In this work, we propose to use a TC method because of its simplicity and robustness. In fact, our experiments have shown that the use of more sophisticated methods, such as the DW-MESS in [26], do not necessarily lead to noticeable performance improvements in this preliminary estimation step.

In the TC method, the TOA estimate at the qth antenna is obtained as the smallest value of the time t, for which the instantaneous power of the time-aligned signal at the qth antenna output, $x_{0,q}^2(t)$, exceeds a given threshold $\lambda > 0$. That is:

$$\hat{\tau}_{0,q} = \min_{0<t<T_u} \{t \,|\, x_q^2(t) > \lambda\} \tag{5.12}$$

where T_u is the initial search range (i.e., uncertainty region) for the unknown TOA. The value of the threshold λ in (5.12) can be selected by considering the trade-off between the probabilities of false alarm and missed detection [32]. In this regard, we note that the noise variance now has to be adjusted to account for the presence of MUI, an aspect which will be elaborated upon in the next subsection.

Next, the preliminary TOA estimates $\hat{\tau}_{0,q}$ are averaged to obtain a single coarse estimate of the TOA at the array geometric center, i.e., τ_0 in (5.2). After comparing different approaches for the calculation of a mean TOA value, we found that the quadratic mean, given by

$$\hat{\tau}_0 = \frac{1}{Q}\Big(\sum_{q=0}^{Q-1} \hat{\tau}_{0,q}^2\Big)^{1/2} \tag{5.13}$$

achieved relatively better performance than other approaches. This can be explained by the fact that outlier estimates resulting from the application of (5.12) tend to be negatively biased (i.e., smaller than the true delay), and the quadratic mean gives a lesser weight to these smaller values.

5.3.3 Refined joint ML-based estimation

In this third and final step, the preliminary TOA estimate (5.13) is used to initiate a fine search for the TOA and AOA of user 0. This is achieved by maximizing a LLF based on the work in

[102], but extended to take into account the presence of MUI in the scenario considered here. The derivation of this extended LLF calls for the characterization of the random processes $\{x_q(t)\}$.

According to the Gaussian assumption for the combined pulse images $\{\zeta_{k,q}(t)\}$, the MUI interference $z_q(t)$ and the equivalent noise $\bar{n}(t)$, as well as their assumed mutual independence, it follows from (5.9)-(5.10) that $x_q(t)$ is also a Gaussian process, with non-zero mean

$$\mu_q(t) = E[x_q(t)] = \sqrt{E_0}\,\eta_0(t - \tau_{0,q}) \tag{5.14}$$

and covariance function

$$\begin{aligned} R_q(t,u) =& E[(x_q(t) - \mu_q(t))(x_q(u) - \mu_q(u))] \\ =& E_0 P(t) g(t - \tau_{0,q})\delta_c(t-u) + \bar{\sigma}_n^2 \delta_c(t-u) + R_{z_q}(t,u) \end{aligned} \tag{5.15}$$

where $R_{z_q}(t,u) = E[z_q(t)z_q(u)]$ is the auto-correlation of the MUI interference. To complete the characterization of $x_q(t)$ and proceed further with the application of the joint ML-based parameter estimation, we need a reasonable approximation for this auto-correlation, and especially the MUI power.

By making use of (5.10) along with the assumption that MUI contributions from different users k are independent, $R_{z_q}(t,u)$ can be further expanded as

$$R_{z_q}(t,u) = \frac{1}{(N_{\text{sym}}N_f)^2} \sum_{k=1}^{K-1} \sum_{(i,j)\in\mathcal{I}} \sum_{(i',j')\in\mathcal{I}} E_k P(t - \tau_{i,j,k})\delta_c(t - u - \tau_{i,j,k} + \tau_{i',j',k}) \tag{5.16}$$

where we define $\mathcal{I} = \{0,\ldots,N_{\text{sym}} - 1\} \times \{0,\ldots,N_f - 1\}$. At this point, we make an important simplification in (5.16): referring to the two inner summations over the index set $\mathcal{I}$, we shall neglect cross-terms for which $(i,j) \neq (i',j')$. Indeed, due to the random nature of the TH codes $c_k(j)$ and training sequences $a_k(i)$, the delays $\tau_{i,j,k}$ will be different with high probability for the different pairs of indices (i,j), and therefore the absolute delay differences $|\tau_{i,j,k} - \tau_{i',j',k}|$ far exceed T_p on average, which is the duration of the pulse waveform $w(t)$ in our model. Then, following the developments in [102], it can be shown that the corresponding peaks of the autocorrelation function $R_{x_q}(t,u)$ bring no useful information in the joint TOA/AOA estimation problem under

consideration, as their contributions to the LLF nearly vanish.[2] Consequently, we can write

$$R_{z_q}(t,u) \simeq (E_0 P(t) g(t-\tau_{0,q}) + \sigma_z^2(t) + \bar{\sigma}_n^2)\delta_c(t-u) \tag{5.17}$$

where $\sigma_z^2(t)$, the instantaneous power level of the MUI, is given by

$$\sigma_z^2(t) = \frac{1}{(N_{\text{sym}}N_f)^2} \sum_{k=1}^{K-1} \sum_{i=0}^{N_{\text{sym}}-1} \sum_{j=0}^{N_f-1} E_k P(t-\tau_{i,j,k}). \tag{5.18}$$

The time delay variables $\tau_{i,j,k}$ in (5.15) account for the asynchronism between the different users, frames and symbols. Due to the random nature of the TH codes $c_k(j)$ and training sequences $a_k(i)$, it is reasonable to model the time differences $\tau_{i,j,k}$ in (5.15) as independent realizations of a random variable υ with PDF $f(\upsilon)$. Hence, since the value of the product $N_{\text{sym}}N_f$ is typically large under the proposed scenario in this work, the law of large numbers can be invoked to obtain the following approximation

$$\frac{1}{N_{\text{sym}}N_f} \sum_{i=0}^{N_{\text{sym}}-1} \sum_{j=0}^{N_f-1} P(t-\tau_{i,j,k}) \simeq E_\upsilon[P(t-\upsilon)] = \int_{-T_f}^{T_f} P(t-\upsilon) f(\upsilon) d\upsilon. \tag{5.19}$$

Using (5.18) in (5.15) we finally obtain

$$\sigma_z^2(t) = \frac{\bar{P}(t)}{N_{\text{sym}}N_f} \sum_{k=1}^{K-1} E_k \tag{5.20}$$

where we define $\bar{P}(t) = \int_{-T_f}^{T_f} P(t-\upsilon) f(\upsilon) d\upsilon$.

Let $\mathbf{x} = \{x_q(t) : t \in [0, T_f],\ q \in \{0, \ldots, Q-1\}\}$ represent the complete set of observed data, after time-alignment for user 0 and frame averaging, and define $\boldsymbol{\phi} = [\tau_0, \theta_0]$ as the vector of the unknown parameters being estimated. By proceeding as in [102], a closed form expression for the LLF of $\mathbf{x}$ given the value of the unknown parameter vector $\boldsymbol{\phi}$, can be derived. This involves passing to discrete-time by uniformly sampling the signals $x_q(t)$ at the Nyquist rate, making use of the multi-dimensional Gaussian PDF expression for the resulting vector of time samples, inverting the associated data covariance matrix, and finally converting back to continuous-time.

[2] These peaks contribute additional terms of the type $\int_0^{T_f} \alpha(t)\bar{x}_q(t)\bar{x}_q(t-\delta\tau)dt$ to (21), where $\alpha(t)$ is a weighting function, $\bar{x}_q(t) = x_q(t) - \mu_q(t;\tau_{0,q})$, and $|\delta\tau| > T_p$, to the LLF in (21). For such values of $\delta\tau$, this integral is nearly zero as there remains no useful correlation between $x_q(t)$ and $x_q(t-\delta\tau)$.

After these operations, the desired LLF is obtained as

$$\ln \Lambda(\mathbf{x}, \phi) = -\frac{1}{2} \sum_{q=0}^{Q-1} \left(l_{1,q}(\mathbf{x}; \phi) + l_2(\phi) \right) \tag{5.21}$$

where the data-dependent terms $l_{1,q}(\mathbf{x}; \phi)$ are given by

$$l_{1,q}(\mathbf{x}; \phi) = \int_0^{T_f} \frac{\left(x_q(t) - \mu_q(t) \right)^2}{E_0 P(t) g(t - \tau_{0,q}) + \sigma_z^2(t) + \bar{\sigma}_n^2} dt. \tag{5.22}$$

with $\tau_{0,q}$ as defined in (5.2) in terms of the TOA τ_0 and AOA θ_0. During the calculation of $l_2(\phi)$, we found that its final value is almost constant for different choices of τ_0 and θ_0, as long as the channel delay spread is smaller than T_f.

The numerical evaluation of (5.21) requires the knowledge of $\mu_q(t)$ in (5.14), which in turn depends on $\eta_0(t)$, i.e., the received pulse image from user 0 along the primary path. In practice, the pulse shape $\eta_0(t)$ is unknown and must be estimated from the observed data along with the desired parameters. Here, we proceed as in [102] and estimate $\mu_q(t)$ simply as a time-shifted version of $x_0(t)$ over an interval of duration T_p. That is, for each candidate value of the unknown TOA $\tau_{0,q}$ in (5.2), we replace the unknown pulse shape $\sqrt{E_0}\hat{\eta}(t)$ in (5.21) by $x_0(t + \tau_{0,q})$ when $0 \le t \le T_p$ and by 0 otherwise. In addition, the evaluation of (5.21) also requires $\sigma_z^2(t)$, which is given by (5.18). In practice, if the transmitted powers E_k are unknown, we can approximate $E_k P(t - \tau_{i,j,k})$ in (5.18) by squaring the signal obtained through alignment and averaging using the TH code and training sequence of the kth user.

Finally, the joint ML estimator is obtained by maximizing the LLF using a two-dimensional fine search, as in:

$$\hat{\phi}_{\mathrm{ML}} = \arg \min_{\phi \in \mathcal{P}} \left(\sum_{q=0}^{Q-1} l_{1,q}(\mathbf{x}; \phi) \right) \tag{5.23}$$

where $\mathcal{P}$ denotes the parameter space over which the search is performed. In practice, the search range for τ_0 and θ_0 is restricted by practical considerations. That is, the search for τ_0 is limited to a few chip intervals around the preliminary estimate $\hat{\tau}_0$ in (5.13), while the search for θ_0 is limited by the antenna distance d and the sampling resolution of the available discrete-time signals.

5.4 Numerical results

To demonstrate the validity of the proposed method for joint TOA/AOA estimation in the presence of multiuser interference, computer simulations under realistic operating conditions are carried out and the corresponding results are discussed in this Section.

5.4.1 Methodology

We consider a $K = 4$ user system, with user 0 being the desired user. The main timing system parameters are chosen as follows: $N_{\text{sym}} = 32$, $T_{\text{sym}} = 512$ns, $N_f = 4$, $T_f = 128$ns, $T_c = 4$ns and $T_p = 0.5$ns. An optimal TH code set from [110, 111] is adopted in the simulations, specifically: for the desired user $c_0(j) = [3, 2, 3, 6]$, and for the interfering users $c_1(j) = [7, 9, 1, 7]$, $c_2(j) = [2, 0, 4, 2]$ and $c_3(j) = [9, 5, 7, 1]$, where j runs from 0 to 3. The training sequences are created randomly for each user, i.e., the values of $a_k(i)$ are generated as independent and uniformly distributed random variables from the discrete set $\{0, \ldots, 7\}$. The TH code and training sequences are used to construct the IR-UWB pulse trains of the individual users by repetition of a properly shifted Gaussian doublet pulse, with effective bandwidth $B = 4$GHz.

The UWB radio channels are generated using the CM1 channel model (i.e., residential, line of sight) in the IEEE 802.15.4a standard [6] with a delay spread of 80ns. Spatial dependence is incorporated into the propagation model according to the approach in [107, 108]. That is, the AOA of each path follows a Laplacian distribution with a cluster mean value uniformly distributed over the range $[45^o, 135^o]$ and a standard deviation of 5° for each cluster. The receiver is equipped with a ULA of $Q = 3$ identical antenna elements, with inter-element spacing $d = 50$cm, whose outputs are sampled at the rate $F_s = 16$GHz.

The joint TOA/AOA estimation is realized by implementing the three-step approach presented in Section III, with the following specifications. In the second step, the initial search range is set to $T_u = 48$ns and the preliminary estimate $\hat{\tau}_0$ in (5.13) is rounded to the nearest available time sample, i.e., multiple of $T_s = 1/F_s = 0.0625$ns. In the third step, the gating function $g(t)$ used in the LLF (5.22) is simply set as a unit step function with delay T_p. The search range for the fine estimation (5.23), which is limited by the sampling period T_s, consists of a regular grid of 17×55 points in the $(\tau_0, \Delta\tau_0)$ plane with center at $(\hat{\tau}_0, 0)$. The performance of the proposed estimator is measured using the root-mean-square error (RMSE), evaluated by averaging over 500 runs using independent channels and additive noise realizations.

5.4.2 Results and discussion

Fig. 5.5 shows the performance of the preliminary TOA estimation with respect to the number of symbols N_{sym}, with the SNR $= N_f E_0/\sigma_n^2$ of the desired user fixed at 15dB. Here, the RMSE is also compared for different numbers of interfering users, with same power as the desired one, i.e., $E_k = E_0$. When the number of interfering users is reduced from $K - 1 = 3$ to 0, the RMSE of the preliminary TOA estimates decreases as expected. We also note that the estimation performance becomes stable when N_{sym} reaches a value of 16, beyond which only marginal improvements are obtained.

Results of the fine TOA estimation using the proposed joint estimator are presented in Fig. 5.6 as a function of SNR. In this case, $N_{\text{sym}} = 32$, $K = 4$, and the results are compared for different values of the interference power, i.e., $E_k = \rho E_0$ where $\rho \in \{0, 0.5, 1, 1.5\}$. It is clear that the fine TOA estimation from the joint ML estimation step achieves fairly high accuracy (mostly less than 0.1 ns). In particular, comparing with the corresponding results in Fig. 5.5, we find that the RMSE of the TOA estimation drops from 0.12ns following the preliminary estimation, to about 0.08ns after the fine search, for a net additional gain of about 3.5dB.

Fig. 5.7 compares the AOA estimation performance of the proposed method with different MUI power levels. As in Fig. 5.5, the energies of the interfering users are set to larger, equal or smaller than the energy of the desired user, accordingly. It can be seen that the AOA estimation accuracy improves as the interference degrades. At SNR of 10 dB, the attainable RMSE value is under 2 degrees for all the cases. When the interference user energy is 1.5 times that of the desired user, the performance of the AOA estimation slightly degrades. This is reasonable because in this case, the total energy level of the additive MUI amounts for 4.5 times (13dB) that of the desired user in this worst case scenario.

5.5 Conclusions

In this chapter, we proposed a new three-step method for the joint TOA/AOA estimation of a desired IR-UWB signal with an antenna array receiver, in the presence of multiuser interference. In the first step, the received signals which consist of the linear superposition of all the user transmissions, are time-aligned according to the unique TH code and training sequence of the desired user, which greatly reduces the power of unwanted MUI and additive noise. In the second step, a preliminary TOA estimate is obtained via energy detection followed by non-linear averaging.

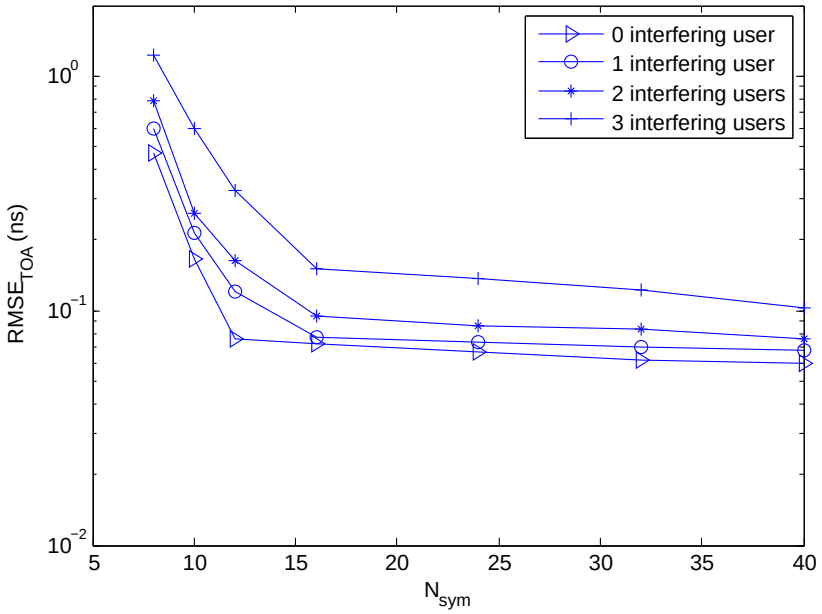

Fig. 5.5 RMSE of preliminary TOA estimates versus N_{sym} ($E_k = E_0$, SNR= 15dB).

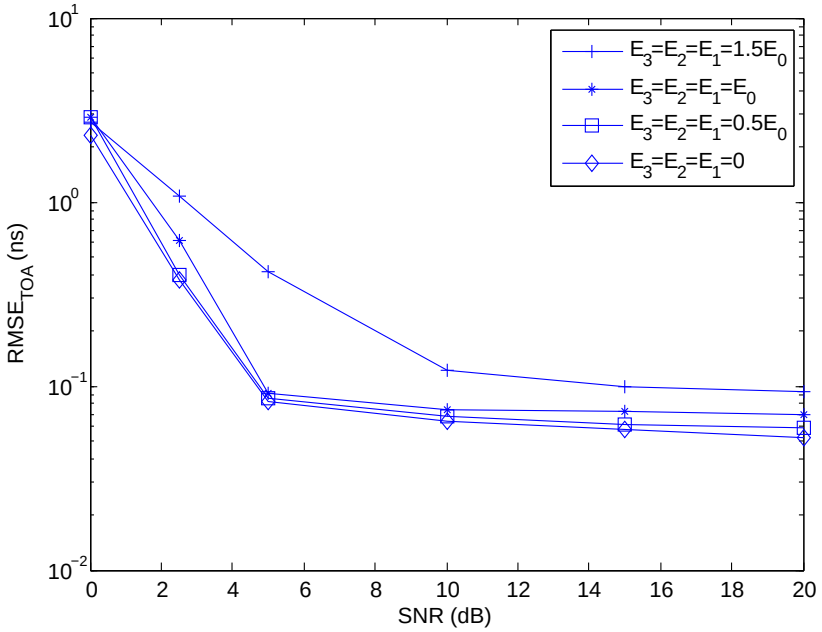

Fig. 5.6 RMSE of TOA estimates versus SNR for different MUI power ($N_{\text{sym}} = 32$, $K = 4$).

In the third step, the final joint TOA/AOA estimation is achieved by maximization of a recently proposed LLF through a fine 2D search over a smaller region delimited by the preliminary TOA. This LLF, which relies on a special formulation of the desired user signal model that incorporates

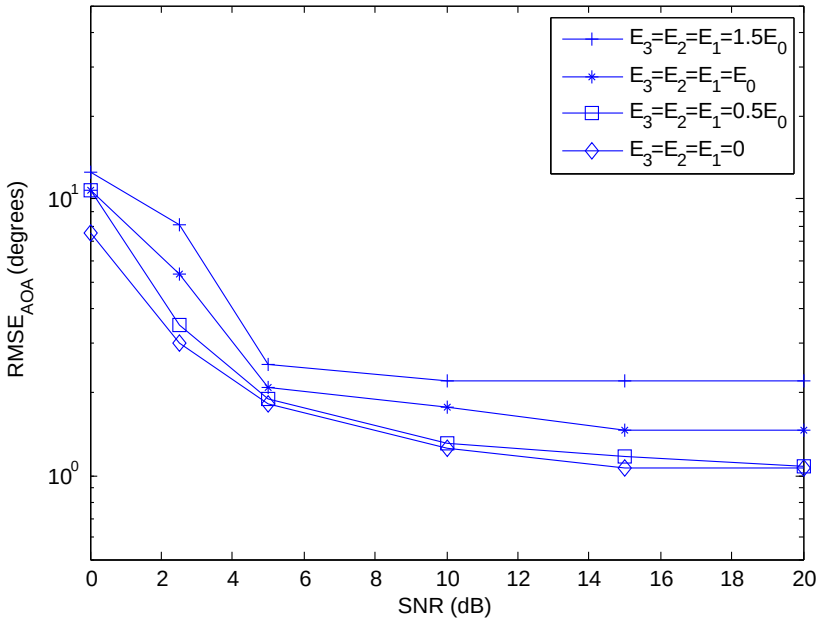

Fig. 5.7 RMSE of AOA estimates versus SNR for different MUI power ($N_{\text{sym}} = 32$, $K = 4$).

a gating mechanism along with the APDP [102], is further extended to incorporate the effect of MUI. Finally, simulation experiments are carried out that demonstrate the effectiveness of the proposed method.

Chapter 6

Conclusions and Future Works

6.1 Summary and conclusions

In this thesis, we designed and studied the properties of new low-complexity, yet accurate algorithms for parameter estimation in IR-UWB systems, and this for both single user and multiple users scenarios. The estimated parameters include the TOA and the AOA, which are the most commonly employed parameters in UWB localization systems, as well as the APDP which provides important information about the UWB channel.

In the first chapter, we began by introducing the UWB technology and its applications from a high-level perspective. This was followed by a literature review of different parameter estimation methods with special emphasis on TOA and AOA, both for single user and multi-user applications. The main objectives and research contributions of the thesis were then stated.

In the second chapter, the main focus was on presenting the necessary background information on parameter estimation for IR-UWB localization systems. We first reviewed IR-UWB signaling principles, including the choice of pulses, time-domain modulation and multiple-access schemes. This was followed by a detailed description of the UWB channel model proposed along with the IEEE 802.15.04a standard and based on the modified SV model. Since the statistical parameters of these models were obtained from practical measurements, they are favored by many researchers and they were employed in the later simulations. The various geometrical approaches for the localization of a UWB emitter based on the estimation of physical parameters such as RSS, TOA, TDOA, AOA and hybrid combination thereof where then introduced. Finally, selected methods from the literature for TOA and AOA estimation were reviewed.

Starting with the third chapter, we gave the detailed explanations of our own proposed meth-

ods, which in each case were thoroughly evaluated and compared to other algorithms of the same category as well as the CRB. In Chapter 3, we mainly studied the TOA estimation problem under the single user, single antenna scenario. In particular, a new method for jointly estimating the TOA and the APDP was developed that only required a sub-Nyquist sampling rate. While there have been many works in this area during the past years, we were still interested in improving the sub-Nyquist ML based approach since it has the potential to achieve the best performance under the constraint of low sampling rate [22]. As we know, traditionally, the nuisance parameters related to channel information are either estimated simultaneously with the TOA, which adds a heavy burden on the algorithm, or simply assumed as available *a priori* knowledge. Noting that neither of these approaches are practical for a real implementation, we decided to explore the use of channel information in terms of APDP at low cost, by using some recently proposed channel models. We assumed a multi-cluster parametric model for the APDP and estimated its parameters via log-domain LS fitting; the estimated APDP was then used in conjunction with a ML criterion to obtain the TOA estimate. By exploiting these parameterized APDP models, the computation complexity now became practical due to the largely reduced number of unknowns. Meanwhile, to further alleviate the computational burden, all the operations were performed at sub-Nyquist rate. Consequently, we were finally able to achieve an accurate TOA estimation performance at a low and practical cost. In addition, the effectiveness of estimated APDP was further verified by applying it to earlier TOA estimation methods which also need to employ the APDP to fulfill the final TOA estimation.

In Chapter 4, we studied the joint estimation problem of the TOA and AOA for a single user assuming this time that an antenna array is employed at the receiver to enable the AOA estimation. We focused on developing a joint ML-based estimator by exploring the spatial as well as the channel information, still targeting a low computation cost. Unlike previous works, we brought in an original formulation of the channel in which the impulse response is separated into two parts: the primary pulse image and the superposition of images from secondary paths. The primary pulse image was considered as deterministic while the secondary path images were modeled as a Gaussian random process, whose second order statistical properties were characterized by a wideband space-time correlation function. Taking advantage of this model, together with spatial information, a novel form of the LLF was derived which incorporates a special gating mechanism to represent the onset of the secondary paths. The LLF depends on both nuisance parameters (APDP and primary pulse image) as well as the geometrical parameters to be estimated (TOA and AOA). Therefore, if we can solve for the nuisance parameters, a simplified 2D search can be

carried out to determine the unknown TOA and AOA. To implement this approach, we proposed a specific method in two steps, that is: (1) a preliminary stage which involves the coarse estimation of the TOA using energy-based threshold crossing, the APDP using log-domain LS fitting (which can be easily obtained based on our previous work in Chapter 3) and the primary pulse image using one of the received signals; (2) joint TOA refinement and AOA estimation by local 2D maximization of a LLF which employs the preliminary estimates from the first step. A new CRB based on the estimation variance of unbiased estimators of the TOA and AOA was derived based on this LLF. Finally, according to the simulation results, the proposed joint estimator provided a better performance than an existing benchmark algorithm by taking better advantage of the channel as well as the spatial information.

As an extension of these contributions, Chapter 5 considered the problem of joint TOA and AOA estimation under a multiple users scenario. Unlike the single user case, where we can operate directly on the received signals, here we need to firstly isolate the signal of desired user out of the received signal which bears much resemblance to noise due to the MUI. In our proposed method, this task was fulfilled by making use of the TH code of the desired user, which is available at the receiver for multi-user access, as well as the unique training sequence assigned to this user. Specifically, the TH code and training sequence were used in a first step to time-align and average the sequence of time coded pulses emitted by the desired user. After reducing the effects of MUI and noise in this manner, the remaining steps were similar to those of the single user. Therefore, in a second step, preliminary TOA estimation based on energy detection followed by quadratic averaging were applied and then, in the third and final step, joint TOA and AOA estimation were performed by maximizing a LLF. The latter was based on our previous work in Chapter 4, but extended to consider the effect of MUI as an additive Gaussian noise term with calculated power level. The performance of the proposed method in estimating TOA and AOA was demonstrated through numerical simulations for a multi-user scenario where the near-far problem was accounted for.

In conclusion, several new parameter estimation methods for the estimation of the TOA and AOA parameters in IR-UWB localization systems were proposed and thoroughly investigated in this thesis. We paid special attention to exploring and modeling the internal characteristics of the UWB radio channel, especially the APDP and the spatial correlation properties, in order to achieve a fine estimation of the geometric localization parameters. We employed the channel statistics in a much simpler way, instead of using the full channel information (i.e., the channel impulse response) as in previous work, which would have greatly increased the overall cost and

complexity of the estimation algorithms. Our work showed that by properly exploiting a limited amount of information about the channel, in the form of second order statistical properties, it is still possible to improve the accuracy of the TOA and AOA estimation without excessively increasing the computational complexity of the required processing. Comprehensive studies as well as simulation experiments were conducted, which demonstrated the effectiveness of the proposed methods.

6.2 Future work

The following topics have been identified during the development of this thesis, which deserve particular attention for future research:

1. *Experimental validation:* Issues regarding practical hardware implementation of the proposed estimators can be further studied, and the interpolation structure can be included as well. While the experiments in this thesis are based on numerical simulations, it is worth examining and verifying the proposed methods by means of a real experimental set up using off-the-shelf IR-UWB tags and special purpose tag readers (receivers) along with fast DSP processors for off-line data processing and evaluation. For example, real measurements can be conducted in an indoor open hall where several tags transmitting IR-UWB pulses can be placed at different locations, whereas a tag reader employing a ULA array with adjustable distance between antenna elements is fixed in a peripheral location. The receiver should incorporate an assembly board of cascaded components, including antennas, low-noise amplifier, fast A/D for sampling and data processing unit for parameter estimation. In this respect it would be of interest to determine the effect of the A/D resolution (i.e., number of quantization bits) on the achievable estimation performance of the proposed estimator.

2. *Directional image field:* In terms of joint estimation, a more sophisticated spatial model could be developed that more accurately represents the directional image fields encountered in practical applications. We have been able to observe that the performance of the proposed as well as other existing estimation methods degrades notably in the presence of a directional secondary image field, since the current signal model on which the estimators are based is not designed for such extreme cases. As an alternative, we could consider the necessary changes in the problem formulation part for the special case of a directional

image field as it is believed that a more accurate, although more complex model would bring benefit under the same framework. To be specific, this can be done by modifying the space-time correlation function in (4.5), and especially the spatial component $\varrho(q, q')$. Currently, there is no clear description for the space-time correlation of the channel response at different antenna elements, especially for the extreme case of a very directional image field. It is therefore worthwhile to develop new functional relations which can embody the characteristics of such highly directional paths. Then, based on this generalized model of the space-time correlation, a new (hopefully tractable) form of the LLF can be obtained and the associated CRB derived as well. With the corresponding changes in the signal model according to the spatial correlation properties of the radio environment, it is hoped that a better performance in TOA and AOA estimation could be obtained with the newly derived ML estimator.

3. *Joint multi-user estimation:* Finally, as mentioned previously, joint TOA and AOA estimation under MUI is not well developed in the literature and we believe it is worth putting more effort along this avenue. In our current work, we considered this joint estimation problem for one specific user under different power levels of MUI. This can be extended to a more sophisticated scenario where we attempt to perform joint multi-user parameter estimation simultaneously. In fact, joint estimation of localization parameters of different users may lead to a performance gain, since it can benefit from a better exploitation of the incorporated signal structure. However, these benefits are likely to come at the expense of many practical complications. For example, a joint multi-user parameter estimation implies the use of a more complex form of the LLF, which would require much further work for its derivation as well as for its implementation. In addition, the joint multi-user estimation would require a high-dimensional multi-dimensional search in the final joint optimization step. To alleviate the computation cost, it would be necessary to develop simplified or more efficient search techniques, such as the ones used in current sequential interference cancelation techniques. Of related interest is the derivation of the CRB on TOA and AOA parameters for the joint multi-user estimation problems. Finally, the individual estimation accuracy of the parameter estimates obtained with the joint multi-user approach would need to be compared to the current work under the same system set up, to determine whether or not this new formalism can bring sustainable performance gains.

References

[1] Federal Communication Commission, "First Report and Order," *FCC 02-48*, Feb. 2002.

[2] J. Foerster, "Channel modeling sub committee report final," *IEEE P802.15 Wireless Personal Area Networks P802.15-02/490r1-SG3a*, Feb. 2003.

[3] J. Balakrishnan, A. Batra, and A. Dabak, "A multi-band OFDM system for UWB communication," in *Proc. IEEE Int. Conf. Ultra Wideband Systems and Technologies*, Reston, USA, Nov. 2003, pp. 354–358.

[4] R. Fisher, R. Kohno, H. Ogawa, H. Zhang, K. Takizawa, M. M. Laughlin, and M. Welborn, "DS-UWB physical layer submission to 802.15 task group 3a," in *IEEE P802.15-04/0137r5*, July 2004.

[5] S. Hara and R. Prasad., "Overview of multicarrier CDMA," *IEEE Communications Mag.*, vol. 35, no. 12, pp. 126–133, Feb. 1997.

[6] A. Molisch, K. Balakrishnan, C. Chong, S. Emami, A. Fort, J. Karedal, J. Kunisch, H. Schantz, U. Schuster, and K. Siwiak, "IEEE 802.15.4a channel model-final report," *IEEE 802.15 WPAN Low Rate Alternative PHY Task Group 4a (TG4a)*, Nov. 2004.

[7] P. Zhang and H. Liu, "An ultra-wide band system with chirp spread spectrum transmission technique," in *Proc. Int. Conf. ITS Telecommun.*, Chengdu, China, Jun. 2006, pp. 294–297.

[8] *Part 15.4: Wireless Medium Access Control (MAC) and Physical Layer (PHY) Specifications for Low-rate Wireless Pesonal Area Networks (LRWPANs)*, IEEE P802.15.4a/D4 (Amendment of IEEE Std 802.15.4) Std., July 2006.

[9] G. Shirazi and L. Lampe, "Lifetime maximization in UWB sensor networks for event detection," *IEEE Trans. Signal Processing*, vol. 59, no. 9, pp. 4411–4423, Sept. 2011.

[10] J. Taylor, *Ultra-wideband Radar Technology*. CRC Press, 2001.

[11] S. Gezici, Z. Tian, G. B. Biannakis, H. Kobayashi, A. F. Molisch, H. V. Poor, and Z. Sahinoglu, "Localization via ultra-wideband radios: A look at positioning aspects for

future sensor networks," *IEEE Signal Processing Magazine*, vol. 22, no. 4, pp. 70–84, July 2005.

[12] G. Zhang and S. Rao, "Position localization with impulse ultra wide band," in *Proc. IEEE Int. Conf. Wireless Commun. and Applied Computational Electromagnetics*, Hawaii, USA, April 2005, pp. 17–22.

[13] M. Tuchler, V. Schwarz, and A. Huber, "Location accuracy of an UWB localization system in a multi-path environment," in *Proc. IEEE Int. Conf. Ultra-Wideband*, Sept. 2005, pp. 414–419.

[14] D. Jourdan, D. Dardari, and M. Win, "Position error bound for uwb localization in dense cluttered environments," *IEEE Trans. Aerospace and Electronic Systems*, vol. 44, no. 2, pp. 613–628, 2008.

[15] S. Gezici and H. V. Poor, "Position estimation via ultra wideband signals," in *Proc. IEEE*, vol. 97, pp. 386–403, Feb. 2009.

[16] D. Dardari and M. Win, "Threshold-based time-of-arrival estimators in UWB dense multipath channels," in *Proc. IEEE Int. Conf. Commun.*, June 2006, pp. 4723–4728.

[17] Y. Qi, H. Kobayashi, and H. Suda, "On time-of-arrival positioning in a multipath environment," *IEEE Trans. Vehicular Technology*, vol. 55, no. 5, pp. 1516–1526, Sept. 2006.

[18] U. Schuster and H. Bolcskei, "Ultra wideband channel modeling on the basis of information-theoretic criteria," *IEEE Trans. Wireless Commun.*, vol. 6, no. 7, pp. 2464–2475, July 2007.

[19] C. Carbonelli and U. Mitra, "Clustered channel estimation for UWB multiple antenna systems," *IEEE Trans. Wireless Commun.*, vol. 6, no. 3, pp. 970–981, Mar. 2007.

[20] H. Wymeersch, S. Marano, W. Gifford, and M. Win, "A machine learning approach to ranging error mitigation for UWB localization," *IEEE Trans. Commun.*, vol. 60, no. 6, pp. 1719–1728, Jun. 2012.

[21] M. Win and R. Scholtz, "Characterization of ultra-wide bandwidth wireless indoor channels: a communication-theoretic view," *IEEE J. Sel. Areas Commun.*, vol. 20, no. 9, pp. 1613–1627, Dec. 2002.

[22] H. Poor, *An Introduction to Signal Detection and Estimation*. New York: Springer-Verlag, 1994.

[23] D. Dardari, A. Conti, U. Ferner, A. Giorgetti, and M. Win, "Ranging with ultrawide bandwidth signals in multipath environments," in *Proc. IEEE*, vol. 97, no. 2, pp. 404–426, Feb. 2009.

[24] J. Lee and R. Scholtz, "Ranging in a dense multipath environment using an UWB radio link," *IEEE J. Sel. Areas Commun.*, vol. 20, no. 9, pp. 1677–1683, Dec. 2002.

[25] A. Rabbachin, I. Oppermann, and B. Denis, "GML TOA estimation based on low complexity UWB energy detection," in *Proc. IEEE Int. Symp. Personal, Indoor and Mobile Radio Communications*, Sept. 2006, 5 pages.

[26] I. Guvenc, S. Gezici, and Z. Sahinoglu, "Ultra-wideband range estimation: theoretical limits and practical algorithms," in *Proc. IEEE Int. Conf. Ultra-Wideband*, Sept. 2008, pp. 93–96.

[27] H. Luecken, C. Steiner, and A. Wittneben, "ML timing estimation for generalized UWB-IR energy detection receivers," in *Proc. IEEE Int. Conf. on Ultra-Wideband*, Sept. 2009, pp. 829–833.

[28] O. Bialer, D. Raphaeli, and A. Weiss, "Efficient time of arrival estimation algorithm achieving maximum likelihood performance in dense multipath," *IEEE Trans. Signal Processing*, vol. 60, no. 3, pp. 1241–1252, Mar. 2012.

[29] A. D'Amico, U. Mengali, and L. Taponecco, "Energy-based TOA estimation," *IEEE Trans. Wireless Commun.*, vol. 7, no. 3, p. 3, 2008.

[30] W. Feng, T. Zhi, and B. M. Sadler, "Weighted energy detection for noncoherent ultra-wideband receiver design," *IEEE Trans. Wireless Commun.*, vol. 10, no. 2, pp. 710–720, 2011.

[31] W. Liu, H. Ding, X. Huang, and Z. Liu, "TOA estimation in IR UWB ranging with energy detection receiver using received signal characteristics," *IEEE Commun. Lett.*, vol. 16, no. 5, pp. 738–741, May 2012.

[32] D. Dardari, C. Chong, and M. Win, "Threshold-based time-of-arrival estimators in UWB dense multipath channels," *IEEE Trans. Commun.*, vol. 56, pp. 1366–1378, Aug. 2008.

[33] R. Zhang and X. Dong, "A new time of arrival estimation method using UWB dual pulse signals," *IEEE Trans. Wireless. Commu.*, vol. 7, no. 6, pp. 2057–2062, Jun. 2008.

[34] S. Gezici, Z. Sahinoglu, A. Molisch, H. Kobayashi, and H. Poor, "Two-step time of arrival estimation for pulse-based ultra-wideband systems," *EURASIP J. on Advances in Signal Processing*, vol. 2008, Article ID 529134, 11 pages, May 2008.

[35] J. Youssef, B. Denis, C. Godin, and S. Lesecq, "New TOA estimators within energy-based receivers under realistic UWB channel statistics," in *Proc. IEEE Int. Conf. Vehicular Technology*, May 2010, pp. 1–5.

[36] I. Guvenc and Z. Sahinoglu, "Threshold-based TOA estimation for impulse radio UWB systems," in *Proc. IEEE Int. Conf. Ultra-Wideband*, Sept. 2005, pp. 420–425.

[37] ——, "Threshold selection for UWB TOA estimation based on kurtosis analysis," *IEEE Commun. Lett.*, vol. 9, no. 9, pp. 1025–1027, 2005.

[38] X. Chi and C. L. Law, "Delay-dependent threshold selection for UWB TOA estimation," *IEEE Commun. Lett.*, vol. 12, no. 5, pp. 380–382, May, 2008.

[39] A. Hirata, T. Morimoto, and Z. Kawasaki, "DOA estimation of ultra-wideband EM waves with MUSIC and interferometry," *IEEE Antennas Propag. Lett.*, vol. 2, no. 1, pp. 190–193, 2003.

[40] V. Mani and R. Bose, "Direction of arrival estimation and beamforming of multiple coherent UWB signals," in *Proc. IEEE Int. Conf. Communications*, Cape Town, South Africa, May 2010, 5 pages.

[41] H. Keshavarz, "Weighted signal-subspace direction-finding of ultra-wideband sources," in *Proc. IEEE Int. Conf. Wireless and Mobile Computing, Networking and Communications*, Montreal, Canada, Aug. 2005, pp. 23–29.

[42] A. Marath, A. Leyman, and H. Garg, "New focusing scheme for DOA estimation of multipath clusters in WiMedia UWB systems without coarse estimation of angle of arrival," *IEEE Commun. Lett.*, vol. 14, no. 2, pp. 103–105, 2010.

[43] Y. Zhang, A. Brown, W. Malik, and D. Edwards, "High resolution 3-D angle of arrival determination for indoor UWB multipath propagation," *IEEE Trans. Wireless Commun.*, vol. 7, no. 8, pp. 3047–3055, Aug. 2008.

[44] N. Iwakiri and T. Kobayashi, "Joint TOA and AOA estimation of UWB signal using time domain smoothing," in *Proc. Int. Symp. on Wireless Pervasive Computing*, no. 23, Puerto Rico, Feb. 2007, 6 pages.

[45] E. Lagunas, M. Najar, and M. Navarro, "UWB joint TOA and DOA estimation," in *Proc. IEEE Int. Conf. Ultra-Wideband*, Sept. 2009, pp. 839–843.

[46] Y. Luo and C. Law, "Indoor positioning using UWB-IR signals in the presence of dense multipath with path overlapping," *IEEE Trans. Wireless Commun.*, vol. 11, no. 10, pp. 3734–3743, Aug. 2012.

[47] M. Navarro and M. Najar, "Joint estimation of TOA and DOA in IR-UWB," in *Proc. IEEE Workshop Signal Processing Advances in Wireless Communications*, June 2007, pp. 1–5.

[48] ——, "TOA and DOA estimation for positioning and tracking in IR-UWB," in *Proc. IEEE Int. Conf. Ultra-Wideband*, Sept. 2007, pp. 574–579.

[49] ——, "Frequency domain joint TOA and DOA estimation in IR-UWB," *IEEE Trans. Wireless Commun.*, vol. 10, no. 10, pp. 1–11, Oct. 2011.

[50] L. Taponecco, A. A. D'Amico, and U. Mengali, "Joint TOA and AOA estimation for UWB localization applications," *IEEE Trans. Wireless Commun.*, vol. 10, no. 7, pp. 2207–2217, July 2011.

[51] Z. Sahinoglu and I. Guvenc, "Multiuser interference mitigation in non-coherent UWB ranging via nonlinear filtering," *EURASIP J. on Wireless Communications and Networking*, vol. 2006, pp. 1–10, April 2006.

[52] J. P. Lie and B. P. Ng, "Multiple UWB emitters DOA estimation employing time hopping spread spectrum," *Progress in Electromagnetics Research*, vol. 78, pp. 83–101, 2008.

[53] H. Zhan, J. Ayadi, J. Farserotu, and J.-Y. Le Boudec, "Impulse radio ultra-wideband ranging under multi-user environments," in *Proc. IEEE Int. Conf. Vehicular Technology*, Barcelona, Spain, April 2009, pp. 1–5.

[54] A. Amigo, A. Mallat, and L. Vandendorpe, "Multiuser and multipath interference mitigation in UWB TOA estimation," in *Proc. IEEE Int. Conf. Ultra-Wideband*, Bologna, Italy, Sept. 2011, pp. 465–469.

[55] A. Molisch, "Ultrawideband propagation channels - theory, measurement, and modeling," *IEEE Trans Vechi. Tech.*, vol. 54, no. 5, pp. 1528–1545, May 2005.

[56] T. Phan, V. Krizhanovskii, S. Han, H. Lee, Sand Oh, and N. Kim, "4.7pj/pulse 7th derivative gaussian pulse generator for impulse radio uwb," in *Proc. IEEE Int. Conf. Circuits and Systems*, New Orleans, USA, May 2007, pp. 3043–3046.

[57] S. Sim, D. Kim, and S. Hong, "A CMOS UWB pulse generator for 6-10 ghz applications," *IEEE MicroIwave and Wireless Components Letters*, vol. 19, no. 2, pp. 83–85, 2009.

[58] M. Ghavami, L. Michael, and K. R., *Ultra Wideband Signals and Systems in Communication Engineering*. Wiley Online Library, 2006.

[59] M. Hamalainen, R. Tesi, and J. Iinatti, "On the UWB system performance studies in AWGN channel with interference in UMTS band," in *Proc. IEEE Int. Conf. Ultra-Wideband*, Baltimore, USA, Sept. 2002, pp. 321–325.

[60] Y.-P. Nakache and A. Molisch, "Spectral shape of UWB signals influence of modulation format, multiple access scheme and pulse shape," in *Proc. IEEE Semiannual Conf. Vehicular Technology*, vol. 4, Seoul, Korea, April 2003, pp. 2510–2514.

[61] I. Oppermann, M. Hamalainen, and J. Iinatti, *UWB: Theory and Applications*. Wiley, 2004.

[62] M. Hamalainen, R. Tesi, J. Iinatti, and V. Hovinen, "On the performance comparison of different UWB data modulation schemes in AWGN channel in the presence of jamming," in *Proc. IEEE Int. Conf. Radio and Wireless*, Boston, USA, Aug. 2002, pp. 83–86.

[63] M. D. Benedetto and G. Giancola, *Understanding Ultra Wide Band Radio Fundamentals*. Prentice Hall, 2004.

[64] A. Saleh and R. Valenzuela, "A statistical model for indoor multipath propagation," *IEEE J. Sel. Areas Commun.*, vol. 5, no. 2, pp. 128–137, Feb. 1987.

[65] M. Win, R. Scholtz, and M. Barnes, "Ultra-wide bandwidth signal propagation for indoor wireless communications," in *Proc. IEEE Int. Conf. Commun.*, vol. 1, Montreal, Canada, Jun. 1997, pp. 56–60.

[66] D. Cassioli, M. Win, and A. Molisch, "The ultra-wide bandwidth indoor channel: from statistical model to simulations," *IEEE J. Sel. Areas in Commun.*, vol. 20, no. 6, pp. 1247–1257, Aug. 2002.

[67] L. Hentila, A. Taparungssanagorn, H. Viittala, and M. Hamalainen, "Measurement and modelling of an UWB channel at hospital," in *Proc. IEEE Int. Conf. Ultra-Wideband*, Zurich, Switzerland, Sept. 2005, pp. 113–117.

[68] J. Karedal, S. Wyne, P. Almers, F. Tufvesson, and A. Molisch, "A measurement-based statistical model for industrial ultra-wideband channels," *IEEE Trans. Wireless Commun.*, vol. 6, no. 8, pp. 3028–3037, Aug. 2007.

[69] A. Molisch, "Ultra wideband propagation channels," in *Proc. IEEE*, vol. 97, no. 2, Mar. 2009, pp. 353–371.

[70] J. Foerster, "Channel modelling sub-committee, final report," in *IEEE P802.15-02/490r1-SG3a*, Mar. 2003.

[71] G. Wang, M. Amin, and Y. Zhang, "New approach for target locations in the presence of wall ambiguities," *IEEE Trans. Aerospace and Electronic Systems*, vol. 42, no. 1, pp. 201–315, 2006.

[72] Y. Shen, H. Wymeersch, and M. Win, "Fundamental limits of wideband localization part ii: Cooperative networks," *IEEE Trans. Information Theory*, vol. 56, no. 10, pp. 4981–5000, 2010.

[73] N. Alsindi, B. Alavi, and K. Pahlavan, "Measurement and modeling of ultrawideband TOA-based ranging in indoor multipath environments," *IEEE Trans.Vehicular Technology*, vol. 58, no. 3, pp. 1046–1058, 2009.

[74] S. Duenas, X. Duo, S. Yamac, M. Ismail, and L.-R. Zheng, "CMOS UWB IR non-coherent receiver for RFID applications," in *Proc. IEEE North-East Workshop on Circuits and Systems*, Jun. 2006, pp. 213–216.

[75] D. Dardari and R. D'Errico, "Passive ultrawide bandwidth RFID," in *Proc. IEEE Global Communication Conf.*, New Orleans, USA, Nov. 2008, 6 pages.

[76] S. Hu, Y. Zhou, C. Law, and W. Dou, "Study of a uniplanar monopole antenna for passive chipless UWB-RFID localization system," *IEEE Trans. Antennas Propag.*, vol. 58, no. 2 pp. 271–278, Feb. 2010.

[77] Z. Sahinoglu, S. Gezici, and I. Guvenc, *Ultra-wideband Positioning Systems: Theoretical Limits, Ranging Algorithms, and Protocols*. Cambridge University Press, 2008.

[78] S. Ergut, R. Rao, O. Dural, and Z. Sahinoglu, "Localization via TDOA in a UWB sensor network using neural networks," in *Proc. IEEE Int. Conf. Commun.*, Beijing, China, May 2008, pp. 2398–2403.

[79] J. Caffery, J. and G. Stuber, "Subscriber location in CDMA cellular networks," *IEEE Trans. Vehicular Technology*, vol. 47, pp. 406–416, May 1998.

[80] C. Knapp and G. Carter, "The generalized correlation method for estimation of time delay," *IEEE Trans. Acoust., Speech, Signal Process.*, vol. 24, pp. 320–327, Aug. 1976.

[81] Y. Lee, Y. J. Seo, and G. Choi, "Angle-of-arrival estimation for UWB signals clustered in angle," in *Proc. Int. Symp. on Wireless Pervasive Computing*, Jan. 2006, pp. 1–4.

[82] S. Korkmaz and A.-J. van der Veen, "Matched subspace based correction of large errors in UWB localization," in *Proc. IEEE Symp. Communications and Vehicular Technology*, Nov. 2007, pp. 1–4.

[83] V. La Tosa, B. Denis, and B. Uguen, "Direct path DoA and DoD finding through IR-UWB communications," in *Proc. IEEE Int. Conf. Ultra Wideband*, vol. 2, Hannover, Germany, Sept. 2008, pp. 223–227.

[84] N. Karmakar, *Direction of Arrival (DOA) Estimation of Impulse Radio UWB RFID Tags*. Wiley-IEEE Press, 2010.

[85] D. Chin, Y. Yeh, and C. Hsueh, "Hybrid TDOA/AOA indoor positioning and tracking using extended Kalman filters," in *Proc. IEEE Conf. Vehicular Technology*, vol. 3, May 2006, pp. 1058–1062.

[86] R. Fujiwara, K. Mizugaki, T. Nakagawa, D. Maeda, and M. Miyazaki, "TOA/TDOA hybrid relative positioning system using UWB-IR," in *Proc. IEEE Symp. Radio and Wireless*, San Diego, USA, Jan. 2009, pp. 679–682.

[87] Z. Zou, T. Deng, Q. Zou, M. Sarmiento, F. Jonsson, and L. Zheng, "Energy detection receiver with toa estimation enabling positioning in passive UWB-RFID system," in *Proc. IEEE Int. Conf. Ultra Wideband*, Nanjing, China, Sept. 2010, 4 pages.

[88] W. Shi, R. Annavajjala, P. Orlik, A. Molisch, M. Ochiai, and A. Taira, "Non-coherent TOA estimation for UWB multipath channels using max-eigenvalue detection," in *Proc. IEEE Int. Conf. Commun.*, Ottawa, Canada, June 2012, pp. 4509–4514.

[89] C. Xu and C. Law, "Delay-dependent threshold selection for UWB TOA estimation," *IEEE Commu. lett.*, vol. 12, no. 5, pp. 380–382, 2008.

[90] F. Shang, B. Champagne, and I. Psaromiligkos, "Joint estimation of time of arrival and channel power delay profile on pulse based UWB system," in *Proc. IEEE Int. Conf. Commun.*, Ottawa, Canada, Jun. 2012, pp. 4515–4519.

[91] ——, "Time of arrival and power delay profile estimation for IR-UWB systems," *Signal Processing*, vol. 93, no. 5, pp. 1317–1327, May 2013.

[92] Z. Sahinoglu and S. Gezici, "Ranging in the IEEE 802.15.4a standard," in *Proc. IEEE Annual Conf. Wireless and Microwave Technology*, Dec. 2006, 5 pages.

[93] D. Dardari, G. A., and W. M.Z., "Time-of-arrival estimation of uwb signals in the presence of narrowband and wideband interference," in *Proc. IEEE Int. Conf. Ultra-Wideband*, Singapore, Sept. 2007, pp. 1–6.

[94] Z. Sahinoglu, S. Gezici, and I. Güvenc, *Ultra-wideband Positioning Systems: Theoretical Limits, Ranging Algorithms, and Protocols*. Cambridge University Press, 2008.

[95] R. Zhang and X. Dong, "Synchronization and integration region optimization for uwb signals with non-coherent detection and auto-correlation detection," *IEEE Trans. Commun.*, vol. 56, no. 5, pp. 790–798, May 2008.

[96] F. Vanhaverbeke, Y. Guan, and M. Moeneclaey, "Optimal channel and time-of-arrival estimation for IR-UWB in the presence of pulse overlap," in *Proc. IEEE Int. Conf. Commun.*, May 2010, pp. 1–5.

[97] Z. Xu and B. Sadler, "Time delay estimation bounds in convolutive random channels," *IEEE J. of Selected Topics in Signal Process.*, vol. 1, pp. 418–430, Oct. 2007.

[98] T. Liu, X. Dong, and W. Lu, "Multiresolution wavelet denoising for ultra-wideband time-of-arrival estimation with regularized least squares," *Physical Communication*, vol. 2, no. 4, pp. 285–295, Dec. 2009.

[99] K. Makaratat, T. Brown, and S. Stavrou, "Estimation of time of arrival of UWB multipath clusters through a spatial correlation technique," *IET Microw. Antennas Propag.*, vol. 1, pp. 666–673, Jun. 2007.

[100] D. S. Bernstein, *Matrix Mathematics: Theory, Facts, and Formulas (Second Edition)*. Princeton University Press, 2009.

[101] S. M. Kay, *Modern Spectral Estimation: Theory and Practice*. Prentice-Hall, 1999.

[102] F. Shang, B. Champagne, and I. Psaromiligkos, "A novel ML based joint TOA and AOA estimation for IR-UWB systems," in *Proc. IEEE Int. Conf. Acoustic, Speech and Signal Process.*, Vancouver, Canada, May 2013, 5 pages.

[103] H. S. Lee and C. Sodini, "Analog-to-digital converters: Digitizing the analog world," in *Proc. IEEE*, vol. 96, no. 2, Feb. 2008, pp. 323–334.

[104] G. Durgin and T. Rappaport, "Effects of multipath angular spread on the spatial cross-correlation of received voltage envelopes," in *Proc. IEEE Int. Conf. Vehicular Technology*, vol. 2, Houston, USA, May 1999, pp. 996–1000.

[105] F. C. Schweppe, "Evaluation of likelihood functions for Gaussian signals," *IEEE Trans. Information Theory*, vol. 11, no. 1, pp. 61–70, Jan. 1965.

[106] A. Mallat, J. Louveaux, and L. Vandendorpe, "UWB based positioning in multipath channels: CRBs for AOA and for hybrid TOA-AOA based methods," in *Proc. IEEE Int. Conf. Commun.*, Glasgow, Scotland, June 2007, pp. 5775–5780.

[107] R.-M. Cramer, R. Scholtz, and M. Win, "Evaluation of an ultra-wide-band propagation channel," *IEEE Trans. Antennas Propag.*, vol. 50, no. 5, pp. 561–570, May 2002.

[108] S. Venkatesh, V. Bharadwaj, and R. Buehrer, "A new spatial model for impulse-based ultra-wideband channels," in *Proc. IEEE Int. Conf. Vehicular Technology*, Dallas, USA, Sept. 2005, pp. 2617–2621.

[109] A. Amigo and L. Vandendorpe, "ZIV-ZAKAI lower bound format UWB based toa estimation with multi-user interference," in *Proc. IEEE Int. Conf. Acoustic, Speech and Signal Process.*, Vancouver, Canada, May 2013, 5 pages.

[110] F. Kharrat-Kammoun, C. Le Martret, and P. Ciblat, "Performance analysis of ir-uwb in a multi-user environment," *IEEE Trans. Wireless Commun.*, vol. 8, no. 11, pp. 5552–5563, Nov. 2009.

[111] C. Le Martret, A.-L. Deleuze, and P. Ciblat, "Optimal time-hopping codes for multi-user interference mitigation in ultra-wide bandwidth impulse radio," *IEEE Trans. Wireless Commu.*, vol. 5, no. 6, pp. 1516–1525, Jun. 2006.